NTNU

Norwegian University of
Science and Technology

Wind tunnel testing of bridge decks

Vindtunneltesting av brutverrsnitt

Johannes Raaum Grongstad
Oddbjørn Kildal

Civil and Environmental Engineering
Submission date: June 2018
Supervisor: Ole Andre Øiseth, KT
Co-supervisor: Henrik Skyvulstad, Norconsult

Norwegian University of Science and Technology
Department of Structural Engineering

Institutt for konstruksjonsteknikk

FAKULTET FOR INGENIØRVITENSKAP
NTNU – Norges teknisk-naturvitenskapelige universitet

MASTEROPPGAVE 2018

for

Oddbjørn Kildal og Johannes Grongstad

Vindtunneltesting av brutverrsnitt

Wind tunnel testing of bridge decks

Vindtunneltester brukes rutinemessig i prosjekteringen av brukonstruksjoner som kan settes i bevegelse av vind. Målet med denne oppgaven er at studentene skal lære hvordan seksjonsmodellforsøk av brutverrsnitt utføres og at de skal teste forslag til brokasser som kan benyttes til ei hengebru som krysser Sulafjorden.

Oppgaven bør inneholde følgende temaer:

- Litteraturstudie for vindtunneltesting av brutverrsnitt.
- Utarbeidelse av detaljert oversikt over brukassene til eksisterende hengebruer med langt spenn.
- Prosjektering av en seksjonsmodell studentene har tro på.
- Bygging av seksjonsmodellen og testing i vindtunnelen.

Besvarelsen organiseres i henhold til gjeldende retningslinjer.

Veileder(e): Ole Andre Øiseth, Henrik Skyvulstad

NTNU, 14.01.2018

Ole Andre Øiseth
Faglærer

Summary

First different designs of bridges were investigated to lay out an overview of what bridge designs there were on the table for production and testing. Different bridge cross sections seemed to be favourable for different types of bridges and span lengths. Using the CAD-ing software Fusion 360 and a router a section model of a twin deck bridge girder was built, in a 1:50 scale, based on a suggestion from Multiconsult for the Sulafjorden bridge. The section model was built by carving pieces out from a material called Divinycell and reinforcing the section with an aluminium pipe for strength and stiffness. The model was foiled and held together by end plates using 3D-printed parts for attachment. After assembly the model was explored with regard to eigenfrequencies and results were compared to analytical approximations. The eigenfrequencies of the model proved to be a bit low as it was subject to resonance because of vortex shedding for wind speeds between 0 and 12 m/s. The cross section was tested for static coefficients and aerodynamic derivatives, the precision of the testing and theory was explored through comparing measured forces and theoretical approximated forces.

The gathered data showed that the cross section was resistant to galloping and torsional instability while being vulnerable to static divergence and flutter. It was shown the assumption of the self excited forces being linearly dependent on velocity and displacement is not valid, but yield acceptable results in the vertical and angular directions. The ADs extracted from harmonic motion histories was used to estimate self exited forces from random motion histories with frequency content from 0 to 3.5 Hz. The results showed good correlation between the measured and estimated SE forces in the vertical and angular directions, where the R^2 values were in range 85-95%. There was almost no correlation in the horizontal direction. The findings imply that the linearity of the SE forces and the superposition principle can be used in the vertical and angular direction, but not in the horizontal direction. There was observed some Reynolds dependency and static coefficients decreased as wind speed increased. Methods of reducing vortex shedding vibration were explored and the countermeasure of two spoilers in this case proved to be highly effective while a spoiler and a TMD also alleviated some vibrations.

Sammendrag

Først ble forskjellige typer brutversnitt undersøkt for å kartlegge hva som fantes, hva som ikke var testet og hva som allerede var bygget. Det viste seg at forskjellige typer tverrsnitt var fordelaktig for forskjellige typer broer og forskjellig lengde. Ved hjelp av Fusion 360 og en todimensjonal fres, X-Carve, ble en seksjonsmodell i målestokk 1:50 bygget. Tverrsnittet var et forslag for ei hengebru som skal krysse Sulafjorden, utarbeidet av Multiconsult. Seksjonsmodellen ble bygget opp av deler i et materiale kalt Divinycell. For å oppnå høy nok styrke og stivhet ble modellen forsterket med et aluminiumsrør. Modellen ble videre foliert og holdt sammen av endeplater. Endeplatene var påmontert 3D-printede deler som aluminiumsrørene ble festet i. Da modellen var ferdig bygget ble det gjort noen målinger for å sammenligne analytisk beregnede egenfrekvenser og målte egenfrekvenser. Det viste seg at egenfrekvensene var litt lave, og dermed at tverrsnittet kunne utvise virvelavløsningsvibrasjoner for vindhastigheter mellom 0 og 12 m/s, dette på grunn av resonans. Videre ble det testet i vindtunnel for å finne statiske egenskaper og for å finne de aerodynamiske deriverte. Nøyaktigheten av målingene og teorimetoden ble undersøkt ved å sammenligne målte krefter og krefter estimert fra teori.

Måledata fra seksjonsmodellen viste at tverrsnittet er motstandsdyktig mot gallopering og torsjonsustabiliteter, men sårbart for tilfeller av flutter og statisk divergens. Det er vist at antagelsen om at de selvinduserte kreftene er lineært avhengig av hastighet og forskyvning ikke gjelder, men resultatene viser at det er akseptabelt å anta i vertikal- og rotasjonsretning. De aerodynamiske deriverte som er funnet fra harmoniske bevegelser ble brukt til å estimere selvinduserte krefter fra en tidsserie med tilfeldig bevegelse som inneholder frekvenser fra 0 til 3.5 Hz. Resultatet viste god korrelasjon mellom de målte og estimerte kreftene i vertikal- og rotasjonsretning, der R^2-verdier ble beregnet til 85-95%. Det var nesten ingen korrelasjon i horisontalretning, noe som viser at lineariteten til de selvinduserte kreftene med tanke på hastighet og forskyvning, og superpoisisjonsprinsippet ikke kan benyttes i horisontalretning, men med god tilnærming i de andre retningene. Det ble observert noe Reynoldsavhengighet da de statiske koeffisientene avtok litt i verdi med økende vindhastighet. Metoder for å redusere virvelavløsningsvibrasjoner er diskutert og det viste seg at oppsett med to spoilere reduserte vibrasjoner i alle retninger. Oppsett med TMD reduserte også mye av vibrasjonene.

Preface

Rome was not built in a day, neither was this thesis. We chose to do this project as it was conceptually very interesting, highly relevant for clear purposes and offered a range of widely different tasks through the semester. The project was attractive as it combined theory, practical work, lab work and engineering software all in one thesis. We wish to express our deep gratitude for having had the opportunity to write this thesis.

The work was carried out at the Norwegian University of Science and Technology(NTNU), Department of Structural Engineering(KT). Roughly the thesis first present the necessary theory laying the foundation for further work, then emphasis is on the practical building of the section model, followed by testing in the wind tunnel and finally processing of the acquired results. Efforts have been made to offer physical interpretations of phenomenons that are often only communicated as equations. The building procedure for the section model has been thoroughly documented to assist future building of wind tunnel models. In all of this we have also had a great time.

In the making of this thesis we have for sure been standing on the shoulders of giants. Although as the pile of giants has come of considerable size over the centuries it is not all that clear whoms and how many shoulders one is actually standing on. Taking into consideration the pile of giants has become very high it is not surprising it is rather cloudy a bit down the road. The ever increasing height of the giant pile taken into account it is for sure in its place with some wind engineering. However, being impossible to acknowledge all of those whom acknowledgement deserve, one may focus on the obvious ones.

First and foremost we would like to thank our supervisor Professor Ole Andre Øiseth and our co-supervisor PhD Candidate Henrik Skyvulstad for offering their expertise, always being positive, being available and keeping a great mood. Second we extend our great gratitude to PhD Bartosz Siedziako, Sigurd Berg Aas and Svend Erik Horg for having been pioneers in developing the wind tunnel setup at NTNU. Great thanks goes to lab staff Terje Petersen, Steinar Seehuus, Trond Auestad and Bjørn Scjølberg for always helping with all sorts of requests and showing interest in our project. The book Theory of Bridge Aerodynamics has been a vital source of information and therefore thanks goes to Professor Einar Strømmen. Last and perhaps least but still significant: Our families. Thank you for providing Lego at a young age, facilitating the development of curiosity and basic understanding. Thank you for introducing little children to TV-shows like Newton, lighting the fire and the will to explore. Thank you for always providing an arena for healthy discussion.

Table of Contents

List of Tables

List of Figures

Abbreviations

AD	=	Aerodynamic Derivative
CAD	=	Computer Aided Design
DOF	=	Degree of Freedom
FRF	=	Frequency Response Function
IIR	=	Infinite Impulse Response
MDOF	=	Multiple Degree of Freedom
NPRA	=	Norwegian Public Roads Administration
NW	=	Northwest
PLA	=	Polylactic Acid
PSD	=	Power Spectral Density
Re	=	Reynolds
Sc	=	Scruton
SE	=	Self Excited
St	=	Strouhal
STL	=	Stereolithography
TMD	=	Tuned Mass Damper
UGS	=	Universal Gcode Sender

Chapter 1

Introduction

Norway is a country with incredibly challenging geography when it comes to infrastructure. The country has a unique situation with large parts of its populated areas in between mountains and fjords. To be able to have a functioning infrastructure there are large amounts of ferries constantly running over the fjords allowing traffic to cross. In later years there has been announced ambitious ideas about making the Norwegian coast ferry free, to achieve this one may build submerged tunnels, floating bridges or very long span suspension bridges. Some of the bridges that may be built will not only be record breaking by far, but also much more slender structures than anything ever seen as traffic in Norway is not as intense as in larger countries like the USA or China, and therefore does not require as large cross sections as currently seen in the worlds longest spans.

The wind induced dynamic response is a crucial aspect in design of long span bridges. Wind induced forces may displace a structure in such a way that the wind induced forces change due to changes in position or velocity. So there are forces which may cause changes whom in turn change the forces themselves, these forces are called self excited forces. Self excited forces may cause multiple instability phenomenons which are undesirable as they may cause trouble with regard to serviceability and even cause failure in the ultimate limit state. In industry efforts to predict self excited forces for long span bridges usually involve conducting wind tunnel tests to extract aerodynamic derivatives. The aerodynamic derivatives are meant to specifically describe how wind induced forces change with regard to the displacement and velocity of a bridge section.

In later years it has been shown the way bridges have usually been built can not be applied if even longer spans are to be realised. To overcome the challenges of dynamic forces and instabilities it has been developed numerous bridge designs with their strengths and weaknesses. This thesis seeks to enlighten the field of aerodynamic design of long span bridges and determine the aerodynamic properties of a proposed cross section for the Sulafjorden Bridge which is planned to have a main span of 2800 meters.

Chapter 2

Theory

In this chapter fundamental theory is presented to lay the foundation for further work. Mainly theory is collected from books and scientific articles.

2.1 Cross Sections

The cross section of a bridge determines a lot of the bridges behaviour due to wind, therefore cross sections for long span bridges are subject to a lot of research. The aerodynamic properties of cross sections has been an increasingly important topic since the Tacoma Narrows Bridge disaster in 1940(Kardon, 2010) and wind tunnel trials are an important tool for estimating aerodynamic properties of a cross section.

2.1.1 Existing Bridge Designs

Mainly there are five different deck types of interest for long span bridges. There are single-, twin- and triple streamlined decks, trusses and prefabricated concrete and steel composite decks.

Figure 2.1: Comparison of Akashi (left) and Messina (right) horizontal deflection due to wind in the wind tunnel. Equivalent wind speed = 60 m/s. The Akashi photo is courtesy of Honshu-Shikoku Bridge Expressway Company Limited Japan. (Diana et al., 2015)

As seen from figure 2.1 different cross sections may give rise to very different responses from the same conditions depending on the type and shape. To serve as benchmarks showing what is currently proven to be possible cross sections of particular interest is presented below.

Akashi Kaikyo Bridge

Cross section type: Truss
Design: Suspension
Main span length: 1991 m
Country: Japan

The Akashi Kaikyo bridge has the longest span in the world. As figure 2.2 shows the bridge deck is a truss construction made from steel. The truss structure has a clear downside giving large drag forces compared to more streamlined decks. Large drag forces on the girder exert large flexural moment on the towers and becomes a limitation for very long span bridges(Diana et al., 2015).

Figure 2.2: Akashi Kaikyo cross section. (Brancaleoni, 2016)

Great Belt Bridge

Cross section type: Single deck
Design: Suspension
Main span length: 1624 m
Country: Denmark

The Great Belt bridge has the fourth longest bridge span in the world and as figure 2.3 shows a single box deck girder. Due to aerodynamic stability issues single box decks are only feasible for spans up to 1500 - 1600 m(Brancaleoni, 2016) so the Great Belt bridge is pushing the limit for a single deck.

Figure 2.3: Great Belt cross section. (Brancaleoni, 2016)

Xihoumen Bridge

Cross section type: Twin deck
Design: Suspension
Main span length: 1650 m
Country: China

The Xihoumen bridge has the third longest bridge span in the world. As figure 2.4 shows the bridge has a twin deck girder with somewhat rough edges possibly increasing static drag, but decreasing Reynolds dependency due to clear separation points for the air flow. Multiple deck girders are a valid alternative for spans more than 1400 m(Brancaleoni, 2016).

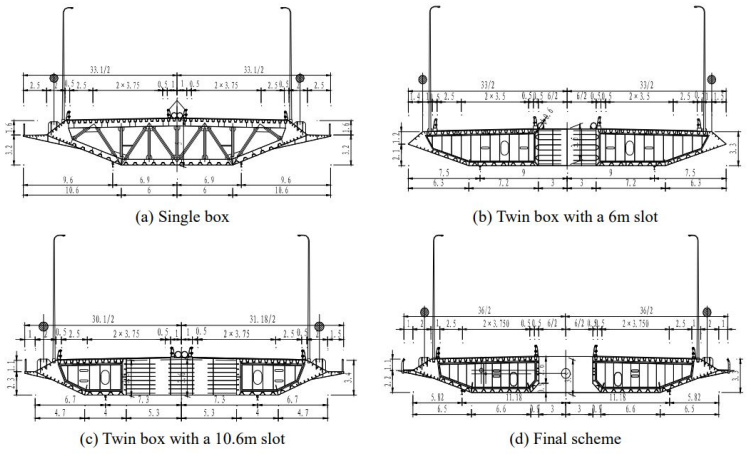

Figure 2.4: Xihoumen cross section. (Ge and Xiang, 2008)

Tsing Lung Bridge

Cross section type: Twin deck
Design: Suspension
Main span length: 1418 m
Country: Hong Kong

The Tsing Lung bridge has a twin deck girder and as seen in figure 2.5 it is clearly more streamlined than the Xihoumen bridge in order to have a low drag coefficient, but the streamlining makes the position of separation points up for questioning and possibly makes the wind induced forces on the section depend on turbulence.

Figure 2.5: Tsing Lung cross section. (Brancaleoni, 2016)

Yangluo Yangtze River Bridge

Cross section type: Prefabricated concrete and steel composite
Design: Suspension
Main span length: 1280 m
Country: China

The Yangluo Yangtze bridge has a girder made from prefabricated concrete and steel composite. This is not a common way of constructing long span suspension bridges as it similarly to the Akashi bridge may lead to large drag forces due to the lack of streamlining. An overview of the Yangluo Yangtze bridge is shown in figure 2.6.

Figure 2.6: Yangluo Bridge. (Constellationevolution, 2010)

Stonecutters Bridge

Cross section type: Twin deck
Design: Cable stayed
Main span length: 1018 m
Country: Hong Kong

The Stonecutters bridge is a cable stayed bridge with a twin deck girder as shown in figure 2.7. Cable stayed bridges are however not believed to be the future for very long span bridges due to large compression forces in the girder during erection. This increasing sensitivity to static and dynamic wind effects, the progressively larger structures needed for anchoring the side span stays, the height necessary for the towers and the complex challenge of controlling the various possible forms of dynamic wind response of long stays(Brancaleoni, 2016).

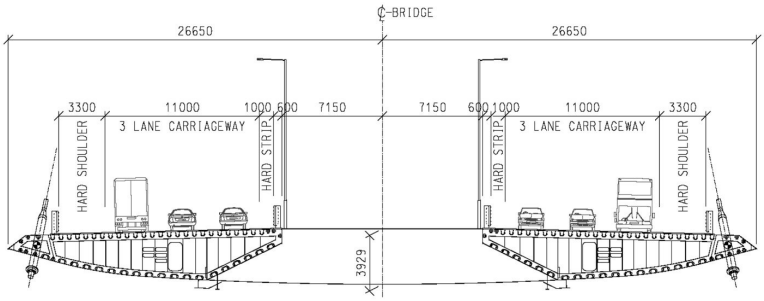

Figure 2.7: Stonecutters cross section. (Hui and Wong, 2009)

Messina Bridge Feasibility Study

Cross section type: Triple deck
Design: Suspension
Main span length: 3300
Country: Italy

The Messina bridge would have had a triple deck girder as shown in figure 2.8 and would have been the worlds longest bridge span by far with a main span of 3300 m. Having been a symbolic project in Italy the bridge has been subject to large amounts of research, though being extremely technically and economically challenging the bridge has not yet been built(Ramsden, 2009). As shown in figure 2.1 the deflections of the Akashi and Messina bridge aeroelastic models during wind tunnel tests at an equivalent full scale wind speed of 60 m/s shows the importance of aerodynamic design. The maximum deflection for Messina at mid span is around 10 m, compared with approximately 30 m for Akashi even if the Messina bridge span is much longer(Diana et al., 2015).

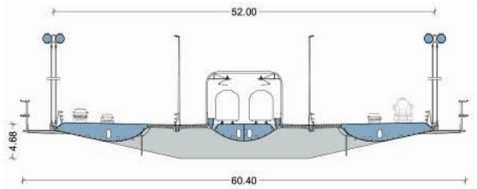

Figure 2.8: Messina cross section. (Brancaleoni, 2016)

List of longest bridge spans in the world

Table 2.1 shows a list of the longest bridge spans in the world. Among the longest bridge spans there are suspension bridges and cable stayed bridges as well as trusses, single decks, twin decks and composite decks. The list provides an overview of what is proven to be possible, what is considered to be relatively unsensational and what is considered to be challenging projects.

No.	Name	Cross section	Design	Main span [m]	Country
1	Akashi Kaikyo	Truss	Suspension	1991	Japan
2	Yangsigang	Twin deck	Suspension	1700	China
3	Xihoumen	Twin deck	Suspension	1650	China
4	Great Belt	Single deck	Suspension	1624	Denmark
5	Izmit	Single deck	Suspension	1550	Turkey
6	Yi-Sunsin	Twin deck	Suspension	1545	South-Korea
7	Runyang	Single deck	Suspension	1490	China
8	Tsing Lung	Twin deck	Suspension	1418	China
9	Humber	Single deck	Suspension	1410	UK
10	Yavuz Sultan Selim	Single deck	Suspension	1408	Turkey
11	Jiangyin	Single deck	Suspension	1385	China
12	Tsing Ma	Twin deck	Suspension	1377	China
13	Hardanger	Single deck	Suspension	1310	Norway
14	Verrazano-Narrows	Truss	Suspension	1298	USA
15	Golden Gate	Truss	Suspension	1280	USA
16	Yangluo	Composite	Suspension	1280	China
17	Hga Kusten	Single deck	Suspension	1210	Sweden
18	Longjiang	Single deck	Suspension	1196	China
19	Jinshajiang Taku	Single deck	Suspension	1190	China
20	Aizhai	Truss	Suspension	1176	China
21	Mackinac	Truss	Suspension	1158	USA
22	Ulsan	Single deck	Suspension	1150	South-Korea
23	Hålogaland	Single deck	Suspension	1145	Norway
24	Qingshuihe	Truss	Suspension	1130	China
25	Huangpu	Single deck	Suspension	1108	China
26	Russky	Single deck	Cable stayed	1104	Russia
27	Minami Bisan-Seto	Truss	Suspension	1100	Japan
28	Daduhe Luding	Truss	Suspension	1100	China
29	Hutong	Truss	Cable stayed	1092	China
30	Fatih Sultan Mehmet	Single deck	Suspension	1090	Turkey

Table 2.1: Table of longest bridge spans. (Wikipedia, 2018) (Virola, 2018)

2.1.2 Width-to-Depth Ratio

M. Matsumoto et al.(Matsumoto, 1996) tested rectangular cylinders with width-to-height (B/D) ratio in the range of 5 to 20, and they found that the B/D ratio had a significant impact on the aerodynamic stabilization. Further studies done by Lin, Cheng, Wu et al.(Lin et al., 2005) extend the result above. They investigated the effect of the deck geometry together with the effect of turbulence in the oncoming wind. Both a closed box and a plate girder with different width-to-depth ratios were tested and the effect on the drag, lift and torsional coefficients were investigated along with the effect on the Aerodynamic Derivatives (ADs). They found that selecting a flatter deck shape can improve the aerodynamic

stability, and that this effect is more significant in more bluff bodied cross sections than in streamlined cross sections. However, the critical wind speed for the major instability phenomena is much higher for a streamlined box cross section, and it is therefore more aerodynamically stable. For a closed box girder the depth-to-width ratio does not affect the lift-, drag-, and torsional coefficients significantly, while the effect is larger on a plate girder, also supporting the choice of a closed box girder in wider long span bridges(Horg and Aas, 2016). Reduction in aspect ratio has effects on drag coefficient and on base pressure coefficient which are similar to those associated with increase in blockage ratio(West and Apelt, 1982). The strength of the vortex excitation is sensitive to the ratio of girder depth to deck width(Irwin, 2008).

2.1.3 Bluffness of a Cross Section

Bluff bodies are bodies that are not streamlined. Wind is one of the principal forces of nature and, since most structures are bluff bodies, bluff body aerodynamics therefore becomes a critical topic affecting structural design(Irwin, 2008). For a bluff body the separation points of the flow usually gives rise to a wake of significant width, causing pressure differences to matter more to the drag forces than viscous shear. When the drag is dominated by viscous drag, we say the body is streamlined, and when it is dominated by pressure drag, we say the body is bluff. Whether the flow is viscous-drag dominated or pressure-drag dominated depends entirely on the shape of the body. A streamlined body looks like a fish, or an airfoil at small angles of attack, whereas a bluff body looks like a brick, a cylinder, or an airfoil at large angles of attack. For a given frontal area and velocity, a streamlined body will always have a lower resistance than a bluff body. For example, as figure 2.9 shows, the drag of a cylinder of diameter D can be ten times larger than a streamlined shape with the same thickness(Princeton, 2018).

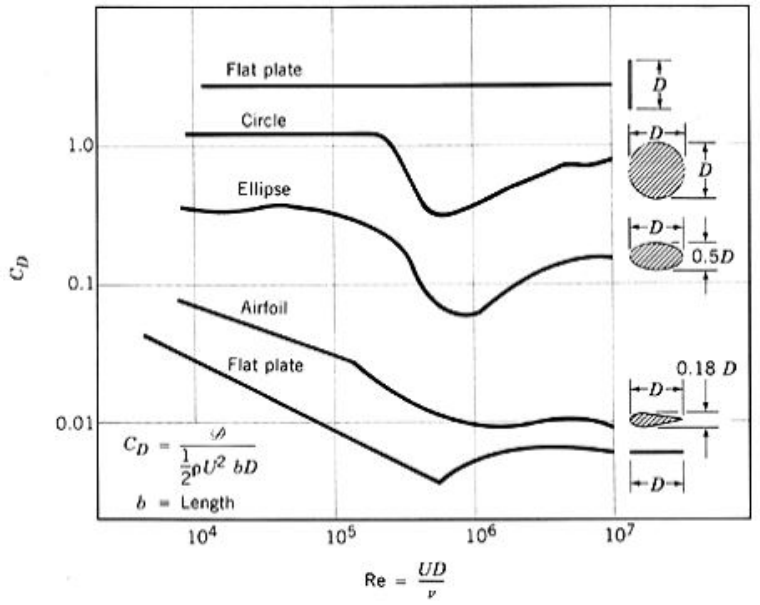

Figure 2.9: Drag coefficients of bodies as function of Reynolds number. (Princeton, 2018)

2.1.4 Twin Deck Sections

A twin deck section is a section where the traffic is carried by two separated girders. Twin deck sections are now used in many of the worlds longest bridges as single deck sections seems inadequate for very long span bridges due to stability problems. It is shown that the favorable aerodynamic effects of the center slot on bridge decks depend on the aerodynamic shape of the box girders and on the slot widths rather than unconditionally improving the aeroelastic stability(Yang et al., 2014). Hypotheses have been made and research executed showing twin deck sections may be more sensitive to vortex shedding than single deck sections. Vortices shed from the upwind girder may hit the downwind girder causing larger pressure fluctuations on the downwind girder causing the twin deck section to be more susceptible to vortex shedding excitation than a single deck girder(Larsen et al., 2008). Research shows that the slot width has the potential to significantly affect the pressure distribution and hence the corresponding aerodynamic performance of a bridge deck(Kwok et al., 2012).

2.2 Basic Dynamics

The dynamic theory start with the equation of motion, this is an equilibrium equation:

$$M\ddot{r}(t) + C\dot{r}(t) + Kr(t) = q(t) \tag{2.1}$$

where M is the mas of the system, C the damping and K the stiffness, q is the force applied on the system, r is the response as a function of time, one dot represents the first

time derivative and two dots represent the second time derivative. The equation can be rewritten to

$$\ddot{r}(t) + 2\zeta\omega_n\dot{r}(t) + \omega_n^2 r(t) = \frac{q(t)}{M} \tag{2.2}$$

and the following is obtained

$$\text{Eigenfrequency:} \quad \omega_n = \sqrt{\frac{K}{M}}, \quad \text{Damping ratio:} \quad \zeta = \frac{C}{C_{cr}} = \frac{C}{2M\omega_n} \tag{2.3}$$

It can be shown that the frequency response function (FRF) becomes:

$$H(w) = \frac{1}{1 - (\frac{\omega}{\omega_n})^2 + 2i\frac{\omega}{\omega_n}\zeta} \tag{2.4}$$

when $\omega = \omega_n$ the only term limiting the FRF not to go to infinity is the damping term. This phenomena is called resonance.

Multi degree of freedom system (MDOF)

$$(K - \omega_n^2 M)\phi = 0 \quad \Longrightarrow \quad det(K - \omega_n^2 M) = 0 \tag{2.5}$$

Where ϕ is the modeshape of the corresponding eigenfrequency, and the response becomes:

$$r(x,t) = \phi(x)\eta(t) \tag{2.6}$$

where $\phi(x)$ is the modeshape of the corresponding eigenvalue ω_n.

What happens at resonance is that the dynamic forces applied to the system are in sync with the motion and has the same frequency as a natural frequency of the system. When the dynamic forces are in sync they may at all times work in the direction of the velocity of the system which results in the dynamic forces solely adding energy as opposed to when they are not in sync and up to half of the time extract energy from the system. This is something that may be seen from an Argand diagram when the velocity vector and the force vector have the same orientation which happens when the phase angle is ninety degrees.

2.3 Aerodynamic Forces

When a structure is exposed to a flow of a substance, forces are applied to the structure. These forces are a result of both friction and change in flow pattern around the affected body. It is convenient to calculate stagnation pressure with Bernoulli's equation.

$$q_u(t) = \frac{1}{2}\rho V^2(t) \tag{2.7}$$

where q_u is the pressure on the body, ρ is the density of the substance and $V(t)$ is the flow velocity of the substance.

The stagnation pressure can be derived from Bernoulli's equation shown below in pressure form(Elger and Roberson, 2016):

$$p + \gamma z + \rho \frac{V^2}{2} = Constant \tag{2.8}$$

which when

$$z_1 = z_2 = Constant \quad and \quad V_2 = 0 \tag{2.9}$$

leads to

$$Q = p_2 - p_1 = \frac{1}{2}\rho V_1^2 \tag{2.10}$$

Three moment and three force components have to be considered. But in cases of bridge engineering, the structure is often extended only in one direction, and the concerning force is the wind perpendicular to this direction, as seen in figure 2.10. So a good approximation is to look at a 2D slice of unit thickness cut off by two planes perpendicular to the longitudinal axis. The idea is the same as the plane strain analysis in the theory of elasticity. In this case only the drag, lift and pitching moment need to be considered.

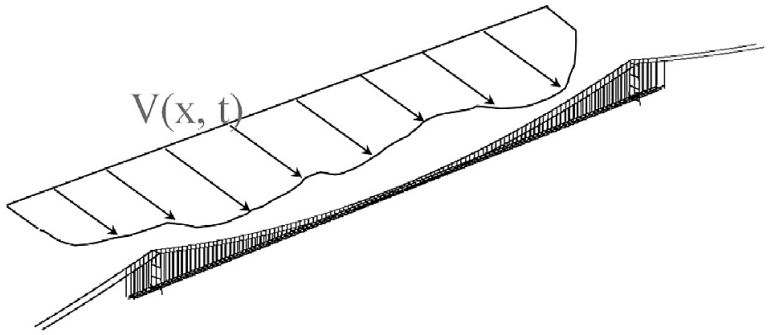

Figure 2.10: Wind turbulence: In an inhomogeneous wind field wind speed varies with space and time. (Diana et al., 2015)

When applying quasi-steady aerodynamics the history of motion can be ignored. Resulting in the aerodynamic forces at any time depending only on the instantaneous position and velocity of the body at that particular moment. So when the quasi-steady approximation is applied, three aerodynamic force components are simply given by

$$q_D = QDC_D(\alpha), \quad q_L = QBC_L(\alpha) \quad and \quad q_M = QB^2C_M(\alpha) \tag{2.11}$$

where q_D, q_L and q_M are line loads, B and D is respectively the width and height of the cross-section, and

$$Q = \frac{1}{2}\rho V_{rel}^2 = \frac{1}{2}\rho(V + u - \dot{r})^2 \tag{2.12}$$

where Q is the stagnation pressure of the flow(Tamura and Kareem, 2013) and $V_{rel} = V + u - \dot{r}$ is the wind speed relative to the bridge in the horizontal direction. This leads to the static wind loads

$$F_D = \frac{1}{2}\rho(DL)V^2 C_D(\alpha), \quad F_L = \frac{1}{2}\rho(BL)V^2 C_L(\alpha) \quad and \quad M = \frac{1}{2}\rho B(BL)V^2 C_M(\alpha) \tag{2.13}$$

The static wind components $C_D(\alpha)$, $C_L(\alpha)$ and $C_M(\alpha)$ is further used in the buffeting theory.

2.4 The Buffeting Theory

The buffeting theory is based on the assumption that wind consist of two parts, the stationary wind speed (V), which only depends on the position, and the fluctuating part(u, v and w), which also depends on the time, t. Figure 2.11 shows a visualisation of the different parameters. Mathematically this is expressed as

$$U(x, y, z, t) = V(x, y, z) + u(x, y, z, t) + v(x, y, z, t) + w(x, y, z, t) \tag{2.14}$$

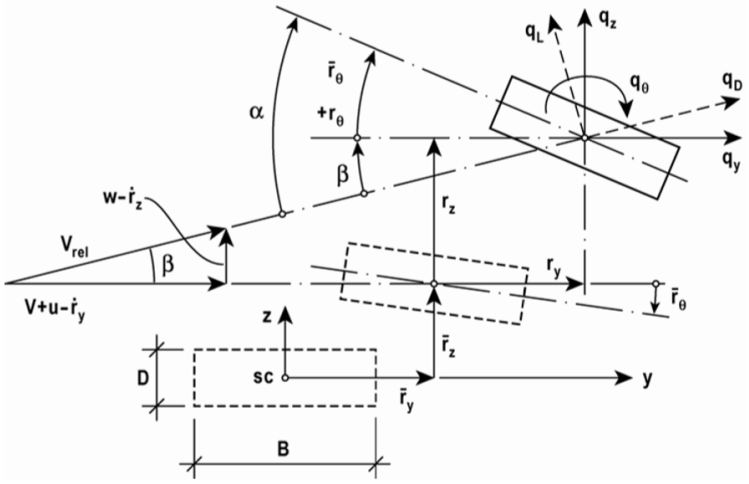

Figure 2.11: Displacements and rotations as response of a wind flow. (Strømmen, 2010)

The acting drag, lift and moment forces is found using the Bernoulli's equation:

$$\begin{bmatrix} q_D \\ q_L \\ q_M \end{bmatrix} = \frac{1}{2}\rho V_{rel}^2 \begin{bmatrix} DC_D(\alpha) \\ BC_L(\alpha) \\ B^2 C_M(\alpha) \end{bmatrix} \tag{2.15}$$

where α is the corresponding angle of flow incidence as shown in figure 2.11. This can be transformed to the structural axis by a transformation matrix

$$\mathbf{q}_{tot}(x,t) = \begin{bmatrix} q_y \\ q_z \\ q_\theta \end{bmatrix}_{tot} = \begin{bmatrix} \cos\beta & -\sin\beta & 0 \\ \sin\beta & \cos\beta & 0 \\ 0 & 0 & 1 \end{bmatrix} \begin{bmatrix} q_D \\ q_L \\ q_M \end{bmatrix} \tag{2.16}$$

where

$$\beta = arctan\left(\frac{w - \dot{r_z}}{V + u - \dot{r_y}}\right) \tag{2.17}$$

When applying an approximation where the assumption is that the mean wind is much greater than the fluctuating part ($V >> u, v, w$).

$$\left.\begin{array}{c} U_{rel}^2 = (V + u - \dot{r_y})^2 + (w + \dot{r_z})^2 \approx V^2 + 2Vu - 2V\dot{r_y} \\ \alpha = \overline{r_\theta} + r_\theta + \beta \approx \overline{r_\theta} + r_\theta + \frac{w}{V} - \frac{\dot{r_z}}{V} \end{array}\right\} \tag{2.18}$$

$$\begin{bmatrix} C_D(\alpha) \\ C_L(\alpha) \\ C_M(\alpha) \end{bmatrix} = \begin{bmatrix} C_D(\overline{\alpha}) \\ C_L(\overline{\alpha}) \\ C_M(\overline{\alpha}) \end{bmatrix} + \alpha_f \begin{bmatrix} C'_D(\overline{\alpha}) \\ C'_L(\overline{\alpha}) \\ C'_M(\overline{\alpha}) \end{bmatrix} \tag{2.19}$$

where α_f is the fluctuating part of angle α. For simplicity this notation is used:

$$\begin{bmatrix} C_D(\overline{\alpha}) \\ C_L(\overline{\alpha}) \\ C_M(\overline{\alpha}) \end{bmatrix} = \begin{bmatrix} \overline{C}_D \\ \overline{C}_L \\ \overline{C}_M \end{bmatrix} \quad \text{and} \quad \begin{bmatrix} C'_D(\overline{\alpha}) \\ C'_L(\overline{\alpha}) \\ C'_M(\overline{\alpha}) \end{bmatrix} = \begin{bmatrix} C'_D \\ C'_L \\ C'_M \end{bmatrix} \tag{2.20}$$

Combining Eqs. 2.15 - 2.20:

$$\begin{bmatrix} q_y \\ q_z \\ q_\theta \end{bmatrix}_{tot} = \rho V \left(\frac{V}{2} + u - \dot{r_y}\right) \left\{ \begin{bmatrix} D\overline{C}_D \\ B\overline{C}_L \\ B^2\overline{C}_M \end{bmatrix} + \left(r_\theta + \frac{w}{V} - \frac{\dot{r_z}}{V}\right) \begin{bmatrix} DC'_D \\ BC'_L \\ B^2 C'_M \end{bmatrix} + \frac{w - \dot{r_z}}{V} \begin{bmatrix} -B\overline{C}_L \\ D\overline{C}_D \\ 0 \end{bmatrix} \right\} \tag{2.21}$$

By discarding higher order terms, the following is obtained:

$$\mathbf{q}_{tot}(x,t) = \begin{bmatrix} \overline{q}_y(x) \\ \overline{q}_z(x) \\ \overline{q}_\theta(x) \end{bmatrix} + \begin{bmatrix} q_y(x,t) \\ q_z(x,t) \\ q_\theta(x,t) \end{bmatrix} = \overline{\mathbf{q}} + \overline{\mathbf{B}}_q \mathbf{v} + \mathbf{C}_{ae}\dot{\mathbf{r}} + \mathbf{K}_{ae}\mathbf{r} \tag{2.22}$$

where

$$\mathbf{v}(x,t) = \begin{bmatrix} u & w \end{bmatrix}^T \tag{2.23}$$

$$\mathbf{r}(x,t) = \begin{bmatrix} r_y & r_z & r_\theta \end{bmatrix}^T \tag{2.24}$$

$$\overline{\mathbf{q}}(x) = \begin{bmatrix} \overline{q}_y \\ \overline{q}_z \\ \overline{q}_\theta \end{bmatrix} = \frac{\rho V^2 B}{2} \begin{bmatrix} (\frac{D}{B})\overline{C}_D \\ \overline{C}_L \\ B\overline{C}_M \end{bmatrix} = \frac{\rho V^2 B}{2} \hat{\mathbf{b}}_q \tag{2.25}$$

$$\mathbf{B}_q(x) = \frac{\rho V B}{2} \begin{bmatrix} 2(\frac{D}{B})\overline{C}_D & ((\frac{D}{B})C'_D - \overline{C}_L) \\ 2\overline{C}_L & (C'_L + (\frac{D}{B})\overline{C}_D) \\ 2B\overline{C}_M & BC'_M \end{bmatrix} = \frac{\rho V B}{2} \hat{\mathbf{B}}_q \tag{2.26}$$

$$\mathbf{C}_{ae}(x) = -\frac{\rho V B}{2} \begin{bmatrix} 2(\frac{D}{B})\overline{C}_D & ((\frac{D}{B})C'_D - \overline{C}_L) & 0 \\ 2\overline{C}_L & (C'_L + (\frac{D}{B})\overline{C}_D) & 0 \\ 2B\overline{C}_M & BC'_M & 0 \end{bmatrix} \tag{2.27}$$

$$\mathbf{K}_{ae}(x) = -\frac{\rho V^2 B}{2} \begin{bmatrix} 0 & 0 & (\frac{D}{B})C'_D \\ 0 & 0 & C'_L \\ 0 & 0 & BC'_M \end{bmatrix} \tag{2.28}$$

So its seen that the total load vectors comprises a time invariant mean (static) part

$$\overline{\mathbf{q}}(x) = \begin{bmatrix} \overline{q}_y \\ \overline{q}_z \\ \overline{q}_\theta \end{bmatrix} = \frac{\rho V^2 B}{2} \hat{\mathbf{b}}_q \tag{2.29}$$

and a fluctuating (dynamic) part

$$\mathbf{q}(x,t) = \begin{bmatrix} q_y \\ q_z \\ q_\theta \end{bmatrix} = \mathbf{B}_q \mathbf{v} + \mathbf{q}_{ae} = \mathbf{B}_q \mathbf{v} + \mathbf{C}_{ae} \dot{\mathbf{r}} + \mathbf{K}_{ae} \mathbf{r} \tag{2.30}$$

(Strømmen, 2010)

2.5 Self Excited Forces

The total wind load on a structure consists of many different contributions. Self excited forces is one of them, and they are the contribution where the motion of the structure itself causes a change in forces. Aerodynamic derivatives(ADs) extend the buffeting theory by including frequency in the load description. Aerodynamic derivatives describe the self excited forces and are functions of wind velocity and motion frequency of the structure. Cross section shape determine the ADs. Self excited forces are the cause of different instability phenomenons, therefore it is important to know their behaviour in order to improve bridge design.

The aerodynamic derivatives were proposed by Scanlan and Tomko(1971) to characterise the self excited forces acting on a bridge, depending on the configuration of the bridge cross section, which were usually identified from wind tunnel experiments(Scanlan and Tomko, 1971).

$$\begin{bmatrix} D_{SE} \\ L_{SE} \\ M_{SE} \end{bmatrix} = \begin{bmatrix} P_1 & P_5 & P_2 \\ H_5 & H_1 & H_2 \\ A_5 & A_1 & A_2 \end{bmatrix} \begin{bmatrix} \dot{r}_y \\ \dot{r}_z \\ \dot{r}_\theta \end{bmatrix} + \begin{bmatrix} P_4 & P_6 & P_3 \\ H_6 & H_4 & H_3 \\ A_6 & A_4 & A_3 \end{bmatrix} \begin{bmatrix} r_y \\ r_z \\ r_\theta \end{bmatrix} \tag{2.31}$$

In equation 2.31 the ADs are divided in two different groups. The first is the aerodynamic damping related group, and the latter is the aerodynamic stiffness related group. All the ADs contribute to the self excited forces D_{SE}, L_{SE} and M_{SE}.

$$\mathbf{C}_{ae} = \begin{bmatrix} P_1 & P_5 & P_2 \\ H_5 & H_1 & H_2 \\ A_5 & A_1 & A_2 \end{bmatrix} \tag{2.32}$$

Where:
- P_1, P_5 and P_2 is the change in drag due to horizontal, vertical and angular velocity.
- H_5, H_1 and H_2 is the change in lift due to horizontal, vertical and angular velocity.
- A_5, A_1 and A_2 is the change in moment due to horizontal, vertical and angular velocity.

$$\mathbf{K}_{ae} = \begin{bmatrix} P_4 & P_6 & P_3 \\ H_6 & H_4 & H_3 \\ A_6 & A_4 & A_3 \end{bmatrix} \tag{2.33}$$

Where:
- P_4, P_6 and P_3 is the change in drag due to horizontal, vertical and angular displacement.
- H_6, H_4 and H_3 is the change in lift due to horizontal, vertical and angular displacement.
- A_6, A_4 and A_3 is the change in moment due to horizontal, vertical and angular displacement.

In order to obtain true ADs for the cross section shape the

$$\mathbf{C}_{ae}$$

and

$$\mathbf{K}_{ae}$$

must be made dimensionless. The relation giving the dimensionless quantities is taken as:

$$\mathbf{C}_{ae} = \frac{\rho B V}{2} K_r \hat{\mathbf{C}}_{ae} \quad and \quad \mathbf{K}_{ae} = \frac{\rho V^2}{2} K_r^2 \hat{\mathbf{K}}_{ae} \tag{2.34}$$

where $K_r = \frac{\omega B}{V}$ is the reduced frequency used to find the ADs, and where

$$\hat{\mathbf{C}}_{ae} = \begin{bmatrix} P_1^* & P_5^* & BP_2^* \\ H_5^* & H_1^* & BH_2^* \\ BA_5^* & BA_1^* & B^2A_2^* \end{bmatrix} \tag{2.35}$$

and

$$\hat{\mathbf{K}}_{ae} = \begin{bmatrix} P_4^* & P_6^* & BP_3^* \\ H_6^* & H_4^* & BH_3^* \\ BA_6^* & BA_4^* & B^2A_3^* \end{bmatrix} \tag{2.36}$$

$\mathbf{C}_{ae}$ and $\mathbf{K}_{ae}$ are called the equivalent aerodynamic derivatives. $\hat{\mathbf{C}}_{ae}$ and $\hat{\mathbf{K}}_{ae}$ are called the true aerodynamic derivatives. The relation can be seen in equation 2.34.

Despite the assumption of self excited forces depending linearly on velocities and displacements the ADs may be highly nonlinear as functions of the reduced velocity and may for example be divided into two groups: The group with torsional amplitudes less or equal to ten degrees, and the group with amplitudes larger than ten degrees. Flow patterns around a section of the two groups may differ substantially; one group may remain an overall streamlined pattern with locally distributed vortices and detached flow, while the other may show fully detached flow with large vortices emerging and developing drastically(Zhang et al., 2017). This makes the aerodynamic derivative P_3^* particularly susceptible to non-linearity.

2.6 Vortex Shedding

Vortex shedding occur when a structure separates the flow of a fluid, such as air. This separation generates vortices behind the structure to be shed alternately on either side of the structure. This generates fluctuating across wind forces q_z, and cross-sectional torsion moment q_θ, accompanied by fluctuating displacements r_z, r_θ which are harmful in case of resonance.

Shedding frequency is taken as $f_s = St\frac{V}{D}$, where St is the Strouhal number. Theoretically resonance will occur when f_s is equal to any eigenfrequency f_i, $f_i = f_s$(Strømmen, 2010).

Vortex shedding is a complex phenomenon and may involve three dimensional flow patterns(Buresti, 1998). For this thesis it is pointed out vortex shedding is a potential problem, deeper investigation is outside the scope of this thesis.

2.7 Motion Induced Instabilities

An increase in the mean wind velocity will increase the static and dynamic response of a structure. The behaviour becomes unstable when a small increase in the mean wind generates a large response in the structure. In other words this instability occurs when the frequency response function (FRF) $H(\omega) \to \infty$. The inverse of the FRF is called the impedance function, $\hat{\mathbf{E}}_\eta(\omega, V)$ and instability points is then obtained when the determinant of the impedance function goes towards zero

$$det(\hat{\mathbf{E}}_\eta(\omega, V)) \to 0 \tag{2.37}$$

The non-dimensional impedance matrix for the identification of possible stability limits are given by

$$\hat{\mathbf{E}}_\eta(\omega_r, V_{cr}) = \begin{bmatrix} 1 - k_{ae_{zz}} - (\frac{\omega_r}{\omega_z})^2 & -k_{ae_{z\theta}} \\ -k_{ae_{\theta z}} & 1 - k_{ae_{\theta\theta}} - (\frac{\omega_r}{\omega_\theta})^2 \end{bmatrix} + 2i \begin{bmatrix} (\zeta_z - \zeta_{ae_{zz}})\frac{\omega_r}{\omega_z} & -\zeta_{ae_{z\theta}}\frac{\omega_r}{\omega_z} \\ -\zeta_{ae_{\theta z}}\frac{\omega_r}{\omega_\theta} & (\zeta_\theta - \zeta_{ae_{\theta\theta}})\frac{\omega_r}{\omega_\theta} \end{bmatrix} \tag{2.38}$$

where

$$k_{ae_{zz}} = \frac{\rho B^2}{2\tilde{m}_z}(\frac{\omega_z(V)}{\omega_z})^2 H_4^* \frac{\int_{L_{exp}} \phi_z^2 dx}{\int_L \phi_z^2 dx} \qquad k_{ae_{z\theta}} = \frac{\rho B^3}{2\tilde{m}_z}(\frac{\omega_z(V)}{\omega_z})^2 H_3^* \frac{\int_{L_{exp}} \phi_z \phi_\theta dx}{\int_L \phi_z^2 dx} \tag{2.39}$$

$$k_{ae_{\theta\theta}} = \frac{\rho B^4}{2\tilde{m}_\theta}(\frac{\omega_\theta(V)}{\omega_\theta})^2 A_3^* \frac{\int_{L_{exp}} \phi_\theta^2 dx}{\int_L \phi_\theta^2 dx} \qquad k_{ae_{\theta z}} = \frac{\rho B^3}{2\tilde{m}_\theta}(\frac{\omega_\theta(V)}{\omega_\theta})^2 A_4^* \frac{\int_{L_{exp}} \phi_\theta \phi_z dx}{\int_L \phi_\theta^2 dx} \tag{2.40}$$

$$\zeta_{ae_{zz}} = \frac{\rho B^2}{4\tilde{m}_z}(\frac{\omega_z(V)}{\omega_z}) H_1^* \frac{\int_{L_{exp}} \phi_z^2 dx}{\int_L \phi_z^2 dx} \qquad \zeta_{ae_{z\theta}} = \frac{\rho B^3}{4\tilde{m}_z}(\frac{\omega_z(V)}{\omega_z}) H_2^* \frac{\int_{L_{exp}} \phi_z \phi_\theta dx}{\int_L \phi_z^2 dx} \tag{2.41}$$

$$\zeta_{ae_{\theta\theta}} = \frac{\rho B^4}{4\tilde{m}_\theta}(\frac{\omega_\theta(V)}{\omega_\theta}) A_2^* \frac{\int_{L_{exp}} \phi_\theta^2 dx}{\int_L \phi_\theta^2 dx} \qquad \zeta_{ae_{\theta z}} = \frac{\rho B^3}{4\tilde{m}_\theta}(\frac{\omega_\theta(V)}{\omega_\theta}) A_1^* \frac{\int_{L_{exp}} \phi_\theta \phi_z dx}{\int_L \phi_\theta^2 dx} \tag{2.42}$$

The equations above show instabilities depend on aerodynamic derivatives. For long-span bridges there exist four instability phenomenons.

2.7.1 Static Divergence

This is a static phenomena ($\omega_n = 0$). Static divergence can be seen as a static buckling phenomena in the torsional direction. When it occurs the self exited aerodynamic moment exceeds the divergence limit causing the cross section to loose its torsional stiffness and buckle. Static divergence is a result of a negative aerodynamic stiffness in torsion which means A_3^* is positive and causes total torsional stiffness to go to zero. What happens is as the section rotates the aerodynamic moment increase as fast or faster than the resisting forces from the torsional stiffness of the section, resulting in the section flipping over.

The static divergence stability limit can be found by inserting $\omega_r = 0$ and $\omega_z \to \infty$ into equation (2.38).

2.7.2 Dynamic Stability Limit in Torsion

In pure torsion the only modeshape vector is $\phi(x) = \begin{bmatrix} 0 & 0 & \phi_\theta \end{bmatrix}^T$. The resonant frequency ω_r will then be equal to the first natural frequency in torsion.

Dynamic instability in torsion can only occur for positive values of A_2^*. Positive values of A_2^* means negative aerodynamic damping, which results in the aerodynamic forces increasing in the direction of motion as velocity increases, adding energy to the system. When the negative aerodynamic damping is larger than the positive structural damping there is no damping left to take energy out of the system and displacement goes towards

infinity, as energy is preserved as kinetic and elastic potential energy.

The torsional stability limit can be found by inserting $\omega_r = \omega_\theta(V_{cr})$ and $\omega_z \to \infty$ into equation (2.38).

2.7.3 Galloping

Galloping is an unstable behaviour that only contains oscillating motion perpendicular to the wind direction. It occurs due to negative aerodynamic damping and a positive H_1^*. The negative aerodynamic damping makes the force in the direction of motion increase as the velocity increases. The modeshape vector for this phenomena is $\phi = \begin{bmatrix} 0 & \phi_z & 0 \end{bmatrix}^T$. The resonant frequency will be equal to the natural frequency of the first vertical mode.

The galloping stability limit can be found by inserting $\omega_r = \omega_z(V_{cr})$ and $\omega_\theta \to \infty$ into equation (2.38).

2.7.4 Flutter

Flutter is an instability phenomena that couples multiple vibration modes. Bi-modal flutter is usually a coupling between the first torsional and vertical mode into one dynamic deflection shape and it occurs when these modes have close eigenfrequencies. What happens is that the aerodynamic stiffness changes the total stiffness of the system which in turn changes the eigenfrequencies. When two or more eigenfrequencies coincide the aerodynamic effects present, but not significant in one mode may become significant to the other mode as the modes interact and vice versa. For example the change in lift with regard to rotation may not be significant if the torsional eigenfrequency is not close to the vertical eigenfrequency, but as the eigenfrequencies coincide the increased lift from the rotation may act as a harmonic force on the vertical mode exactly hitting the vertical resonance frequency. Selbergs formula as portrayed below can be used to roughly approximate the flutter stability limit of a bridge.

$$V_{cr} = 0.6B\omega_\theta \left\{ \left[1 - (\tfrac{\omega_z}{\omega_\theta})^2\right] \tfrac{(\tilde{m}_z \tilde{m}_\theta)^{\frac{1}{2}}}{\rho B^3} \right\}^{\frac{1}{2}} \tag{2.43}$$

Where $\tilde{m}_z$ is modally equivalent and evenly distributed mass in the vertical direction and $\tilde{m}_\theta$ is modally equivalent and evenly distributed rotational inertia in the longitudinal direction.

Motion induced instability occurs when $det(\hat{\mathbf{E}}_\eta(\omega, V)) \to 0$, to produce bi-modal vertical and torsional flutter aerodynamic stiffness must be so that

$$\omega_r = \omega_z(V_{cr}) = \omega_\theta(V_{cr}) \tag{2.44}$$

To obtain an exact solution to the critical wind speed for flutter instability there is no known analytical solution and iterations are needed to solve the equations from the impedance matrix.

2.8 Identification of Static Coefficients

The static coefficients are the unknown coefficients in equation 2.13. They can be identified by static tests, where the cross section is rotated and the coefficients becomes functions of the angle, α.

$$\begin{bmatrix} C_D(\alpha) \\ C_L(\alpha) \\ C_M(\alpha) \end{bmatrix} = \frac{2}{\rho V^2 DL} \begin{bmatrix} F_D \\ \frac{D}{B} F_L \\ \frac{D}{B^2} M \end{bmatrix} \tag{2.45}$$

Physically it means the static coefficients relate the measured forces to a chosen reference area, with a characteristic width and height, multiplied by the stagnation pressure of the flow. From the physical interpretation we can infer the static coefficients are often smaller than one for aerodynamic bodies.

2.9 Identification of Aerodynamic Derivatives

There exist some methods on how to identify the ADs from forced vibration test data. It is possible to find ADs by studying the phase angle between the self excited forces and the motion of the section. A different method is to consider the complex Fourier amplitudes of the self excited forces and relate these to the ADs. There are some uncertainties using these methods that may result in significant estimation errors. A better method could be to use a time domain method, where the model for the self excited forces is fitted to the time series of the test by use of the least square method(Siedziako et al., 2017).

The aerodynamic derivatives were proposed by Scanlan and Tomko(1971) to characterise the self-excited forces acting on a bridge and are usually identified from wind tunnel experiments(Scanlan and Tomko, 1971).

$$D_{SE} = P_1 \dot{r}_y + P_2 \dot{r}_\theta + P_3 r_\theta + P_4 r_y + P_5 \dot{r}_z + P_6 r_z \tag{2.46a}$$

$$L_{SE} = H_1 \dot{r}_z + H_2 \dot{r}_\theta + H_3 r_\theta + H_4 r_z + H_5 \dot{r}_y + H_6 r_y \tag{2.46b}$$

$$M_{SE} = A_1 \dot{r}_z + A_2 \dot{r}_\theta + A_3 r_\theta + A_4 r_z + A_5 \dot{r}_y + A_6 r_y \tag{2.46c}$$

The relationship between the equivalent ADs, which are given in equations 2.32 and 2.33, and the true ADs, which are given in equations 2.35 and 2.36, is

$$\begin{bmatrix} P_1 \\ P_2 \\ P_3 \\ P_4 \\ P_5 \\ P_6 \end{bmatrix} = \frac{1}{2}\rho V^2 B \begin{bmatrix} \frac{K_y}{V} & 0 & 0 & 0 & 0 & 0 \\ 0 & \frac{K_\theta B}{V} & 0 & 0 & 0 & 0 \\ 0 & 0 & K_\theta^2 & 0 & 0 & 0 \\ 0 & 0 & 0 & \frac{K_y^2}{B} & 0 & 0 \\ 0 & 0 & 0 & 0 & \frac{K_z}{V} & 0 \\ 0 & 0 & 0 & 0 & 0 & \frac{K_z^2}{B} \end{bmatrix} \begin{bmatrix} P_1^* \\ P_2^* \\ P_3^* \\ P_4^* \\ P_5^* \\ P_6^* \end{bmatrix} \tag{2.47a}$$

$$\begin{bmatrix} H_1 \\ H_2 \\ H_3 \\ H_4 \\ H_5 \\ H_6 \end{bmatrix} = \frac{1}{2}\rho V^2 B \begin{bmatrix} \frac{K_z}{V} & 0 & 0 & 0 & 0 & 0 \\ 0 & \frac{K_\theta B}{V} & 0 & 0 & 0 & 0 \\ 0 & 0 & K_\theta^2 & 0 & 0 & 0 \\ 0 & 0 & 0 & \frac{K_z^2}{B} & 0 & 0 \\ 0 & 0 & 0 & 0 & \frac{K_y}{V} & 0 \\ 0 & 0 & 0 & 0 & 0 & \frac{K_y^2}{B} \end{bmatrix} \begin{bmatrix} H_1^* \\ H_2^* \\ H_3^* \\ H_4^* \\ H_5^* \\ H_6^* \end{bmatrix} \tag{2.47b}$$

$$\begin{bmatrix} A_1 \\ A_2 \\ A_3 \\ A_4 \\ A_5 \\ A_6 \end{bmatrix} = \frac{1}{2}\rho V^2 B^2 \begin{bmatrix} \frac{K_z}{V} & 0 & 0 & 0 & 0 & 0 \\ 0 & \frac{K_\theta B}{V} & 0 & 0 & 0 & 0 \\ 0 & 0 & K_\theta^2 & 0 & 0 & 0 \\ 0 & 0 & 0 & \frac{K_z^2}{B} & 0 & 0 \\ 0 & 0 & 0 & 0 & \frac{K_y}{V} & 0 \\ 0 & 0 & 0 & 0 & 0 & \frac{K_y^2}{B} \end{bmatrix} \begin{bmatrix} A_1^* \\ A_2^* \\ A_3^* \\ A_4^* \\ A_5^* \\ A_6^* \end{bmatrix} \tag{2.47c}$$

Where K_y, K_z and K_θ is the reduced frequency in their respective directions.

The test rig control the model, and by forcing the model in sinusoidal motion in one direction only, the following is obtained:

$$r_y(t) = r_{y0}e^{i(\omega_y t+\phi_y)}, r_z(t) = r_\theta(t) = 0 \tag{2.48a}$$

$$r_z(t) = r_{z0}e^{i(\omega_z t+\phi_z)}, r_y(t) = r_\theta(t) = 0 \tag{2.48b}$$

$$r_\theta(t) = r_{\theta 0}e^{i(\omega_\theta t+\phi_\theta)}, r_y(t) = r_z(t) = 0 \tag{2.48c}$$

The total forces under a certain wind velocity can be expressed as a sum of different contributions:

$$Q_{tot}(r, \dot{r}, \ddot{r}, V, u, w) = Q_G + Q_I(\ddot{r}) + Q_S(V) + Q_B(V, u, w) + Q_{SE}(V, r, \dot{r}) \tag{2.49}$$

where Q_G is the static load due to self weight, $Q_I(\ddot{r})$ is the inertia forces and $Q_S(V)$ is the mean wind forces. $Q_B(V, u, w)$ is the buffeting forces and $Q_{SE}(V, r, \dot{r})$ is the self excited forces.

Here the desired forces is the self excited. The gravity forces and the inertia forces disappear from an in-wind test by subtracting the forces from a still air test. This is called the "Wind-NoWind-method" (Siedziako, 2018). The mean wind forces can be taken out by removing the mean value of the measured forces. The buffeting forces may in this case be neglected because of the smooth flow in the wind tunnel. This is how measured self excited forces are found from measured total forces.

By substituting equation 2.48b into equation 2.46 the following is obtained:

$$D_{SE,z} = P_5\dot{r}_z(t) + P_6 r_z(t) \tag{2.50a}$$

$$L_{SE,z} = H_1\dot{r}_z(t) + H_4 r_z(t) \tag{2.50b}$$

$$M_{SE,z} = A_1\dot{r}_z(t) + A_4 r_z(t) \tag{2.50c}$$

This can be rewritten into matrix form

$$\mathbf{Q}_{SE,z} = \mathbf{X}_z\mathbf{D}_z \tag{2.51}$$

where

$$\mathbf{D}_z = \begin{bmatrix} P_5 & H_1 & A_1 \\ P_6 & H_4 & A_4 \end{bmatrix} \tag{2.52}$$

$$\mathbf{X}_z = \begin{bmatrix} \dot{r}_{z,1} & r_{z,1} \\ \vdots & \vdots \\ \dot{r}_{z,n-1} & r_{z,n-1} \end{bmatrix} \tag{2.53}$$

$$\mathbf{Q}_{SE,z} = \begin{bmatrix} D_{SE,z,1} & L_{SE,z,1} & M_{SE,z,1} \\ D_{SE,z,2} & L_{SE,z,2} & M_{SE,z,2} \\ \vdots & \vdots & \vdots \\ D_{SE,z,n-1} & L_{SE,z,n-1} & M_{SE,z,n-1} \end{bmatrix} \tag{2.54}$$

The latter matrix is self excited forces due to motion in the z-direction. n represents the number of sampling points in the time history. $\mathbf{X}_z$ represents the motion, and $\dot{r}_z$ can be approximated by a numerical differentiation on the displacements history r_z. The method is called the forward differential method.

$$\dot{r}(n) = \frac{r(n+1) - r(n)}{\Delta t} = \frac{r(n+1) - r(n)}{1} * f_s \tag{2.55}$$

The method generates a numerical error with order $O(\Delta t^2)$, where Δt is the sampling time interval and f_s is the sampling frequency. The numerical differentiation results in n-1 velocity points. The only unknown is $\mathbf{D}_z$. It is possible to obtain this matrix by a least square approximation of the error term

$$\epsilon_z = \mathbf{Q}_{SE,z,measured} - \mathbf{Q}_{SE,z} = \mathbf{Q}_{SE,z,measured} - \mathbf{X}_z\mathbf{D}_z \tag{2.56}$$

The error arises from the assumption that the self excited forces depend linearly on displacements and velocities as seen in equation 2.46 while this is not really the case. The square of the error is found by a matrix operation

$$\epsilon_z^T\epsilon_z = \left(\mathbf{Q}_{SE,z,measured} - \mathbf{X}_z\mathbf{D}_z\right)^T\left(\mathbf{Q}_{SE,z,measured} - \mathbf{X}_z\mathbf{D}_z\right) = \mathbf{E}_z \tag{2.57}$$

and the error is minimised when the differentiation is zero

$$\frac{\partial \mathbf{E}_z}{\partial \mathbf{D}_z} = -2\mathbf{X}_z^T\mathbf{Q}_{SE,z,measured} + 2\mathbf{X}_z^T\mathbf{X}_z\mathbf{D}_z = 0 \tag{2.58}$$

so

$$\mathbf{D}_z = \left(\mathbf{X}_z^T\mathbf{X}_z\right)^{-1}\mathbf{X}_z^T\mathbf{Q}_{SE,z,measured} \tag{2.59}$$

This has to be repeated in the two other degrees of freedom, so by substituting equation 2.46a instead of 2.46b the matrix becomes

$$\mathbf{D}_y = \begin{bmatrix} P_1 & H_5 & A_5 \\ P_4 & H_6 & A_6 \end{bmatrix} \tag{2.60}$$

is found. To find the last six ADs substitute equation 2.46c instead of 2.46b and the matrix becomes

$$\mathbf{D}_\theta = \begin{bmatrix} P_2 & H_2 & A_2 \\ P_3 & H_3 & A_3 \end{bmatrix} \tag{2.61}$$

(Siedziako et al., 2017)

2.10 Wind Tunnel Effects

Wind is the flow of air on a large scale. It is highly affected by the surrounding environment where local topography and temperature makes the largest difference. Temperature changes the density of the air, and the topography affects the velocity and wind pattern. This is the natural effects, in the wind tunnel there are other effects that needs to be considered to make the test as realistic and natural as possible. The most important effects will be discussed in the next sections. It appears the influence of the laboratory environment or the operational conditions is an important issue to be considered and may significantly affect the results of the testing(Sarkar et al., 2009). Results of comparative studies between wind tunnels and testing methods indicate that a relative variation of the order of ten to twenty percent in critical velocity for a section was possible(Caracoglia et al., 2009), showing the uncertainty of the wind tunnel results.

2.10.1 Boundary Layer

This effect is caused by the friction between the air and the boundary in the wind tunnel. This effect is called boundary layer flow and it is a flow pattern that simulates the outdoor flow system. As we see from figure 2.12 the velocity changes approximately quadratic with the distance from the surface. At approximately 200 mm the velocity is constant and the effect doesn't affect the wind velocity.

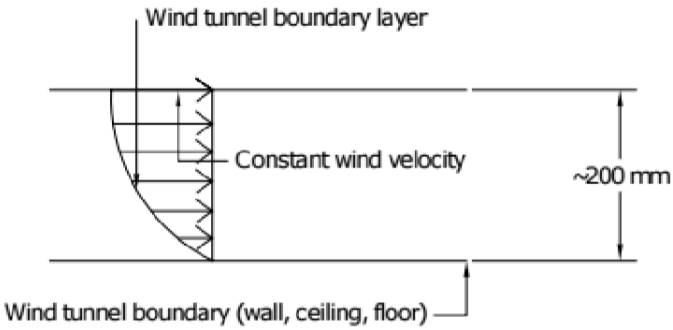

Figure 2.12: Wind tunnel boundary layer(Horg and Aas, 2016).

2.10.2 Blockage

Because the wind tunnel has a relatively small cross section area, the wind flow around measurement equipment or the model will be obstructed. The wind velocity will increase around bodies and create forces. The blockage ratio is often given as $\frac{S}{C}$ where S is the reference area of the model and C is the cross sectional area of the wind tunnel.

For blockage ratios less than 6%, it is shown that the effects of blockage on pressure distribution and the drag coefficient are small and that the Strouhal number is unaffected by blockage. For blockage ratios in the range 6-16%, there is considerable distortion of the flow due to blockage and the effects are complex. The pressure distribution is of a different form and the Strouhal number changes. Conflicting influences may result in a blocked drag coefficient which is not very different from that at no blockage(West and Apelt, 1982) however it has been shown the magnitude of blockage effect on drag coefficient may be significant even at a 5% blockage ratio(Takeda and Kato, 1992).

2.10.3 End Plates

End plates is used in wind tunnel testing so the wind flow is two-dimentional over the whole model. This is done by preventing the fluid outside the model to flow into testing area and to keep the wake two-dimentional. This demands the end plate diameter to be at least 8,5 times larger than the body depth normal to the flow(Kubo et al., 1989). In this thesis this is not a problem, because the model span the entire width of the wind tunnel, causing the walls of the tunnel to work as end plates.

2.11 Scaling Laws

Fluid mechanics is more heavily involved with experimental testing than other disciplines because the analytical tools currently available to solve momentum and energy equations are not capable of providing accurate results. This is particularly evident in turbulent,

separating flows. The solutions obtained by utilizing techniques from computational fluid dynamics with the largest computers available yield only fair approximations for turbulent flow problems, hence the need for experimental evaluation and verification(Elger and Roberson, 2016). Testing of scaled models build on certain assumptions that allow for scaling of size and forces.

2.11.1 Buckingham Π Theorem and Dimensional Analysis

In 1915 Buckingham showed that the number of dimensionless parameters needed to correlate the variables in a given process is equal to n - m, where n is the number of variables involved and m is the number of basic dimensions included in the variables. Buckingham referred to the dimensionless parameters as π-groups.

Dimensional analysis is the process for applying π-groups to analysis, experiment design, and the presentation of results(Elger and Roberson, 2016). The wind tunnel testing that are to be conducted relies on the legitimacy of the use of dimensionless parameters for scaling to yield accurate results.

2.11.2 Geometric Similtude

Similtude is the theory of predicting prototype performance from model observations. Geometric similtude means that the model is an exact geometric replica of the prototype(Elger and Roberson, 2016). In wind tunnel testing of bridge cross sections geometric similtude means the cross section of the model and the cross section of the full scale prototype has to be congruent while the length can be accounted for by using force per length unit.

2.11.3 Scaling Wind Tunnel Model

The dimensions of the model is determined by the size of the wind tunnel and the maximum wind velocity in the tunnel. This gives the geometric scale:

$$\lambda_L = \frac{L_{WT}}{L_{FS}} \tag{2.62}$$

where WT stands for wind tunnel scale and FS for full scale.

2.11.4 Reduced Frequency and Reduced Velocity

The structural non-dimensional frequency is often referred to as the reduced frequency and it is given as

$$K_r = \frac{\omega B}{V} = \frac{2\pi f B}{V} \tag{2.63}$$

The reduced velocity is given as

$$V_r = \frac{V}{\omega B} = \frac{V}{2\pi f B} \tag{2.64}$$

The reduced frequency and velocity is used for comparison between the full scale structure and the wind tunnel model.

$$\frac{V_{FS}}{\omega_{FS} B_{FS}} = \frac{V_{WT}}{\omega_{WT} B_{WT}} \tag{2.65}$$

2.11.5 Reynolds Number

The Reynolds number is a measure for turbulence in a fluid. Reynolds number is a dimensionless number, and is the ratio between inertia forces and viscous forces.

$$Re = \frac{inertia forces}{viscous forces} = \frac{\rho D V}{\mu} = \frac{V D}{\nu} \tag{2.66}$$

Methods to take Reynolds number into account is to change the wind velocity and to change the roughness of the surface of the model. It is also possible to do wind tunnel testing in a pressurized wind tunnel, increasing the density of the air and so increasing the Reynolds number(Schewe and Larsen, 1998).

2.11.6 Strouhal Number

The Strouhal number is relating the vortex shedding frequency to the flow velocity for a certain body shape. Strouhal number is a dimensionless number, useful when analysing oscillating unsteady fluid flow dynamics.

$$St = \frac{\omega L}{V} \tag{2.67}$$

The Strouhal number is a measure of the ratio of the inertia forces due to the unsteadiness of the flow or local acceleration to the inertia forces due to changes in velocity from one point to another in the flow view. Matsuda et al. showed the Strouhal number of a cross section may depend on the Reynolds number of the flow(Matsuda et al., 2001).

It has been shown the Strouhal number for a twin deck section may gradually increase with increasing gap-width due to the change of flow regime around the bridge deck(Kwok et al., 2012).

2.11.7 Scruton Number

The Scruton number is defined as

$$Sc = \frac{2\xi m_e}{\rho b_{ref}^2} \tag{2.68}$$

where ξ is the damping of the system, m_e is the mass per unit length, ρ is the density of the fluid and b_{ref} is the characteristic length of the system.

The Scruton number is considered to be important for the vortex shedding response. With a high enough Scruton number vortex shedding is rarely a problem, bridges may typically

have a Scruton number around ten.

Here follows an attempt to shed light on the Scruton number. Scruton number is a mix of damping and inertial mass per length over force creating mass per length. High Scruton numbers yield low risk for vortex shedding problems. Obviously damping will decrease vibration in most or all cases, so the interesting part is the masses per length. Having a high ratio between said masses may indicate that the fluid is not heavy enough to cause a relatively high acceleration of the heavier body. In case of a large mass and low stiffness like in a suspension bridge the vibrations may be mass controlled, requiring a low wind speed and vortex shedding load frequency to cause resonance. Having a heavy bridge in low wind speed there might not be enough energy in the wind to maintain large vibrations in spite of any damping. In case of a heavy and stiff body subjected to a relatively low density flow chances are the flow is less significant than if the flow was relatively dense as a both heavy and stiff body would need a large energy transfer per time(high effect) from the flow to keep vibrating in spite of any damping and this energy would have to come from kinetic energy in the flow. Note that even if a structure like the Tacoma narrows bridge seems heavy to the human eye it might not have a high enough Scruton number to withstand vortex shedding vibrations.

2.12 Reynolds Dependency

A common assumption in wind engineering is that the flow around bluff and sharp edged bodies is independent of Reynolds Number, Re. An important practical implication of this assumption is that aerodynamic parameters such as lift and drag coefficients may be obtained from low speed wind tunnel model tests and applied directly to the prototype structure. Tests conducted in a pressurised wind tunnel capable of reproducing typical model scale($Re \approx 10^5$) and prototype conditions($Re \approx 10^7$) revealed pronounced Re effects in Strouhal number for the flow around a bluff and sharp edged bridge girder cross section. Similar Re effects are well known from the flow around circular cylinders(Schewe and Larsen, 1998). It has also been shown there are 2-D sections that behave as a bluff- or streamlined body, depending on Re and that slender bodies with sharp-edged cross-sections may also suffer pronounced Reynolds-number effects(Schewe, 2001).

Reynolds-number effects are caused by changes in the topological structure of the wake(Schewe, 2001). Drag forces on a body depend on the size of the wake behind the body. The size of the wake among other things depends on the location of the separation points. The location of the separation points are among other things dependent on the turbulence around the body and Reynolds number is a measure for turbulence. This is a mechanism of how Reynolds number may influence the drag forces on a section.

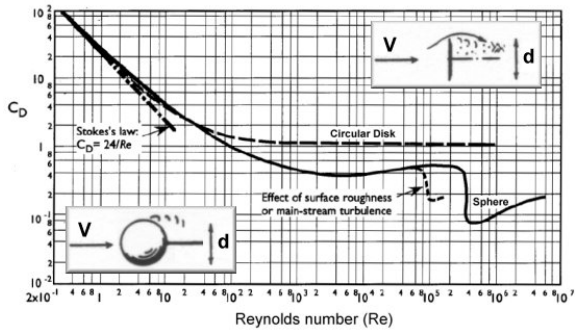

Figure 2.13: Variation of the drag coefficient with different Reynolds number. (Scott, 2005)

As seen from figure 2.13, the drag coefficient have a drop when the Reynolds number passes $3 - 4 * 10^5$. This dependency has to be known to make sure the model behave the same way as the full scale bridge because the Reynolds number of the full scale model would be larger than for the wind tunnel test.

It has been shown that conventional wind tunnel test results in the low Reynolds number region are conservative for wind resistant design of bridge decks(Matsuda et al., 2001).

2.13 Tuned Mass Damper (TMD)

The tuned mass damper is a device consisting of a mass, a spring and a damper that is attached to a structure. The aim is to reduce the dynamic response of the structure, specifically the worst case vibrations so they become less intense. TMD systems can add damping to a resonance frequency that is difficult or expensive to damp directly. The TMD works by adding a mass of for example 5% of a structures mass attached with a spring and a damper. The stiffness of the spring is so that the eigenfrequency of the TMD is close to that of the vibrations it should damp. When the system is excited the TMD will vibrate and energy will be damped out of the system. To have energy dissipate from the system as fast as possible the damper on the TMD must give enough damping to damp the motion, but not so much the added mass doesn't move relative to the structure as the goal is not to damp out the relative motion between the added mass and the structure but to remove energy from the structure as fast as possible which requires a nice balance between damping force and vibrational velocity. Adding an extra mass to a one DOF system makes it a two DOF system, if the eigenfrequency of the added mass is close to that of the initial system the two coupled modes for the new two DOF combined system will have eigenfrequencies close to the eigenfrequency of the original one DOF system, one lower and one higher. This is why a TMD may split a resonant frequency's peak in a spectral density. Figure 2.14 shows TMDs attached under the Millenium bridge to reduce pedestrian induced vibrations.

Figure 2.14: TMDs under the Millenium bridge, London. (Gerb, 2018)

2.14 Signal Filtering

There are several ways to filter a signal, two of the most common ways are low-pass and high-pass filtering. When filtering with a low-pass filter, all the high frequencies are filtered out. When filtering with a high-pass filter, all the low frequencies are filtered out. An ideal filtering process would filter out any frequency below or higher than a specified cut-off frequency. Making an ideal filter is hardly possible, so good approximations is the best one can achieve with the current technology. Figure 2.15 shows a visualisation of a low-pass filter where the x-axis represent the frequencies and the y-axis represent the scaling of the frequency amplitude. As the figure shows the filter attempts to filter out certain frequency intervals.

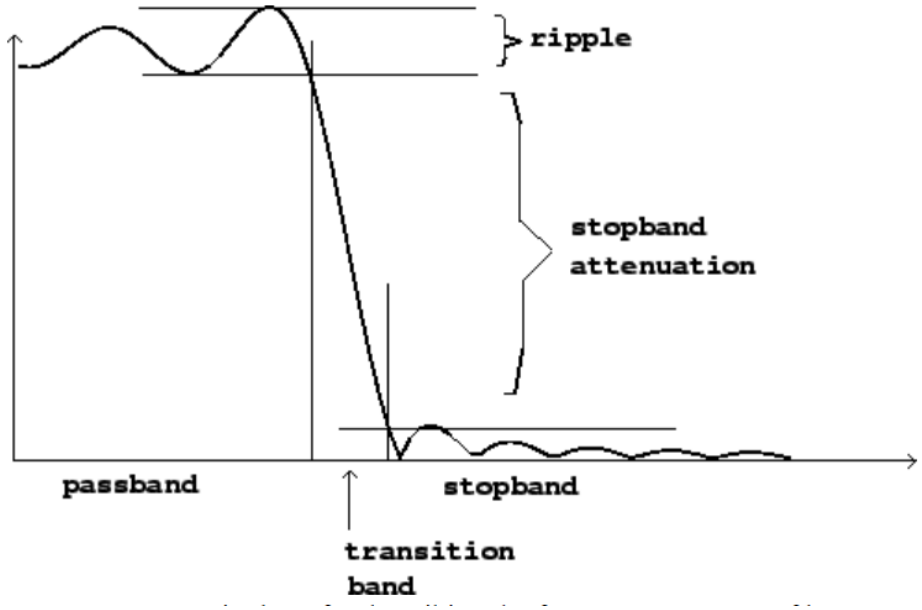

Figure 2.15: Example of a low-pass filter. (Puckette, 2006)

Figure 2.15 shows the frequency response of a low-pass filter. In the passband area the filter should leave the output as the input. Here the ripple represents the deviation from flatness in the passband area. In an ideal filter the ripple should be 0. The stopband frequency area is the area where the filter should filter out the frequencies and return an output without the frequencies. The stopband attenuation is the difference between the lowest gain in the passband area and the highest gain in the stopband area. The stopband attenuation value should be as large as possible. The drop between the passband and the stopband area should be as tight as possible to get a good filter. (Puckette, 2006)

2.15 Spectral Densities

To process recorded data we may use spectral densities. Here follows some useful relations to be aware of resulting in spectral densities(Newland, 2012).

Auto-correlation: The correlation of a process with itself with a time lag.

$$R_{xx}(\tau) = E[x(t)x(t+\tau)] \tag{2.69}$$

Cross-correlation: The correlation of a process with another process with a time lag.

$$R_{xy}(\tau) = E[x(t)y(t+\tau)] \tag{2.70}$$

Auto-spectral density: The Fourier transform of auto-correlation.

$$S_{xx}(\omega) = \int_{-\infty}^{\infty} R_{xx}(\tau) e^{-i\omega\tau} d\tau \tag{2.71}$$

Cross-spectral density: The Fourier transform of cross-correlation.

$$S_{xy}(\omega) = \int_{-\infty}^{\infty} R_{xy}(\tau) e^{-i\omega\tau} d\tau \tag{2.72}$$

The auto- and cross-correlations introduce the assumption that the processes are stationary which means the underlying statistical distributions of the processes are constant.

It can be shown that if ergodicity, which means underlying statistics of a process can be found by long enough measurements and a long recording period is assumed the cross-spectral density of two processes may be written:

$$S_{xy}(f) = \frac{X(f)Y(f)}{\Delta f} = X(f)Y(f) * T \tag{2.73}$$

Where f is frequency in cycles per second, Δf is the smallest frequency increment derived from the measuring period and T is the measuring period. Note if X and Y is the same process then you get the auto-spectral density, this is frequently used in computations.

The area below a spectral density function is the variance of the processes the spectrums are derived from. An auto-spectral density function show how much different frequencies contribute to the overall response of a process.

2.16 Measurement of Damping from Free Vibration

Measurement of damping from free vibration builds on relating the damping ratio ζ to successive amplitudes. The logarithmic decrement δ is defined as the natural logarithm of the ratio between two peaks at time t_n and t_n+T. Figure 2.16 shows damped free vibration with successive peaks.

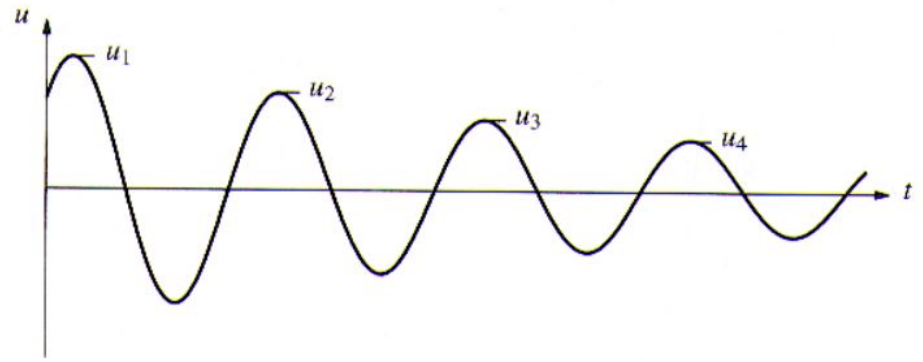

Figure 2.16: Damped free vibration and peak notation.

When measuring damping from successive peaks δ is taken as

$$\delta = ln\frac{u_n}{u_{n+1}} = 2\pi\frac{\zeta}{\sqrt{1-\zeta^2}} \approx 2\pi\zeta \quad for \quad \zeta \ll 1 \tag{2.74}$$

Improved accuracy for ζ is achieved for amplitudes that are several cycles apart especially for lightly damped systems, the logarithmic decrement can then be expressed as

$$\delta = \frac{1}{m}ln\frac{u_n}{u_{n+m}} \approx 2\pi\zeta \rightarrow \zeta \approx \frac{1}{2\pi m}ln\frac{u_n}{u_{n+m}} \tag{2.75}$$

If the damping is independent of amplitude this may give better accuracy as m is increased.

2.17 Argand Diagrams

An Argand diagram shows dynamic forces on a system. What is often talked about is the phase angle θ between the displacement vector and the load vector which can be seen in figure 2.17. The forces rotate in the complex plane with an angular velocity ω, therefore the time lag between the application of force and the displacement is a function of the phase angle θ and the angular velocity ω.

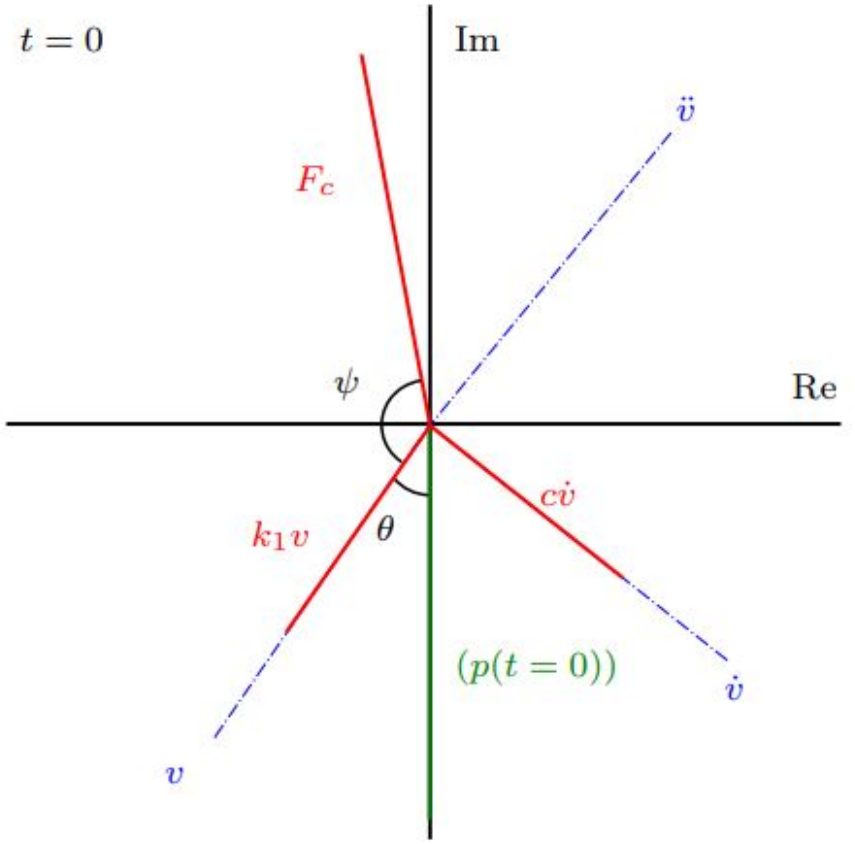

Figure 2.17: Argand diagram, at t=0 (load along y-axis).

The time lag as function of θ and ω becomes

$$T_{lag} = \frac{\theta}{\omega} \tag{2.76}$$

It can be seen from the Argand diagram in figure 2.17 that the stiffness forces are a function of displacement and has the same vector orientation in the complex plane while the damping forces are a function of velocity and has the same vector orientation in the complex plane. Inertia forces are not shown in figure 2.17 but they are function of acceleration and has the same vector orientation in the complex plane. We observe that the phase angle between displacement and further derivatives is ninety degrees.

At resonance the phase angle between load and displacement is ninety degrees which results in all energy added by loads being taken out by the damping while the stiffness and inertia forces cancel each other out in equilibrium.

If one for example for bi-modal flutter have two modes that has a ninety degree phase angle between between displacements one can see the cross terms that are in the damping matrices will work in the stiffness/inertia direction for the other mode and vice versa.

Chapter 3

Model Building and Design

The model was built in the structural engineering laboratory at NTNU, Department for Strutural Engineering. AutoCAD model of the wind tunnel model is shown in figure 3.1 below.

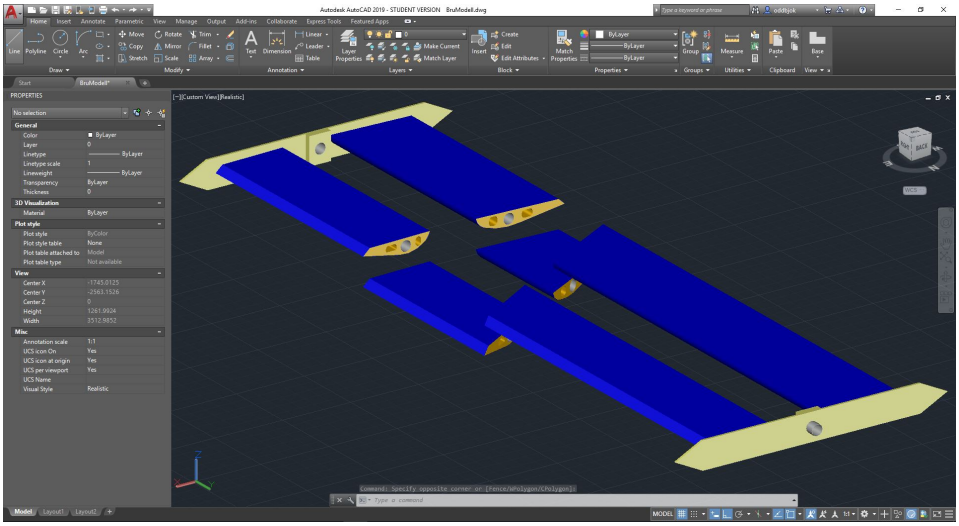

Figure 3.1: Sliced AutoCAD model of the wind tunnel model.

3.1 Choice of Cross Section

The choice of cross section landed on a suggestion by Multiconsult from a report for NPRA shown in figure 3.2 due to the cross section being conceptually interesting and untested. The cross section is an asymmetric twin deck with smoothly curved surfaces. The cross section is asymmetric to exploit the fact that the strongest winds will come from the sea

and therefore one believes the aerodynamic forces will be better dealt with by an asymmetric section(Multiconsult, 2015).

There are numerous decisive, interesting and challenging aspects of this cross section, some of which are the slot size between the decks, the effect of the asymmetry and the possibility for strong Reynolds dependency due to the curved surfaces.

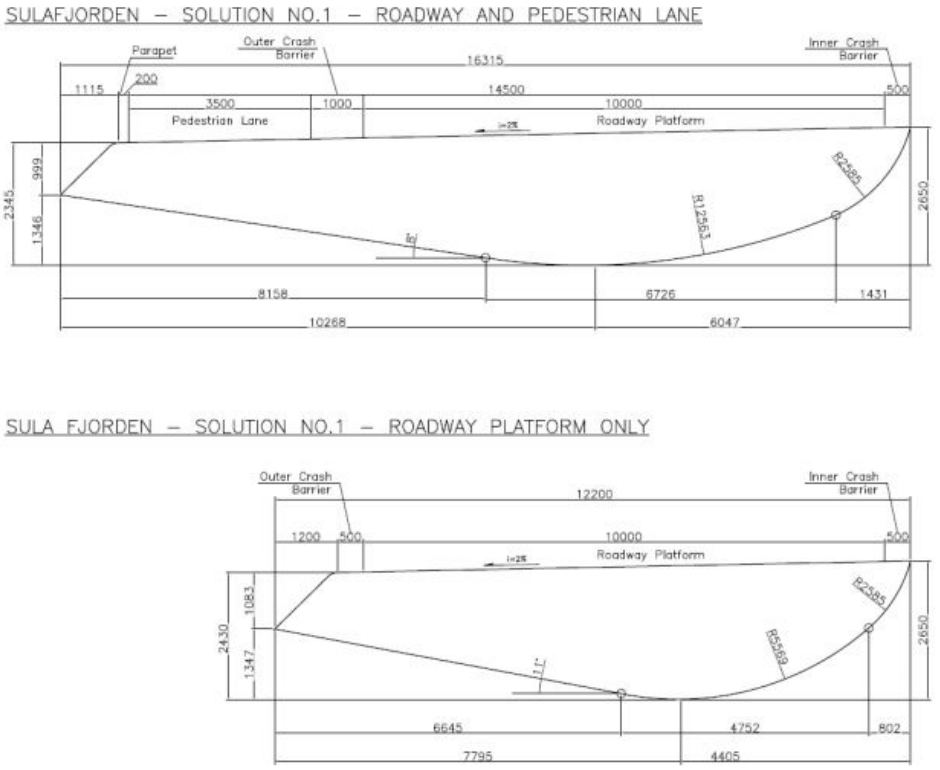

Figure 3.2: Sulafjorden deck boxes - Individual layouts. (Multiconsult, 2015)

From an aerodynamic standpoint, the asymmetry may increase stability as the centre gap is closer to the resultant lift force for the dominant NW winds, hence reducing the aerodynamic moments for the worst expected conditions(Multiconsult, 2015). The proposed configuration of the cross section is shown below in figure 3.3.

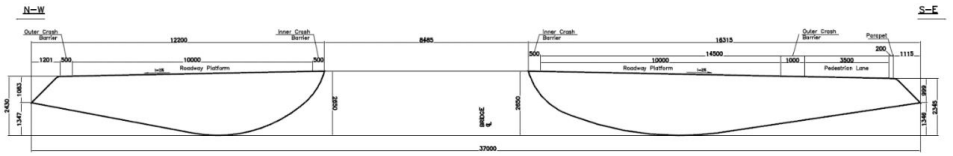

Figure 3.3: Deck overall configuration. The prevailing winds are expected from the open sea, i.e. from NW. (Multiconsult, 2015)

As we see from the figure above the curved edges are pointing inwards where the airflow is highly chaotic and dependent on the angle of the bridge deck relative to the wind while the sharp edges of the sections are pointing outwards making less of a mystery where the separation points may be. This may cause the cross section not to be as Reynolds dependent as feared due to curved edges. Rotating the cross section may give rise to more doubt regarding where the separation points will be, as the curved lower side may be rotated away from the wind and becoming ”harder to follow” for the wind.

The dimensions of the wind tunnel model is shown below in figure 3.4 and 3.5. The scaling is 1:50.

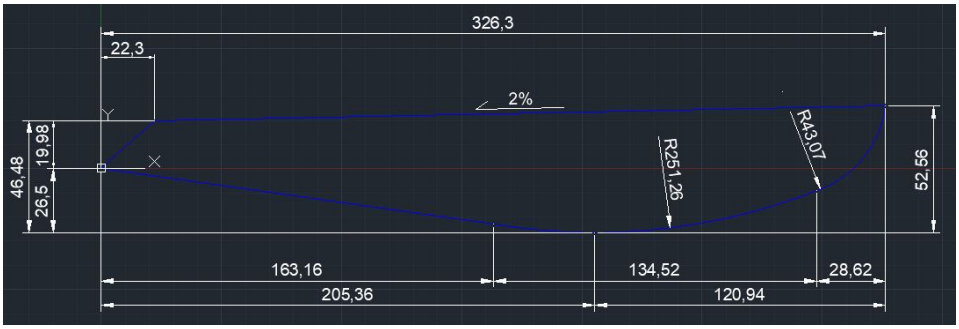

Figure 3.4: Model dimensions of girder with sidewalk. Dimensions in mm.

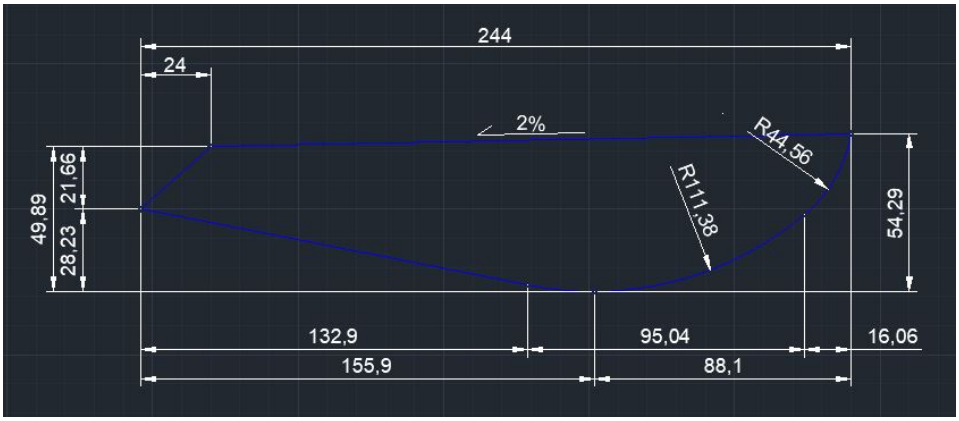

Figure 3.5: Model dimensions of girder without sidewalk. Dimensions in mm.

3.2 Building Procedure

To build the model it was decided to use an X-Carve router and cut the parts out of a light material called Divinycell which was recommended by the marine technology lab. First a CAD-model was made and developed through initial testing of the router and further development of designs. After producing sections of satisfactory quality the full model was produced in parts of 40 cm length and glued together with polyester adherent.

3.2.1 CAD Modelling

Fusion 360 by Autodesk was the preferred program for design of 3D models for carving. Fusion 360 is a bit like AutoCAD, but seems limited to fewer functions to make the drawing-carving interface easier to manage. First 2D drawings based on the Multiconsult designs were made as shown in figure 3.6. The Multiconsult drawings seemed to be hard or impossible to replicate exactly. When the curved surfaces was to be fitted after drawing all the straight lines as prescribed the fit could not be made with a continuous gradient between the curved parts so the lower curved part was done with the prescribed curvature, but the higher curved part was made as a five DOF spline where the translational and rotational DOFs are continuous on the lower end and the translational DOFs are continuous on the higher end. The difference was small and considered insignificant. The sections were made with cutouts in an attempt to save weight. The cutouts might have been a somewhat risky move, but it was believed on grounds of earlier testing of a similar light material and the same adherent on an aluminium surface(Horg and Aas, 2016) the model would still have the necessary strength to stay intact through building, transport and service.

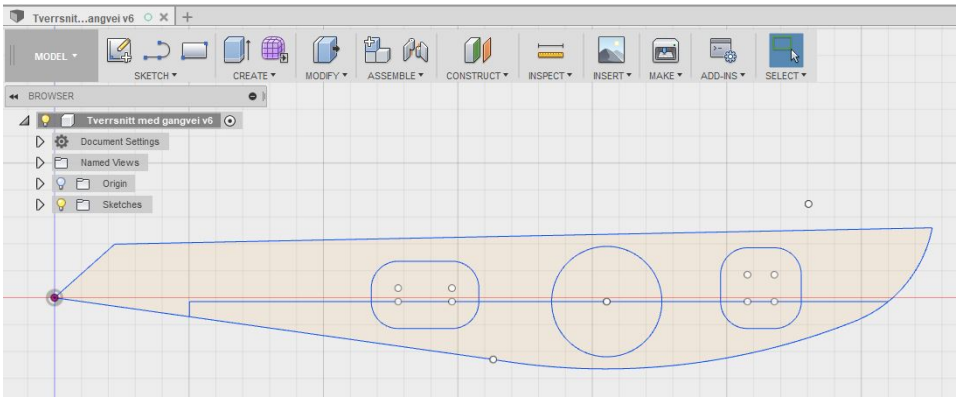

Figure 3.6: CAD cross section without sidewalk in Fusion 360.

To take the 2D drawing into the 3D domain the section was simply extruded, first by 100 mm as shown in figure 3.7, for testing and learning, then by 400 mm as shown in figure 3.8 for production of the full model. After the 3D shape was established different types of milling operations was explored, facing and parallel operations proved to be the most suitable ones for the purpose. Facing operations are good for removing large amounts of material at a fixed height and is restricted to a geometrical area on the model with some offset. Parallel operations run parallel to the model surface and is good for making curved surfaces and difficult shapes. Stepover length is how far the tool moves sideways before every pass. The facing operations were set with a five millimetre stepover to save time and achieve satisfactory quality while removing large amounts of material. The parallel operations for the pipe cutout and outer surfaces were time consuming and set with a two millimetre stepover to make up for the difficulties carving inclined areas without being able to rotate the tool. The less important cutouts were carved with a three millimetre stepover to save some time.

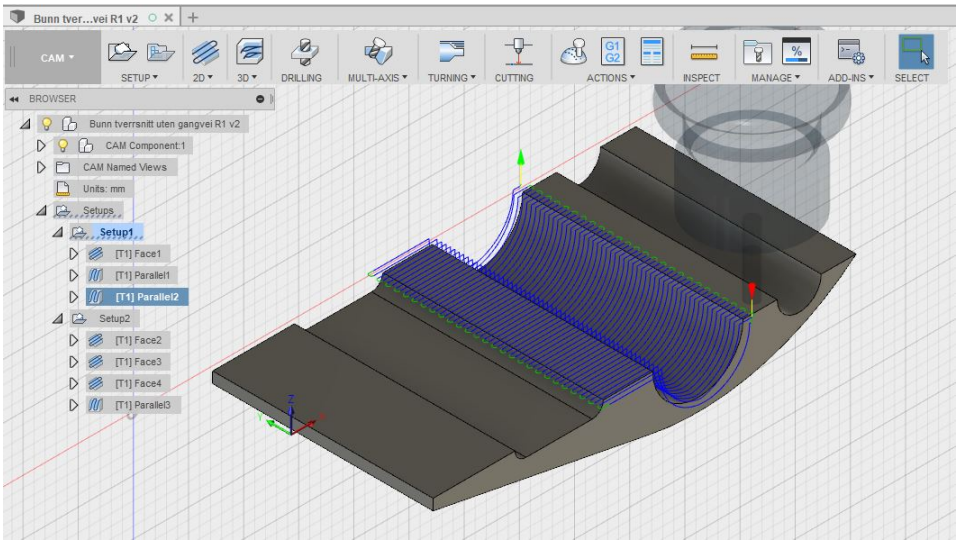

Figure 3.7: Early CAD-model showing milling paths.

Multiple milling operations are included in one setup, which becomes one piece of code the router may run. Every time the material must be turned or a tool is changed a new setup must be run by sending a new piece of code called Gcode to the router. Initially the milling was organised in two setups, one for each side, before and after turning the material. A flat headed tool was used as it was the only one available. A setup in Fusion 360 is converted into one piece of code and is run without stop when milling, making one milling process. As the tool had a flat head the parallel milling of the pipe cutout had to run orthogonal to the pipe direction to get satisfactory smoothness. However running parallel operations orthogonal to the pipe direction took a long time as the vertical speed of the router was significantly lower than the horizontal speed.

After receiving a ball headed tool the milling was changed to involve three setups where the third was for milling the cutouts with the ball headed tool. The ball headed tool allowed for milling parallel to the pipe direction and utilising the horizontal speed instead of the much slower vertical speed of the router. Milling in the pipe direction was also believed to give a higher precision to the model sections because vertical forces were avoided when the model had no support under the mid part, thereby avoiding significant vertical deflections due to milling.

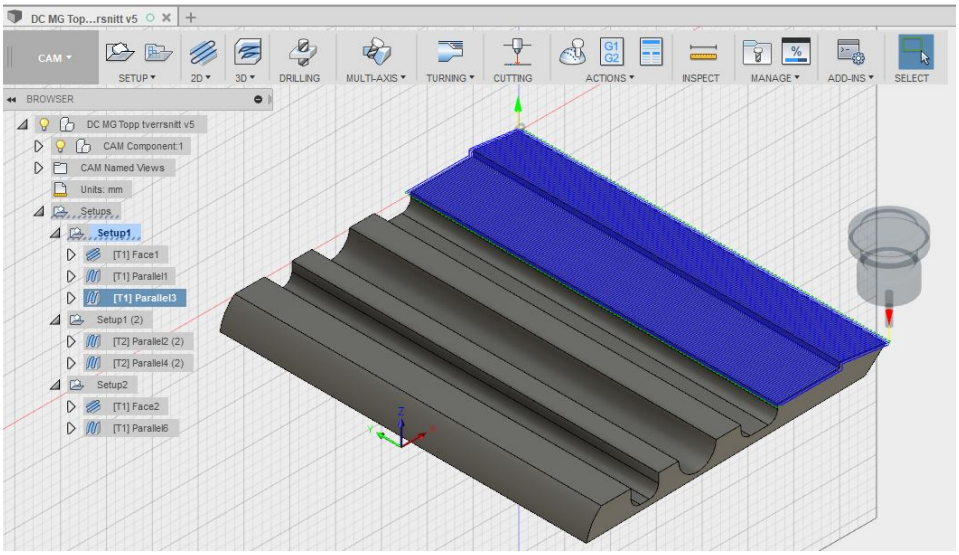

Figure 3.8: Final CAD-model for the top with sidewalk.

Using a milling direction parallel to the pipe direction presented a problem as the steep areas will achieve a very low precision for a stepover length achieving satisfactory precision when milling horizontally. The problem was neatly addressed by using the option ”machine steep areas” as shown in figure 3.9 which allows for using different stepover lengths within the same milling operation, where the stepover length is determined by the steepness of the area to be milled.

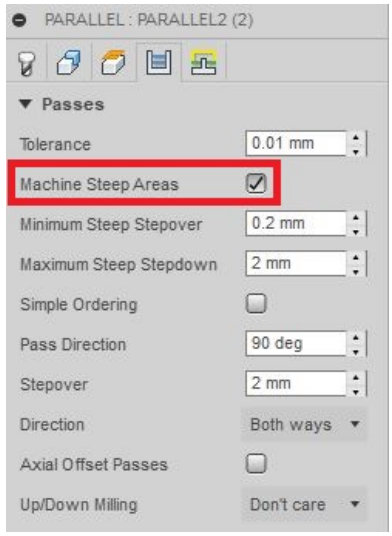

Figure 3.9: Figure showing passing options for a parallel milling operation

The problem of making a good match between the two sides, before and after turning the material, was addressed by making the exact material thickness irrelevant as origo was placed in the same physical point on the material for all milling processes. For the first process origo was on the top surface of the material and after turning the material for the second and third process origo was on the lower surface of the material. This solution caused any surplus or missing material thickness to be taken away by the first facing operation removing one aspect of uncertainty. However the Divinycell plates seemed to hold a very high standard so varying thickness would probably never have become a problem anyway.

3.2.2 Milling

The milling processes were exported from Fusion 360 and sent to the X-Carve router using a code format called Gcode and a program called Universal Gcode Sender pictured in figure 3.10, abbreviated UGS. Using UGS the X-Carve shown in figure 3.11 could be manually controlled and controlled using code based instructions. The router coordinate system had to be calibrated for every milling process instructing the router where in space it was to regard as origo, which had to be done according to the model in Fusion 360. This repeated manual calibration of origo was probably the largest source of error from the milling part of the building process.

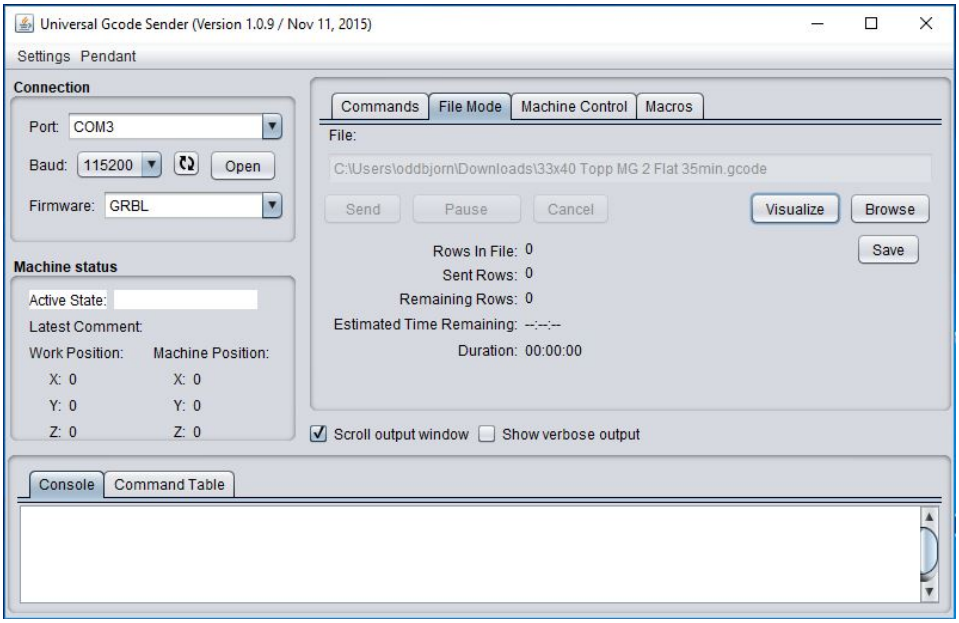

Figure 3.10: Graphical user interface of Universal Gcode Sender

First the router was tested using styrofoam boards. The styrofoam boards served well for learning because they were so soft that even if the tool was not rotating and the router moved full speed through the material nothing broke. There was a lot of small and big

failures as experience was gained on how to use the machine. For example it seemed like the firmware(see figure 3.10) had to be set to GRBL to open the USB port before it could be set to TinyG which was the file format exported from Fusion 360. The milling processes were made to compensate for the weaknesses of the router, for example deep and steep curved cuts were placed at the very end of the material such that if the tool would start struggling with the debth it could actually just break through the remaining material. The effectiveness and necessity of these measures will never be known as there is nothing to compare to and nothing broke.

Figure 3.11: The X-Carve milling rig used for making the model.

With a 40 mm diameter cutout the pipe would not fit due to some leftover material from the milling due to the tool not being able to achieve perfect smoothness. A 41 mm diameter cutout was tested and made almost a perfect fit with the 40 mm pipe. Figure 3.12 shows an early prototype that was successfully made after some trial and error. The connecting surfaces between the upper and lower part were first designed to be entirely flat for easy and fast milling, but this design proved to be very sensitive to small errors in the thickness of the lower part and the very thin edge got milled away due to approaching an infinitely small thickness and therefore very low strength. The new design with a vertical connecting surface as seen on the right side of the prototype in figure 3.12 worked well, but took some more time by complicating the milling processes as seen in figure 3.8.

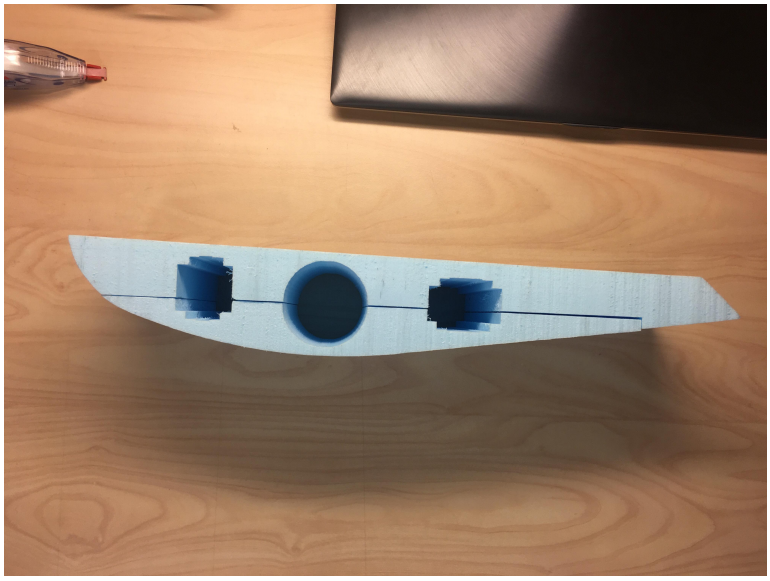

Figure 3.12: Early prototype milled in styrofoam to test machinery and milling techniques.

Finally for the full model there was twelve milling processes of varying duration. It was observed the Fusion 360 estimates of how long a process would take was too optimistic, especially for operations with a lot of vertcial movement the estimations were bad. The twelve processes are listed below in table 3.1.

No.	Part	Dimensions [cm]	Tool	Tool diameter [inch]	Duration [min]
1	Bottom	20x40	Flat	1/4	29
2	Bottom	20x40	Flat	1/4	8
3	Bottom	20x40	Ball	1/4	10
4	Top	25x40	Flat	1/4	29
5	Top	25x40	Flat	1/4	28
6	Top	25x40	Ball	1/4	9
7	Bottom w/sidewalk	26x40	Flat	1/4	33
8	Bottom w/sidewalk	26x40	Flat	1/4	9
9	Bottom w/sidewalk	26x40	Ball	1/4	10
10	Top w/sidewalk	33x40	Flat	1/4	33
11	Top w/sidewalk	33x40	Flat	1/4	35
12	Top w/sidewalk	33x40	Ball	1/4	11

Table 3.1: Table of milling processes.

The different milling tools are pictured below in figure 3.13. The tools were both utilised to achieve satisfying smoothness in the most effective manner. As seen in figure 3.13 the cutting part of the tools is not that high, which led to minor difficulties when milling deep

cuts. The lacking height of the tools were compensated for as far as possible by using facing operations to remove material over and around any deep cuts before the parallel milling operations commenced.

Figure 3.13: 1/4 inch flat and ball head tools.

The ball headed tool gave the opportunity to effectively mill the cutouts with motion parallel to the longitudinal direction using the machine steep areas function as shown in figure 3.14. The authors refrained from using the ball headed tool to machine the outer surfaces parallel to the pipe believing the air flow would be smoother with tracks in the wind direction instead of tracks in the longitudinal direction.

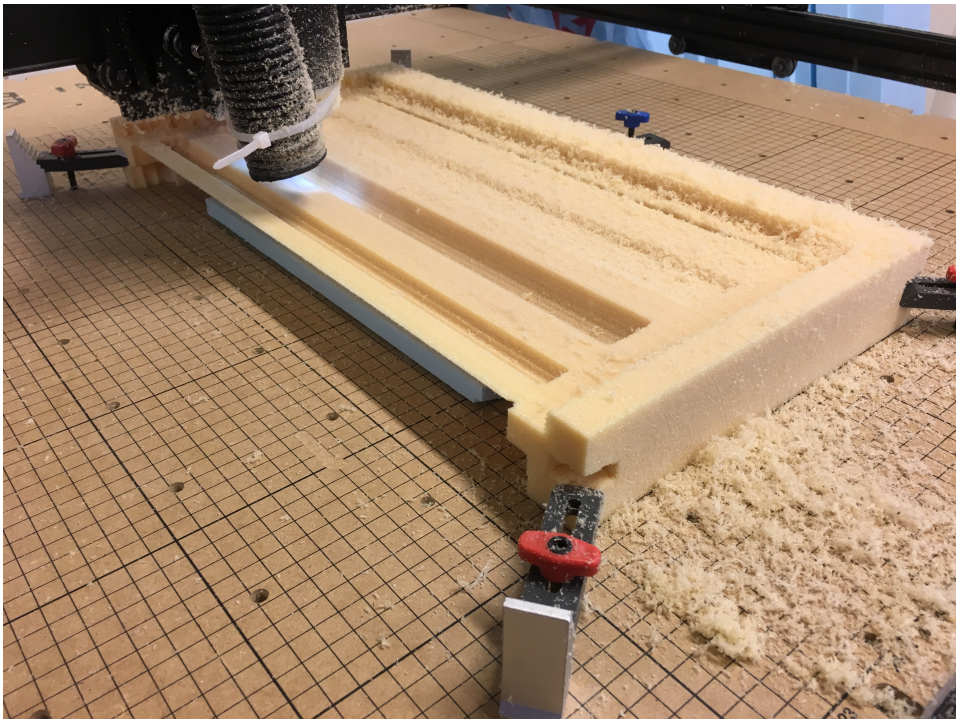

Figure 3.14: Milling of top without sidewalk in Divinycell.

3.2.3 Assembly

After milling all Divinycell parts the model was ready for assembly. The pipe was to be glued in between top and bottom sections before applying foil and mounting the sections on the end fittings.

To assemble the full model the following items was used:

- Divinycell 60kg/m^3
- Aluminium pipes 40 mm diameter 1 mm thick
- Polyester adherent
- Hardener for polyester
- Covering vinyl foil 3M wrap film 1080 series
- Plywood
- 3D-printed end mounts
- 3D-printed clips

First the polyester adherent had to be made ready before the gluing could begin. The polyester was mixed with 2% hardener to decrease the hardening time. With 2% hardener the polyester remained liquid for 30 minutes before becoming hard. Approximately 800 g of the polyester shown in figure 3.15 was used.

Figure 3.15: Chosen polyester and hardener.

Having 30 minutes to assemble each deck the assembly had to be done rather quickly and preparations proved to have been done a bit too quickly as we encountered practical challenges on the way and these had to be dealt with in a hurry. Examples of practical challenges were polyester going through the paper under the model and sticking to the metal surface underneath, having to glue both sides of a joint to ensure a good connection and the sheer amount of surface to be glued. After the assembly the model looked good in the end. The assembled parts are shown in figure 3.16. For later notice it is not recommended to mill 40 cm sections as this gives a large number of joints. Using longer

and fewer sections would be preferable. When gluing together a large amount of sections all having some degree of error the size of the expected maximum error increase with the amount of parts to be glued together. It was observed most parts made a great fit, but some were for example clearly leaving too much space around the pipe for the glue to fill.

Figure 3.16: Twin deck model after gluing.

To make the model smoother before foil application the joints where sanded to make sure there were no ill-shaped polyester spills, remains of paper or clear edges as seen in figure 3.17. The material was easy to work with and sanding went very well.

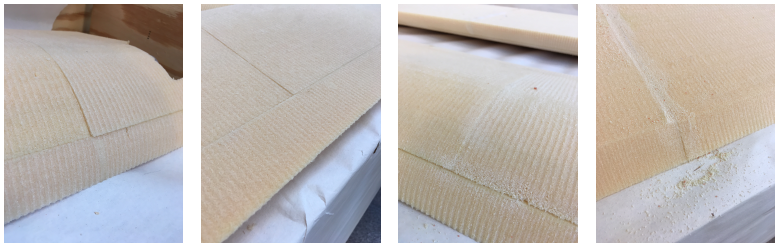

(a) **(b)** **(c)** **(d)**

Figure 3.17: Two joints before sanding and two joints after sanding.

Before applying foil to the entire model two early styrofoam models were used to practice foil application as seen in figure 3.18. A hot air gun was used to make the foil workable as prescribed by the manufacturer. At first the hot air gun was set to 600 degrees Celsius which made the foil melt quickly, then it was found a temperature of 400 degrees Celsius was suitable when watching the material and keeping some distance. Foil has to be applied gradually while making sure there are no bubbles or the bubbles will be very hard to remove. It is recommended to work the foil at the same time as applying heat.

(a) First test and foil applied with heat gun at 600 degrees Celsius.

(b) Second test and foil applied with heat gun at 400 degrees Celsius.

Figure 3.18: Testing of foil application on styrofoam models.

To make the full twin deck model the two decks had to be attached to the plywood. To achieve a good and flexible mount there was 3D printed end mounts for the aluminium pipes for easy attachment and detachment. Models for end mounting was provided by laboratory staff. The aluminium pipe was simply squeezed in the end mount by screws and help in place by friction. The 3D printer and the printed end mounts are shown in figure 3.19.

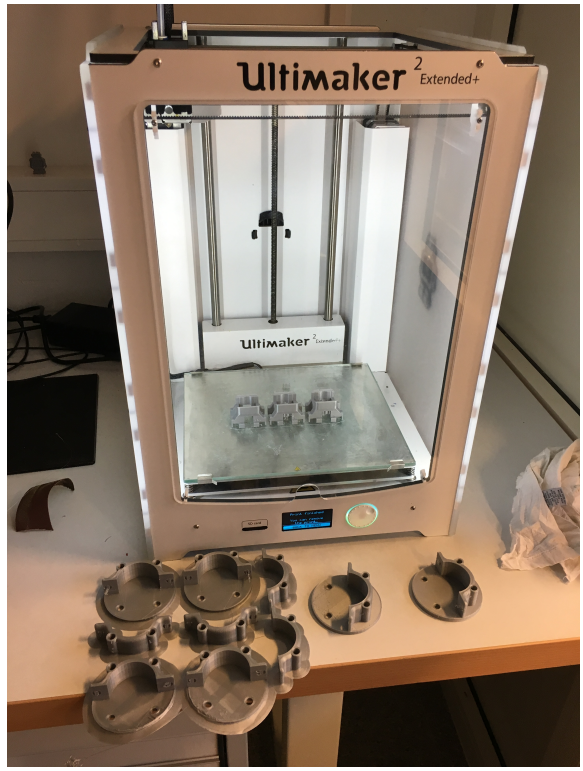

Figure 3.19: 3D printed end mounts for the aluminium pipes.

As the authors had some doubts about the torsional capacity of the friction based end mount solution clips were made to help holding the model in place and to facilitate assembly of the model, removing the need for measurements every time the plywood was to be detached or attached. Models for the clips were created by the authors in Fusion 360 using the sketches from the bridge cross section. The models for the clips are shown in figure 3.20.

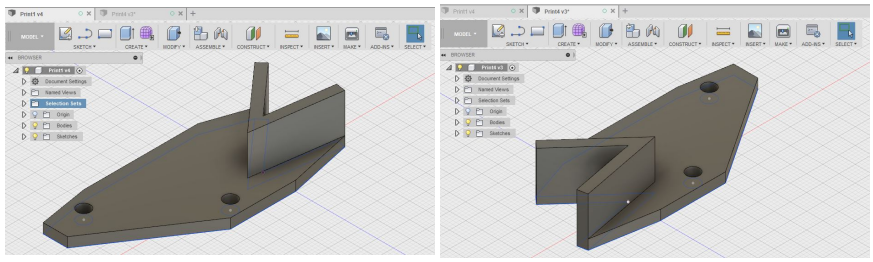

(a) **(b)**

Figure 3.20: Fusion 360 models of clips.

From the placement of the holes one can see the clips were designed to handle a maximum moment from a downward force from the model, but their capacity were probably tenfolds of what was necessary in all directions. The CAD models for the clips were exported from Fusion 360 as STL files and sent to the 3D printer using Cura slicing software. As figure 3.21 shows the clips were printed in PLA which is the most commonly used material for 3D printing. PLA is a biodegradable thermoplastic and easy to work with. The clips were printed using 100% infill density for high strength.

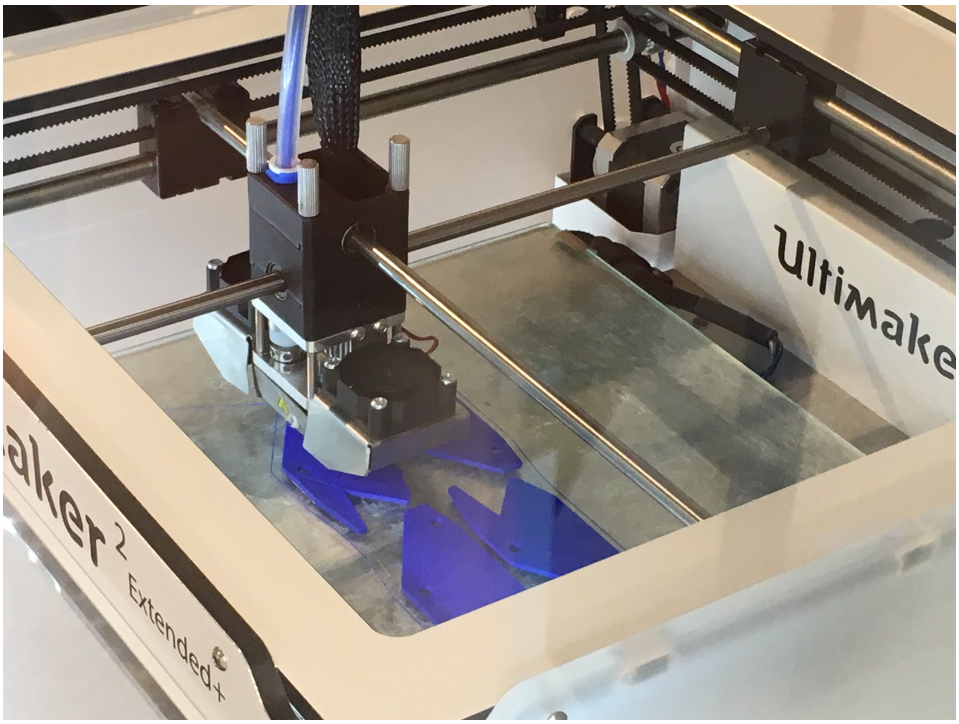

Figure 3.21: 3D printing of clips in progress.

Figure 3.22a shows the finished 3D printed clips. It was decided the clips should be smaller and they were modified to allow for more weight reduction when cutting the wood. The clips ended up as shown in figure 3.22c. As shown in figure 3.2 the inclination on the deck surface was to be 2%, this was fixed by levelling as shown in figure 3.22b. First the inclination was mistakenly set to two degrees but this was corrected to 2% later. Before cutting the wooden plates the model looked as in figure 3.22d.

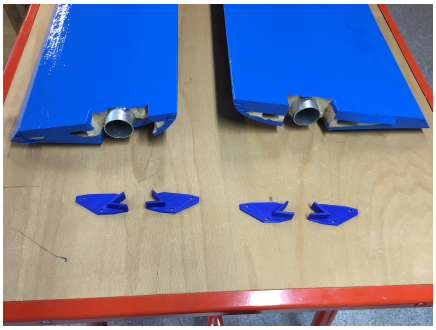

(a) Newly printed clips.

(b) Leveling of deck girders.

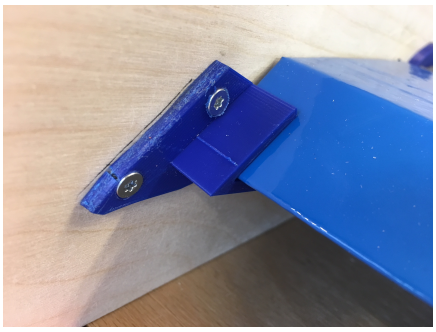

(c) Clip montage.

(d) Preliminary setup.

Figure 3.22: Pictures of model during assembly.

The model in its final configuration is presented in figure 3.23.

Figure 3.23: Model in final configuration.

3.3 Model Characteristics

Knowing model characteristics is good for considering if it is fit for testing and interpreting results. Knowing the weight is good for controlling that it is not too heavy for the load cells, knowing the lowest eigenfrequency is good for setting vortex shedding results in context and different results using different methods may say something about for example the success of the assembly process.

3.3.1 Analytical Frequency Estimation

Eigenfrequencies of the model can be approximated using calculated modal mass and modal stiffness. The analytical approximation is based on a large number of assumptions like Naviers hypothesis, uniformly distributed mass, linear modulus of elasticity and more. Being based on a number of assumptions analytical approximations may deviate from reality. Calculating modal parameters mass, stiffness and eigenfrequency can be taken as(Chopra, 2001):

$$M_n = \int_0^L m(x)[\phi_n(x)]^2 dx \tag{3.1}$$

$$K_n = \int_0^L EI(x)[\phi_n"(x)]^2 dx \tag{3.2}$$

$$K_n = \omega_n^2 M_n \tag{3.3}$$

Looking for the lowest frequency the mode shape is assumed to be $\phi(x) = sin(\frac{\pi x}{L})$.

Frequency of Aluminium Pipe

First to have some sort of benchmark the first eigenfrequency of the aluminium pipe is calculated.

Pipe properties:

- Density of aluminium: $2700 kg/m^3$
- Elasticity modulus of aluminium: 69 GPa
- Length of pipe: 2,664 m
- Outer diameter: 40 mm
- Thickness: 1 mm

Taking the pipe properties and inserting into equation 3.3 the following is obatined:

$$\omega_n = \sqrt{\frac{K_n}{M_n}} = \sqrt{\frac{\frac{\pi^4}{2L^3} E_{Alu} I_{Alu}}{\frac{L}{2} m}} = \sqrt{\frac{\pi^4 E_{Alu} I_{Alu}}{L^4 \rho_{Alu} A_{Alu}}} = 96,95\ rad/s \rightarrow f_n = 15,43\ Hz$$

Frequency of Pipe and Divinycell

Before calculating the eigenfrequencies the distributed masses must be known. The distributed masses were taken as the total masses of the girders divided by the length of the girders. As shown in figure 3.24 the mass of the girder without sidewalk was 2327 grams and the mass of the girder with sidewalk was 2712 grams.

(a) Girder without sidewalk. **(b)** Girder with sidewalk.

Figure 3.24: Weighing of model decks.

The frequencies of the girders with and without sidewalk taking into account pipe stiffness only and total mass was calculated. The eigenfrequency of the girder without sidewalk was approximated to 9,50 Hz and the eigenfrequency of the girder with sidewalk was approximated to 8,80 Hz.

To calculate the eigenfrequencies including the stiffness contribution of the Divinycell it is necessary to know the mechanical properties of the Divinycell. The mechanical properties according to Diab are listed in table 3.2 below. The elasticity modulus was taken as the minimum compressive modulus due to polymers having increasing modulus of elasticity and the glued joints always being able to transfer compression, however this was just a somewhat qualified and arbitrary decision.

Property	**Test Procedure**		**H45**	**H60**
Compressive Strength [MPa]	ASTM D 1621	Nominal	0,6	0,9
		Minimum	0,5	0,7
Compressive Modulus [MPa]	ASTM D1621-B-73	Nominal	50	70
		Minimum	45	60
Tensile Strength [MPa]	ASTM D 1623	Nominal	1,4	1,8
		Minimum	1,1	1,5
Tensile Modulus [MPa]	ASTM D 1623	Nominal	55	75
		Minimum	45	57
Shear Strength [MPa]	ASTM C 273	Nominal	0,56	0,76
		Minimum	0,46	0,63
Shear Modulus [MPa]	ASTM C 273	Nominal	15	20
		Minimum	12	16
Shear Strain [%]	ASTM C 273	Nominal	12	20
Density [kg/m^3]	ISO 845	Nominal	48	60

Table 3.2: Mechanical properties of Divinycell H according to Diab. (Diab, 2018)

To calculate the eigenfrequencies of the girders including the stiffness contribution of the Divinycell it is also necessary to know the second moments of area of the Divinycell cross sections. In figure 3.25 the mass properties of the cross sections are shown as found in AutoCAD. For simplicity the second moments of area about the x and y axes were taken as the second moments of area about the major and minor axes of the sections. Given the major and minor axes orientations seen in figure 3.25 the difference is considered negligible.

```
----------------   REGIONS   ----------------

Area:                      6642.3717
Perimeter:                 837.7874
Bounding box:            X: 496.0000  --  740.0000
                         Y: -28.2338  --  26.0600
Centroid:                X: 614.7159
                         Y: 3.4290
Moments of inertia:      X: 1435215.3945
                         Y: 2537772110.6013
Product of inertia:     XY: -14003722.9473
Radii of gyration:       X: 14.6993
                         Y: 618.1085
Principal moments and X-Y directions about centroid:
                         I: 1357112.2508 along [1.0000 0.0001]
                         J: 27781635.0164 along [-0.0001 1.0000]
```

(a) Mass properties of Divinycell without sidewalk.

```
----------------   REGIONS   ----------------

Area:                      9039.1166
Perimeter:                 1024.6119
Bounding box:            X: 0.0000  --  326.3000
                         Y: -26.4998  --  26.0600
Centroid:                X: 168.6436
                         Y: 3.3588
Moments of inertia:      X: 1744189.3458
                         Y: 327636316.5387
Product of inertia:     XY: -5012979.0154
Radii of gyration:       X: 13.8910
                         Y: 190.3851
Principal moments and X-Y directions about centroid:
                         I: 1642048.5621 along [1.0000 -0.0016]
                         J: 70557892.3789 along [0.0016 1.0000]
```

(b) Mass properties of Divinycell with sidewalk.

Figure 3.25: Mass properties of Divinycell cross sections from AutoCAD.

The frequencies of the girders with and without sidewalk using pipe and Divinycell stiffness and total mass was calculated. The eigenfrequency of the girder without sidewalk

was approximated to 9,77 Hz and the eigenfrequency of the girder with sidewalk was approximated to 9,09 Hz.

Frequency of Pipe, Divinycell and Foil

To calculate the eigenfrequencies of the girders including the stiffness contribution of the foil it is necessary to know the second moments of area of the foil cross sections, these were found in AutoCAD in the same way as the mass properties of the Divinycell cross sections. For simplicity the second moments of area about the x and y axes were taken as the second moments of area about the major and minor axes of the sections. Given the major and minor axes orientations the difference was considered negligible.

The frequencies of the girders with and without sidewalk using total(pipe, Divinycell and foil) stiffness and total mass was calculated. The eigenfrequency of the girder without sidewalk was approximated to 10,34 Hz and the eigenfrequency of the girder with sidewalk was approximated to 9,73 Hz.

Frequency with Point Mass

The frequencies of the girders with and without sidewalk using pipe stiffness and total mass plus a 143 gram point mass at mid span from an IPhone 6S was calculated. The eigenfrequency of the girder without sidewalk was approximated to 8,96Hz and the eigenfrequency of the girder with sidewalk was approximated to 8,37 Hz.

3.3.2 Frequency Estimation by Phone Application

The phone application VibSensor was used to measure eigenfrequencies of the girders. The phone, being an IPhone 6S, was laid on top of one girder at a time and used to record accelerations as the first mode was manually excited. The measurements produced the plots shown in figure 3.26 below.

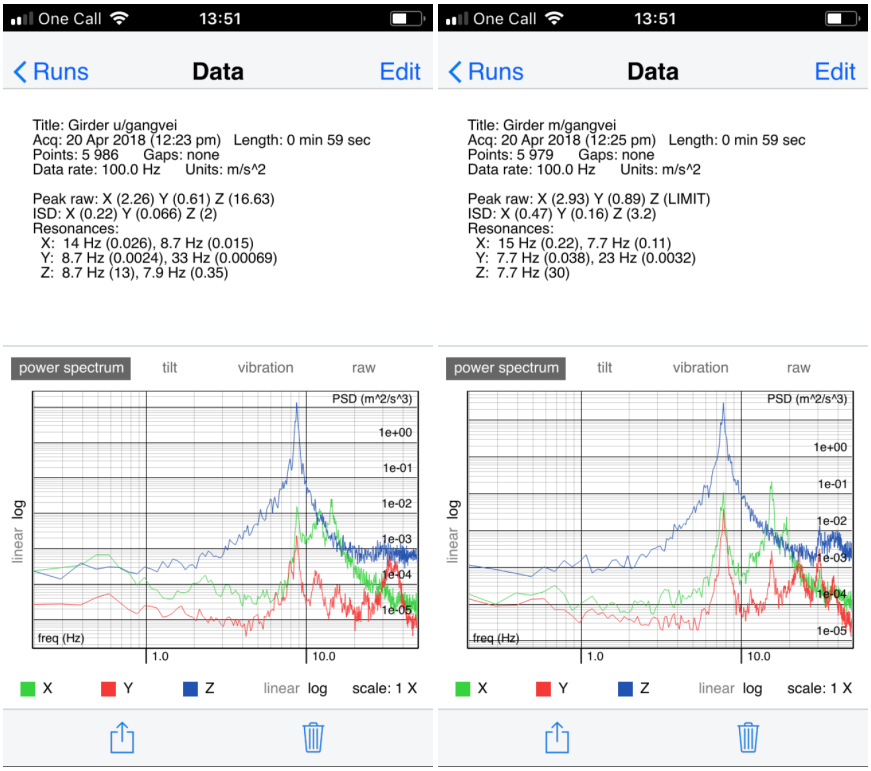

(a) Girder without sidewalk.

(b) Girder with sidewalk.

Figure 3.26: Power spectrums of girders using the app VibSensor.

As seen from figure 3.26 the measured eigenfrequency of the girder without sidewalk was 8,7 Hz and the measured eigenfrequency of the girder with sidewalk was 7,7 Hz.

3.3.3 Summary of Results

A summary of the gathered results is given below in table 3.3.

Stiffness	**Mass**	ω_1 **without sidewalk [Hz]**	ω_1 **with sidewalk [Hz]**
Pipe	Pipe	15,43	15,43
Pipe	Total	9,50	8,80
Pipe and Divinycell	Total	9,77	9,09
Total	Total	10,34	9,73
Pipe	Total + IPhone	8,96	8,37
VibSensor	Total + IPhone	8,7	7,7

Table 3.3: Table of estimated frequencies.

As shown in table 3.3 no calculated eigenfrequencies are as low as the measured eigenfrequencies. The difference between measurements and calculations may be partly because of bad joints in the model and a foil unstressed in the longitudinal direction, although this can not explain an error this large. The model was not entirely simply supported during measurements and modes may have been more complicated than the assumed sine shape due to the girders being fit to the mounting rack. More complex modes may for example in practice have increased the modal mass. The data from the phone application also shows the modes are not completely vertical. The model was subjected to impulse loading by hand.

For the record analytically estimated eigenfrequencies of mode two with a mode shape $\phi(x) = sin(\frac{2\pi x}{L})$ are listed in table 3.4 below.

Stiffness	**Mass**	ω_2 **without sidewalk [Hz]**	ω_2 **with sidewalk [Hz]**
Pipe	Pipe	61,73	61,73
Pipe	Total	37,99	35,19
Pipe and Divinycell	Total	39,07	37,38
Total	Total	41,35	38,94

Table 3.4: Table of estimated frequencies.

Chapter 4

Wind Tunnel Testing

Wind tunnel testing is widely used to investigate the properties of potential long span bridge decks. When doing aerodynamic design the procedures first step requires wind tunnel tests on deck sectional models:

- To measure the lift, drag and moment coefficients as a function of the angle of attack(α) to perform an optimization of the deck shape.
- To measure aerodynamic derivatives in order to verify the fulfilment of the bridge stability requirements.
- To investigate the vortex shedding excitation, analysing the maximum vibration level under lock-in conditions as a function of the Scruton number.

These steps are repeated until the aerodynamic stability is granted and the maximum vibration level at the real bridge Scruton number fulfils the limits of the design specifications. Once the deck optimization has been completed, wind tunnel tests to identify the aerodynamic admittance functions are performed allowing the numerical simulation of the full bridge response to turbulent wind. The most promising solution is then analysed in detail through an aeroelastic full bridge model in a wind tunnel. The results of the full aeroelastic model testing are compared with the numerical simulations in order to control the design(Diana et al., 2013).

In this thesis the lift, drag and moment coefficients and the aerodynamic derivatives are found for a twin deck section. Vortex shedding is also investigated but not explored in depth.

4.1 Experimental Setup

There is mainly two ways to test a bridge section in a wind tunnel: Free vibration and forced vibration. In a free vibration test the section is mounted on springs and is allowed

to vibrate freely in the air flow. In a forced vibration test the section is mounted on an actuator which moves the section in a prescribed motion. The method used in these experiments are forced vibration testing. Research show results obtained using the different methods for the same section may deviate due to amplitude dependency and wind tunnel characteristics(Sarkar et al., 2009)(Zhang et al., 2017). In a study of a streamlined deck for which the comparison was restricted to the analysis of different extraction methods in the same laboratory, relative differences in the critical velocity for coupled-mode flutter were affected by the bridge type and span length selected for simulation. These differences are limited within a ten to fifteen percent margin. For a bluff cross section the most important differences arise from testing method and amplitude dependency and differences in critical velocity for single mode instability may be as large as thirty percent(Caracoglia et al., 2009). Although the differences in aerodynamic derivatives for a section may range from negligibly small values to as much as fifty percent occurring as a result of either different laboratories, measurement methods and bridge type the predicted critical velocity values do not vary as much(Caracoglia et al., 2009).

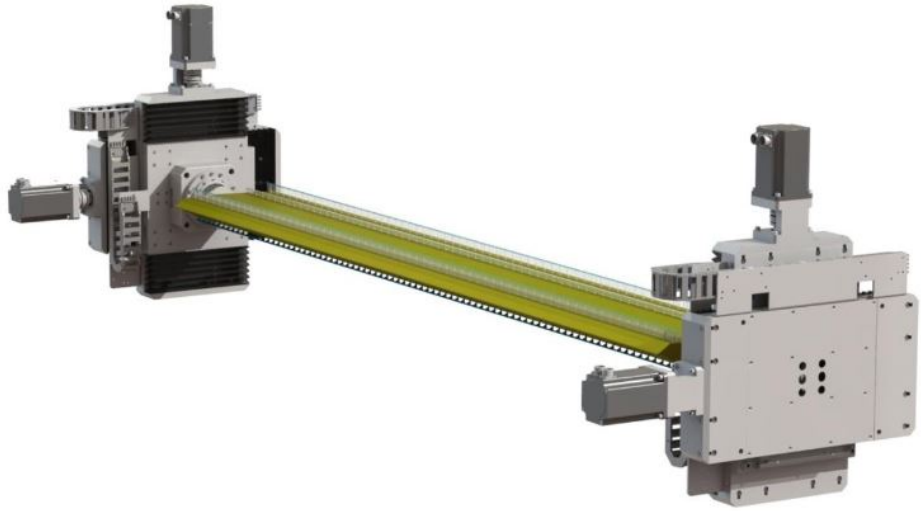

Figure 4.1: Basic working principle of a forced vibration rig: Bridge deck section model fixed between two internally connected actuators. (Siedziako, 2018)

As seen from figure 4.1 above the bridge section model will be mounted between the actuators. The section model will be forced into a prescribed motion, for example a sinusoidal rotational motion. The actuators have load cells attached to measure the forces from the model as the motion goes on. These actuators are able to handle very large forces and can easily move the section with a frequency of 5 Hz. The actuators can move up to $\pm$ 10 cm in the horizontal and vertical directions, while the torsional axis can travel $\pm$ 90 degrees. The induced motion profiles are very smooth since the control system generates third-order motion profiles, making the acceleration and velocity linear and quadratic, respectively(Siedziako, 2018). With a sufficiently small discretization of the sinusoidal

motion a linear acceleration will yield a very good approximation.

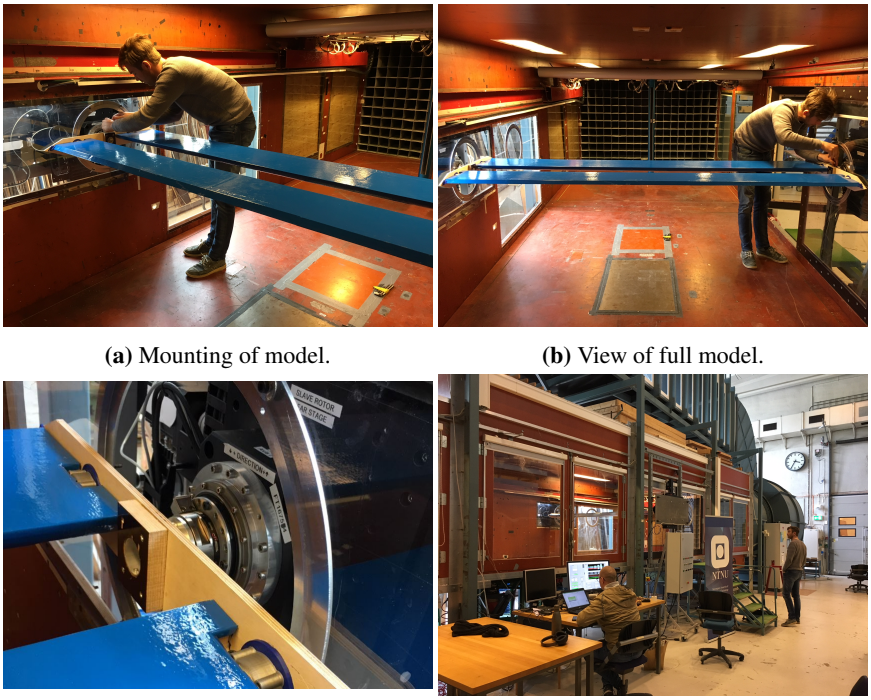

(a) Mounting of model.

(b) View of full model.

(c) Load cell on actuator.

(d) Wind tunnel.

Figure 4.2: Pictures from the EPT lab.

As seen in figure 4.2 the model was set up in the wind tunnel according to plan. The model was levelled by making the top of the wooden part horizontal.

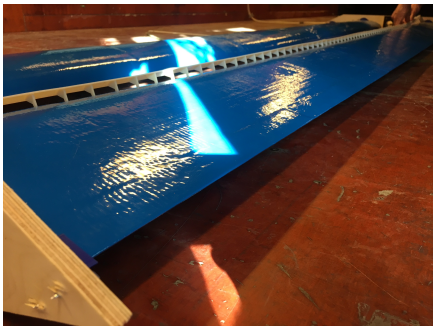

(a) Fitting of spoilers.

(b) Spoilers seen from below.

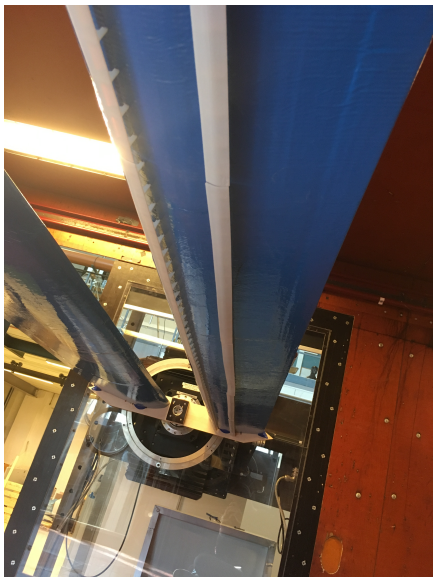

(c) Model with two spoilers.

Figure 4.3: Model with spoilers.

After testing of the initial configuration the model was turned around to test aerodynamic derivatives when wind comes from the other side. After testing for wind from both sides spoilers were attached as seen in figure 4.3 and the section was again tested for vortex shedding. To assess the possibility of damping out the vortex shedding vibrations improvised TMDs were attached to the girders as seen in figure 4.4. The TMDs weighed approximately 100 grams each and therefore was 4,3% and 3,7% of the weight of their respective girders, typically TMDs should weigh about 5% of the structures weight. The frequencies of the dampers were tunable by moving the coins in and out on the stick, changing the stiffness. The TMDs were tuned to approximately the same frequency as the girders by using the phone application VibSensor.

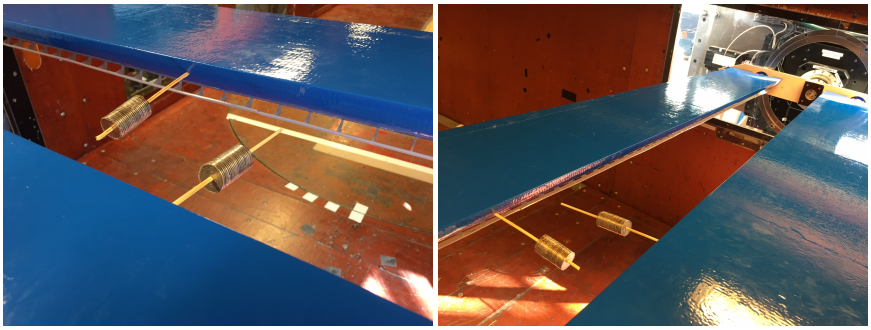

(a) TMDs attached. **(b)** Positioning of TMDs at mid span.

Figure 4.4: Improvised tuned mass dampers.

4.2 Test Description

The model was subjected to a series of tests to measure different characteristics. The tests were as shown in table 4.1. There are basically three different types of tests: Vortex shedding, static coefficients and aerodynamic derivatives. The vortex shedding tests simply increase the wind speed and record forces as the section starts vibrating due to vortex shedding. The tests for static coefficients keep a constant wind speed and incrementally change the angle of the model from minus five degrees to plus five degrees. The aerodynamic derivative tests move the section in harmonic motion either horizontally, vertically or in rotation about the longitudinal axis while the wind speed is kept constant. There were also tested for random motion, this tests are used to compare measured self excited forces with self excited forces calculated by the aerodynamic derivatives.

Also the load cells and the phone application VibSensor was used to gather data from the girders with and without dampers and the data was used to approximate the modal damping of the systems. The damped system was subjected to vortex shedding tests. It was also done a vortex shedding test with two sets of spoilers. The attachment of the TMDs and spoilers are shown in respectively 4.4 and 4.3.

Model configuration	Purpose	Motion	Wind [m/s]	Amplitude
Default	Vortex shedding	None	0-12	None
Default	Vortex shedding	None	8-0	None
Default	Static coefficients	Angular steps	0	+5/-5 deg
Default	Static coefficients	Angular steps	10	+5/-5 deg
Default	Static coefficients	Angular steps	8	+5/-5 deg
Default	Static coefficients	Angular steps	6	+5/-5 deg
Default	Static coefficients	Angular steps	4	+5/-5 deg
Default	Static coefficients	Angular steps	2	+5/-5 deg
Default	Vertical ADs	Single harmonic	0	+20/-20 mm
Default	Vertical ADs	Single harmonic	6	+20/-20 mm
Default	Vertical ADs	Single harmonic	10	+20/-20 mm
Default	Horizontal ADs	Single harmonic	0	+20/-20 mm
Default	Horizontal ADs	Single harmonic	6	+20/-20 mm
Default	Horizontal ADs	Single harmonic	10	+20/-20 mm
Default	Angular ADs	Single harmonic	0	+1/-1 deg
Default	Angular ADs	Single harmonic	6	+1/-1 deg
Default	Angular ADs	Single harmonic	10	+1/-1 deg
Default	Angular ADs	Single harmonic	0	+2/-2 deg
Default	Angular ADs	Single harmonic	6	+2/-2 deg
Default	Angular ADs	Single harmonic	10	+2/-2 deg
Default	Test assumptions	Random horizontal	10	Varying
Default	Test assumptions	Random vertical	10	Varying
Default	Test assumptions	Random angular	10	Varying
Default	Test assumptions	Random	10	Varying
Reversed	Vortex shedding	None	0-12-0	None
Reversed	Static coefficients	Angular steps	0	+5/-5 deg
Reversed	Static coefficients	Angular steps	6	+5/-5 deg
Reversed	Static coefficients	Angular steps	10	+5/-5 deg
Reversed	Vertical ADs	Single harmonic	0	+20/-20 mm
Reversed	Vertical ADs	Single harmonic	6	+20/-20 mm
Reversed	Vertical ADs	Single harmonic	10	+20/-20 mm
Reversed	Horizontal ADs	Single harmonic	0	+20/-20 mm
Reversed	Horizontal ADs	Single harmonic	6	+20/-20 mm
Reversed	Horizontal ADs	Single harmonic	10	+20/-20 mm
Reversed	Angular ADs	Single harmonic	0	+1/-1 deg
Reversed	Angular ADs	Single harmonic	6	+1/-1 deg
Reversed	Angular ADs	Single harmonic	10	+1/-1 deg
Reversed	Angular ADs	Single harmonic	0	+2/-2 deg
Reversed	Angular ADs	Single harmonic	6	+2/-2 deg
Reversed	Angular ADs	Single harmonic	10	+2/-2 deg
Spoiler	Vortex shedding	None	0-12-0	None
Spoiler and TMD	Vortex shedding	None	0-12-0	None
Two spoilers	Vortex shedding	None	0-12-0	None

Table 4.1: Table of test procedures.

4.3 Data Processing

Initially voltage from the load cells on the actuators is logged. MATLAB is used to convert the voltage series into forces, the forces are transformed from the local coordinate system of the load cells into a coordinate system similar to the global coordinate system that rotates with the section model, the forces are then transformed from the rotating coordinate system to the stationary global coordinate system. Finally the forces are transformed into the coordinate system used throughout this thesis with an x-axis parallel to the longitudinal axis, a horizontal y-axis and a vertical z-axis. θ is rotation about the longitudinal axis. Figure 4.5 shows how the different coordinate systems are placed and the position of load cell FT16754 placed at the ”road side” of the wind tunnel and load cell FT16752 at the ”front side” or entrance side of the wind tunnel.

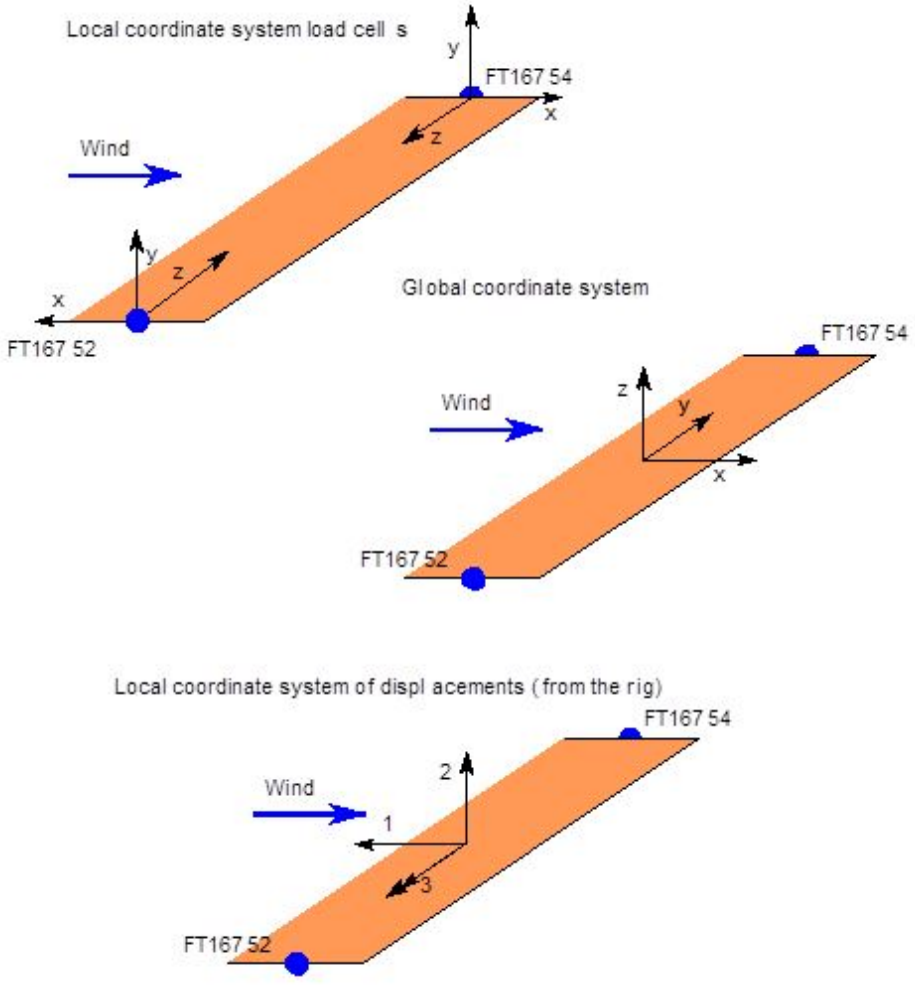

Figure 4.5: Local and global coordinate systems for the wind tunnel testing.

For the vortex shedding tests forces are simply logged as the model is held still and wind speed is increased, forces will then be higher when the model is subjected to vortex shedding frequency coinciding with a natural frequency. Reading the forces and watching for which wind speeds forces go up one may see when vortex shedding takes place and how large the effect is.

For the static coefficients tests and the aerodynamic derivatives tests the model is being subjected to constant wind speed while being subjected to some pattern of motion. The forces from a still air test is subtracted to remove bad calibration, gravity forces and inertia forces. Forces from a still air test is obtained subjecting the model to the pattern of motion in still air. After subtracting the forces from the still air test one is left with the wind forces on the section model. This is the same method used by Siedziako(Siedziako, 2018), called "Wind-NoWind" method. Because the wind flow is rather smooth and vortex shedding forces is minimized both buffeting forces and vortex shedding forces is neglected and/or filtered away. To extract the SE forces also the static forces is removed by subtracting the linear trend in the remaining forces and then the only remaining part of the total forces is the self excited. The self excited forces are used to extract the aerodynamic derivatives.

Static coefficients are found by changing the angle step by step from an angle of minus five degrees to an angle of plus five degrees as shown in figure 4.6. The static coefficients are given as a function of the angle of the model.

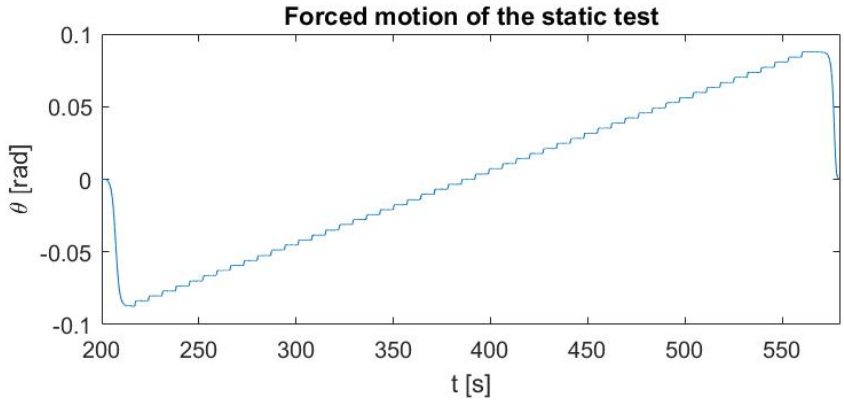

Figure 4.6: The forced motion of the static test.

Aerodynamic derivatives are found by subjecting the model to a single harmonic displacement in one direction per test. For every test the harmonic motion in one direction is done at multiple frequencies as shown in figure 4.7. For each frequency twenty motion cycles are made. The different frequencies are listed in table 4.2.

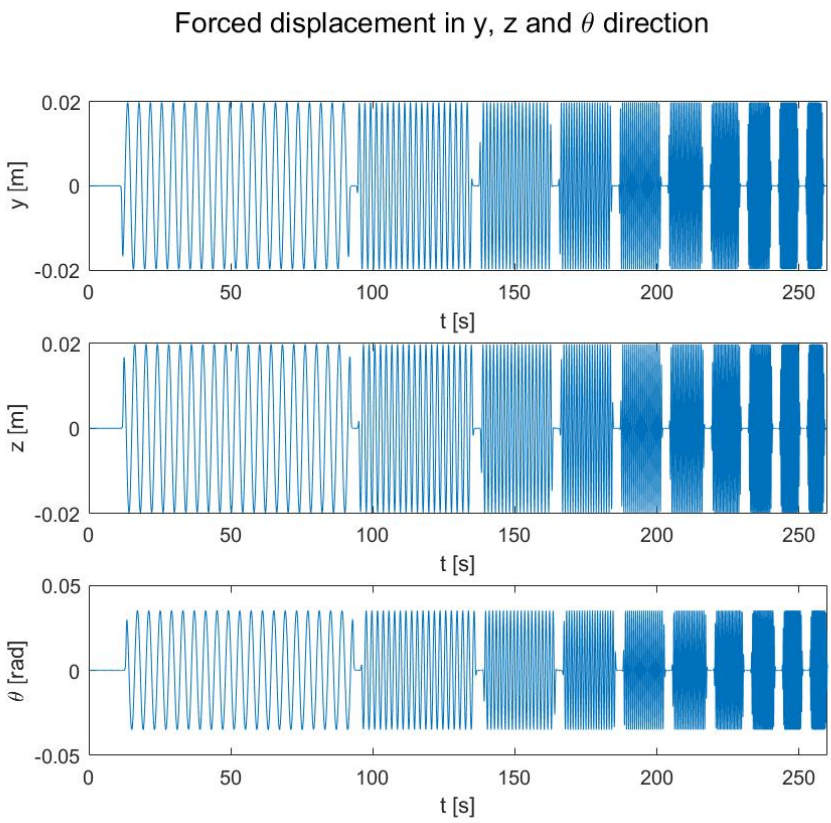

Figure 4.7: The forced displacement in the three different directions, y, z and θ.

Number	Frequency [Hz]	t_{start} [s]	t_{end} [s]
1	0.25	16.17	88.17
2	0.5	96.68	132.7
3	0.8	138.8	162.5
4	1.1	167.7	183.6
5	1.4	188.2	200.8
6	1.7	205.6	215.6
7	2.0	220	228.6
8	2.5	232.5	239.6
9	3.0	243.5	249.2
10	3.5	253	257.9

Table 4.2: Table showing the ten different frequencies used to extract the ADs.

As the model is moved in harmonic motion both the position and velocity are changing with time and the corresponding forces are logged. Knowing the forces corresponding to every point of position and velocity one may set up a system of equations and solve using the least square method, this is how aerodynamic derivatives are found. Details about the calculations are explained in section 2.9.

All the results from the load cells includes noise which has to be filtered away to get the desired accuracy. The method used to filter the signal is a butterworth lowpass infinite impulse response filter. The filtering is done in MATLAB with the designfilt and filtfilt functions. Figure 4.8 below shows the raw and filtered signal. The filtering section of the script was provided by the supervisor.

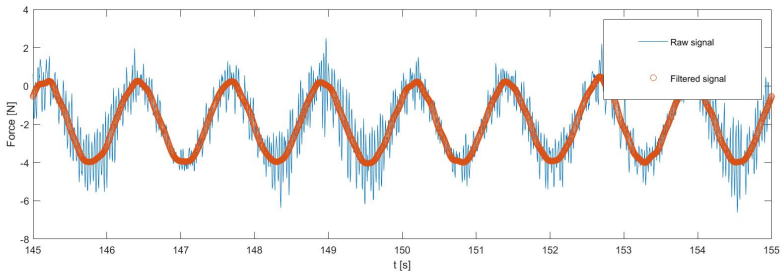

Figure 4.8: Plot of a raw signal and an IIR-filtered signal.

Chapter 5

Results and Discussion

Having collected results from the wind tunnel the important part of presenting and discussing the results still remain. When doing experimental work there are many things playing a role to how the results appear and the results have to be presented and interpreted. In the following sections results are presented topic by topic then discussion is made around the results and finally potential sources of error are examined in the end. In all the results the current model properties are used, B = 0,054m, D = 0,74m and L = 2,68m.

5.1 Vortex Shedding Identification

The results from the vortex shedding tests were used to identify wind velocities where the model didn't exhibit too much vortex shedding vibrations. When measuring other quantites like static coefficients and ADs vortex shedding vibrations is a source of unwanted noise. Figure 5.1 shows at which wind speeds the model was subject to vortex shedding vibrations.

Using 6,9 m/s as the wind speed causing vortex shedding vibrations, the section height 0,054 m as characteristic length and recorded shedding frequency of 31,7 Hz the Strouhal number of the section becomes $St = \frac{f_s D}{V} = 0,25$.

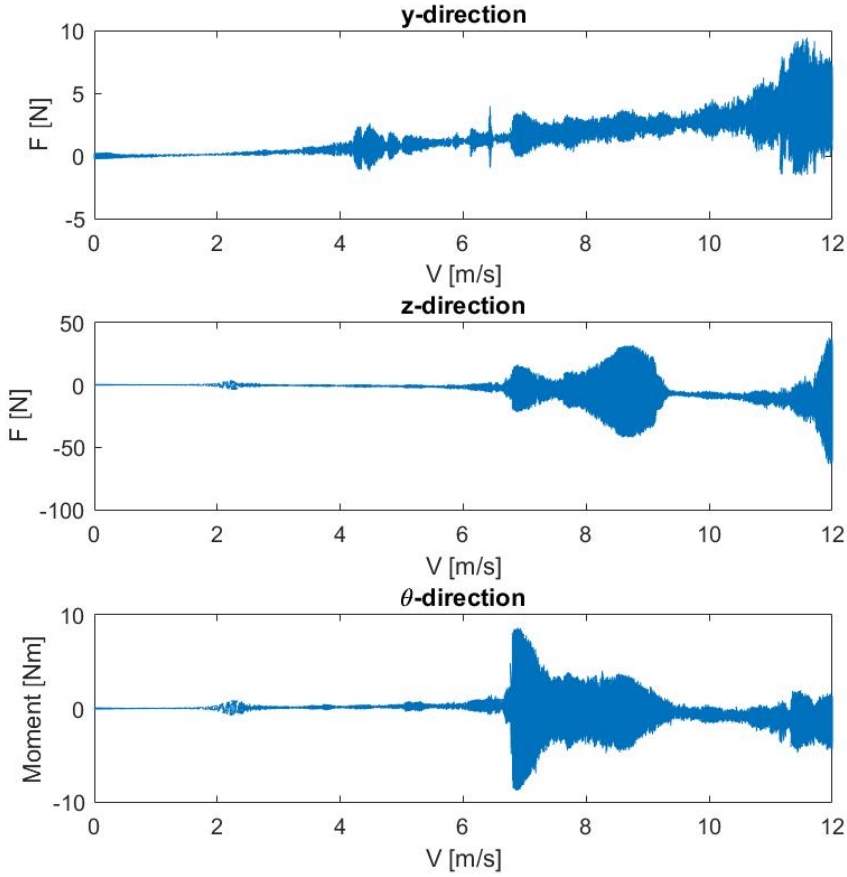

Figure 5.1: Results of a vortex shedding test.

By figure 5.1 the minimum forces obtained on the cross section in the three directions is when the wind velocity is 6 m/s and 10 m/s. Further testing was conducted with these velocities to avoid large vortex shedding forces, noise and in the end get the most accurate results. This way the forces from vortex shedding is minimised and neglected in the following results.

Having seen a lot of vortex shedding vibrations it is pointed out that the Scruton number of the model is lower than in a real bridge. The Scruton number for the model calculated with a 0,65 percent damping and using the bounding box around the cross section as characteristic area is Sc = 0,51. The damping of 0,65 percent is an estimate derived using the phone application VibSensor and the bounding box around the cross section is 54 mm x 740 mm. Real bridges typically have a Scruton number of approximately ten.

The magnitude of the vortex shedding vibrations is heavily dependent on coinciding with a resonant frequency of the model, so it is pointed out that to avoid noise the model should have been even stiffer and lighter.

The power spectral density of a vortex shedding test is shown below in figure 5.2. It must be pointed out that the test was not conducted with a steady increase in wind speed, and therefore the time can not be linearly related to wind speed and the spectrum may not show correctly how bad vortex shedding is relatively between frequencies.

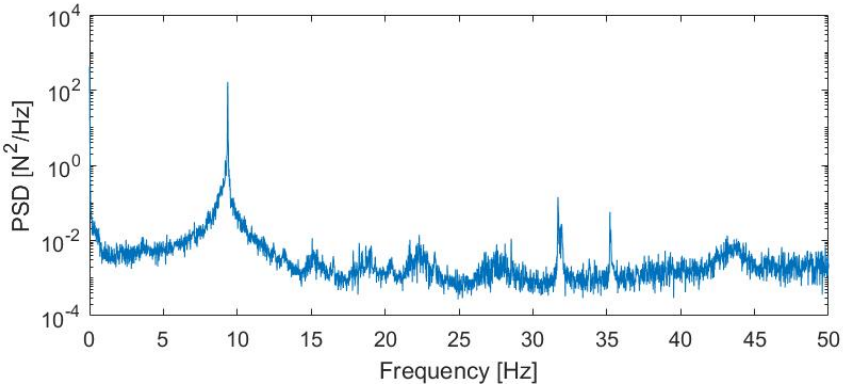

Figure 5.2: PSD of a vortex shedding test.

Even if the spectrum is taken from a test with unsteady increase in wind speed we may find eigenfrequencies of the model by peak picking. The three most distinguished peaks are at 9.35 Hz, 31.7 Hz and 35.2 Hz, this is not too far away from estimations shown in table 3.3 and table 3.4. The first peak in figure 5.2 is nice and broad which may indicate there have not been what is called lock-in to a certain vortex shedding frequency when resonance occured. However the two smaller peaks are much sharper and this may indicate the vortex shedding locked in on the resonant frequency and stayed there until it broke away completely due to the wind speed changing to much and then the shedding frequency was so far away from the resonant frequency the spectre just goes almost flat.

5.2 Static Load Coefficients

The static load coefficients are calculated as described in section 2.8. They are in figure 5.3 to 5.5 functions of the angle α, this gives the static load coefficients as continuous functions of the angle. α is the the angle between the cross section and the wind flow. Figures of the static coefficients for the reversed model is placed in the Appendix.

Testing was done at three different wind velocities: 6, 8 and 10 m/s. All three coefficients has the same shape and almost the same values for all the three velocities, which may

indicate low Reynolds dependency. The grey line in the figures indicates the measured coefficients and the circles are the average of the measurement at the respective angle. In figure 5.5 there is some vibrations at approximately 2°, this may have slightly affected the results.

Something to remember is that this test is a test of a simple model of the bridge girder. Railings, cables and optionally spoilers may heavily affect the static coefficients, but the results from the girder looks promising. It is important to have a C_M close to zero for α = 0, this to prevent the girder from rotating when the wind blows.

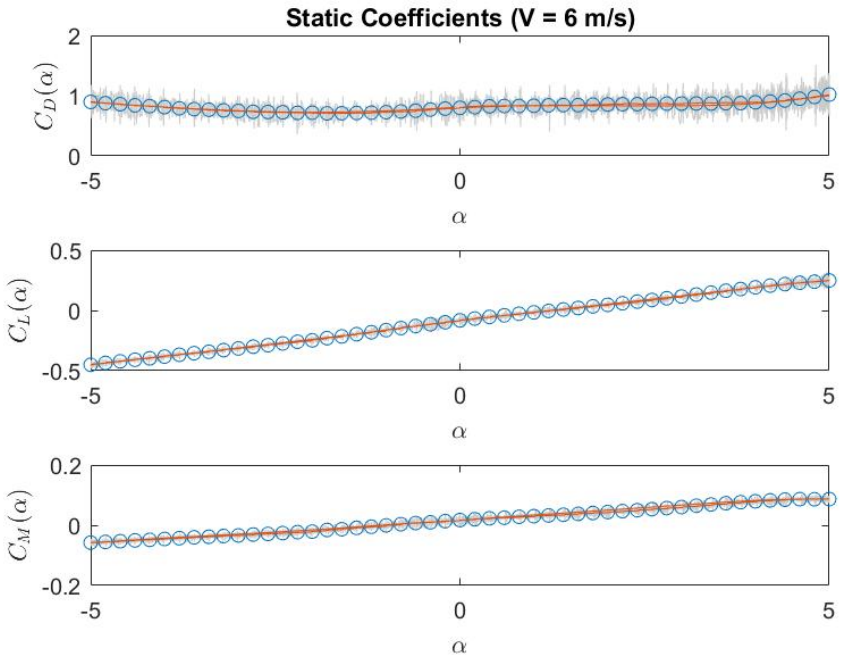

Figure 5.3: Static load coefficients found at wind speed 6 m/s.

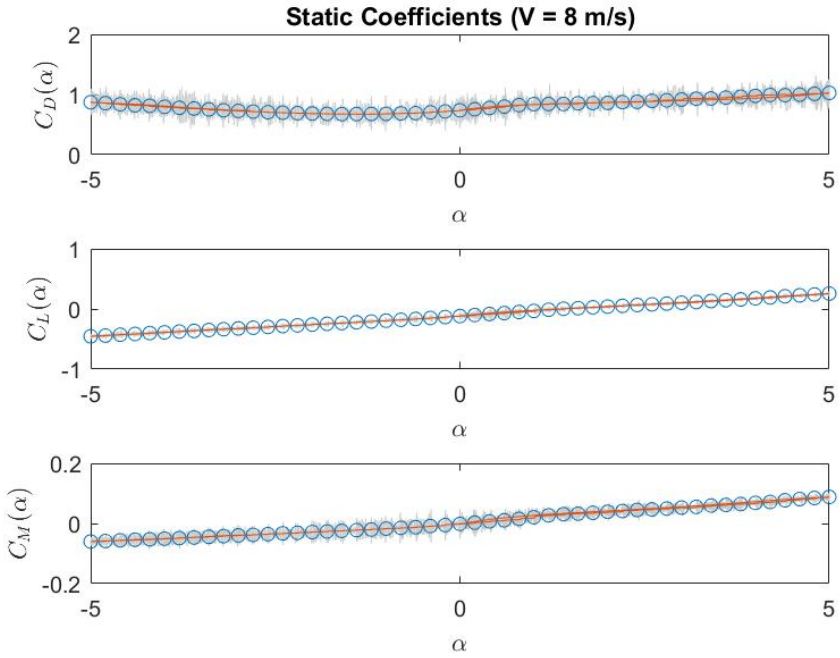

Figure 5.4: Static load coefficients found at wind speed 8 m/s.

It can be seen from figure 5.3 to figure 5.5 the wind speed used to find the static coefficients does not change the coefficients much, which means the assumptions commonly used for static coefficients appear to be reasonable for this case.

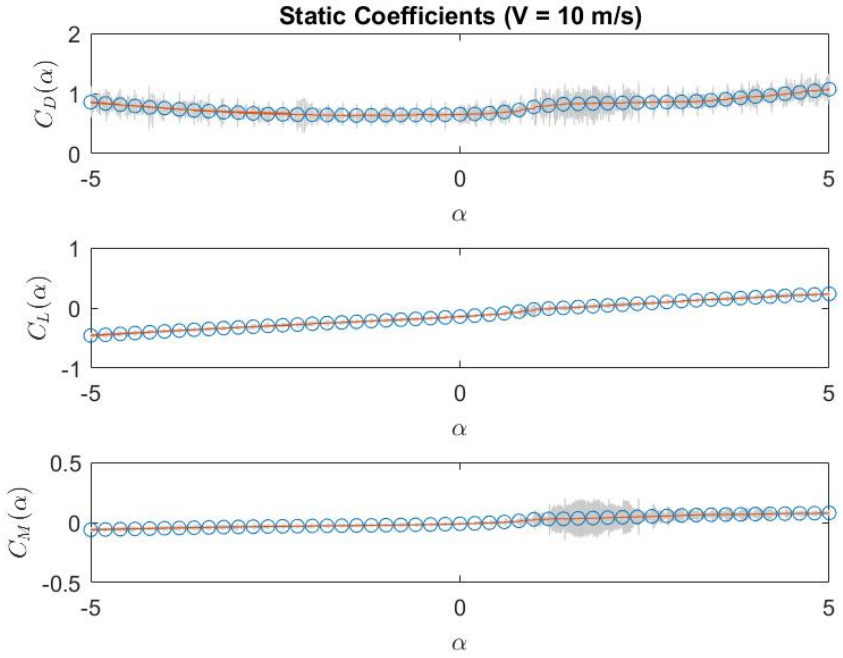

Figure 5.5: Static load coefficients found at wind speed 10 m/s.

As seen from figure 5.3 to figure 5.5 the drag coefficient for the section is around 1. The drag coefficient is rather high because the characteristic length is taken as the height of the section model. The height of the twin deck section model is not descriptive for the surface that may be hit by air because the second girder also has a surface up against the flow and this makes the drag higher. Also the twin deck section model is quite deep relative to how high it is so drag forces from shear becomes significant even if the body is bluff.

The observed non-linearity of the drag coefficients are evidence of how complicated the flow patterns around the section are, how changes are unpredictable and how the forces are affected by it.

From figure 5.6 the static coefficients dependence on wind speed and therefore Reynolds number can be seen clearly. The Reynolds dependency is clearly present but not very large. For the lift coefficient the Reynolds dependency seems to be almost non-existent. The tendency is that the static coefficients gets smaller values for higher wind velocities.

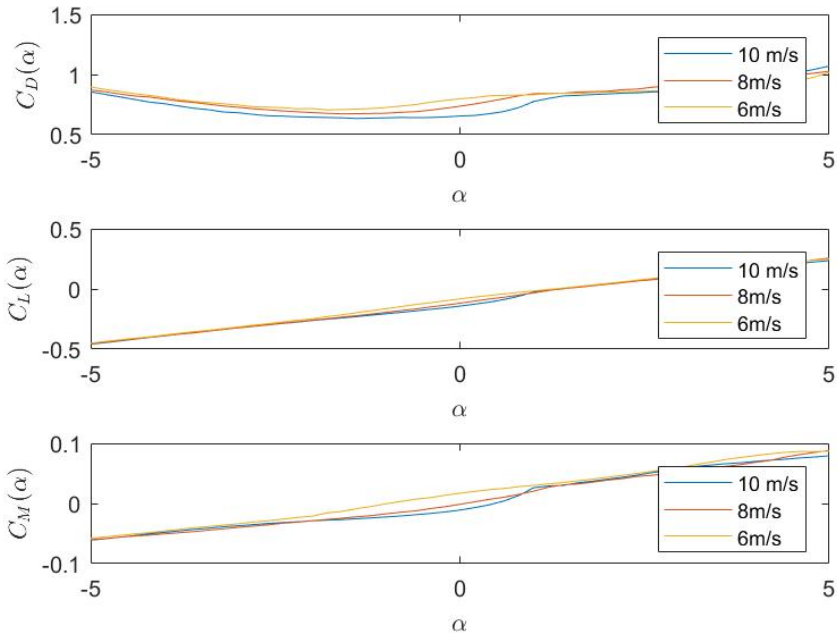

Figure 5.6: Comparison of the static coefficients found with different wind velocities.

5.3 Self Excited Forces

The dynamic forces found in figure 5.7 to 5.9 is due to the motion patterns shown in figure 4.7. The self excited forces are grouped into D_{SE}, L_{SE} and M_{SE}. Given the assumption that the self excited forces depend linearly on the displacements and the velocities the self excited forces should be shaped as a harmonic function.

In figures 5.7 to 5.9 phase lag as seen in equation 2.17, between the displacements and forces is clearly visible as the peak values do not come at the same time.

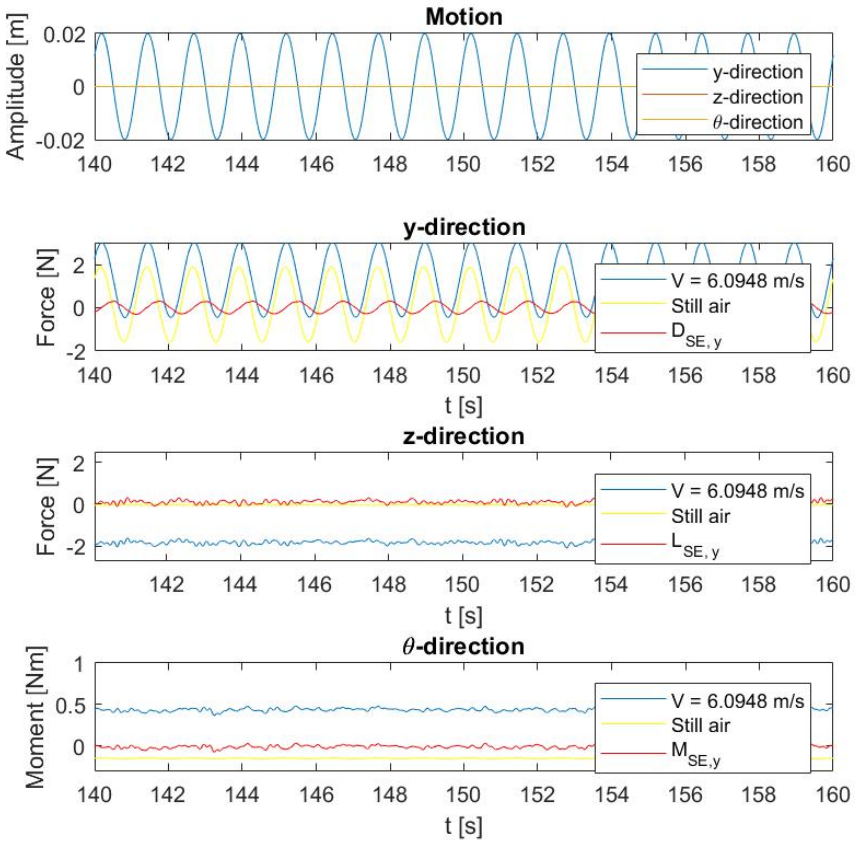

Figure 5.7: Self exited forces from testing carried out with horizontal motion.

The plots in figure 5.7 to 5.9 shows the dynamic forces from three different test series, the figures show the forces from t = 140 s to t = 160 s where the motion frequency is 0.8 Hz. The wind speed was 6.0871 m/s. The reduced velocity becomes:

$$V_r = \frac{V}{\omega B} = \frac{V}{2\pi f B} = 1.6364 \tag{5.1}$$

Figure 5.7 shows dynamic forces from horizontal motion in all three directions. The most dominating force is in the horizontal direction, the shape is also nearly harmonic. The self excited forces in the two other directions is small and does not fit very good to a harmonic shape. In the two directions where forces are small the derived ADs are expected to be low. These ADs are A_5^*, A_6^*, H_5^* and H_6^*.

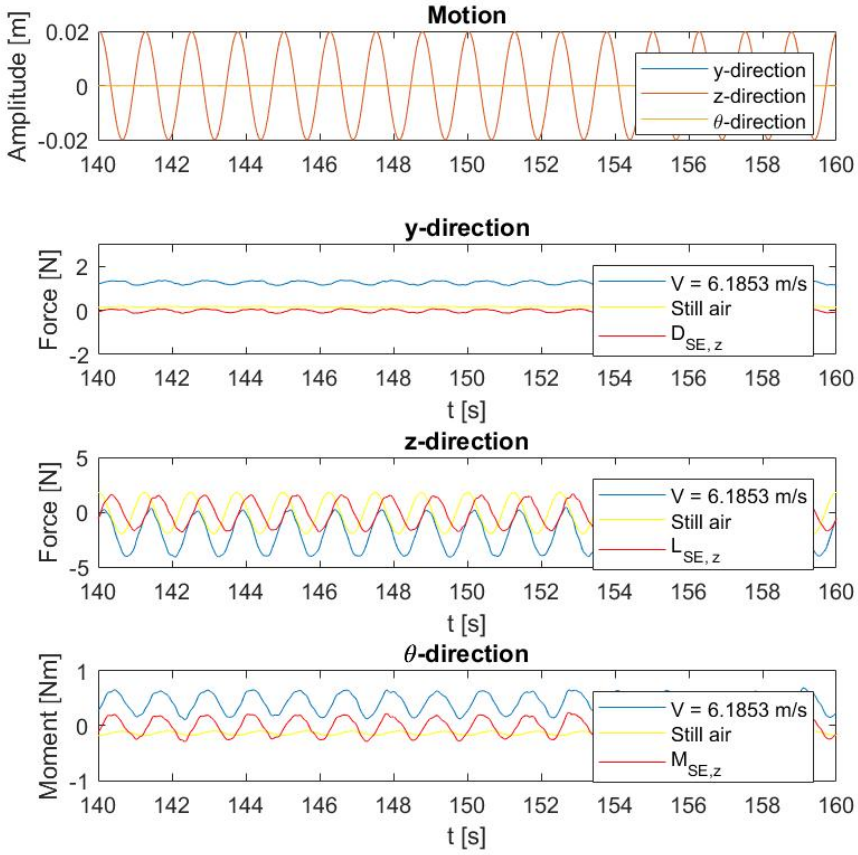

Figure 5.8: Self exited forces from testing carried out with vertical motion.

From figure 5.8 dynamic forces from vertical motion is shown in all three directions. The red line in the three latter plots display the self excited forces. In all three directions the red line is almost following a harmonic shape, but with some deviation. The self excited forces D_{SE}, L_{SE} and M_{SE} have little deviation from harmonic shape, which shows the self excited forces linear dependence on displacements and velocities with the coefficients P_5^*, P_6^*, H_1^*, H_4^*, A_1^* and A_4^* are a good approximation. The forces corresponding to D_{SE} are low, so P_5^* and P_6^* will have low values.

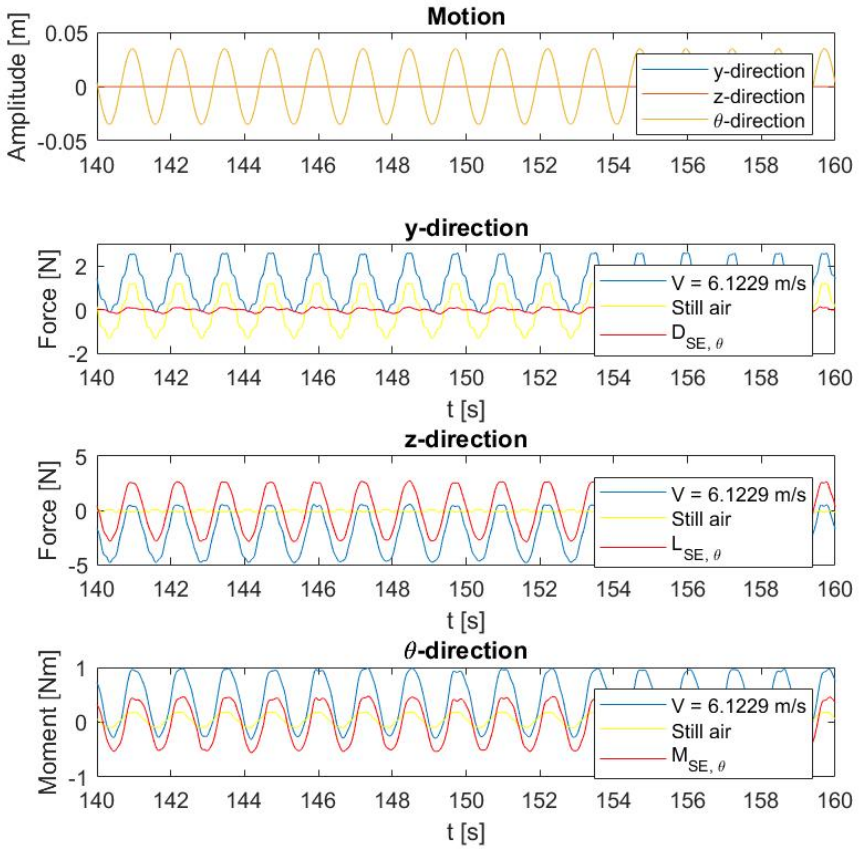

Figure 5.9: Self exited forces from testing carried out with angular motion.

Figure 5.9 shows dynamic forces from angular motion in all three directions. In all directions the self excited forces are harmonically shaped. The horizontal forces is deviating a bit more than the others, but the magnitude is low and the corresponding ADs will be low. It can be pointed out the corresponding ADs P_2^* and P_3^* are usually not important. The magnitude of the self excited forces in the vertical and torsional direction are significant and therefore the corresponding ADs are expected to have significant values, also these are important ADs for torsional instability and flutter.

5.3.1 Aerodynamic Derivatives

The results of the aerodynamic derivatives testing is presented below. They are extracted as described in section ”2.9 Identification of Aerodynamic Derivatives”, and presented in dimensionless form as in equations 2.35 and 2.36. There are 20 points in each plot, they come from two different wind velocities and ten different frequencies which gives 20 different sampling points. The samples are presented as functions of the reduced velocity. The blue lines in figure 5.10 to 5.12 are second order polynomials to estimate the ADs for any reduced velocity. ADs for the reversed model is placed in the Appendix.

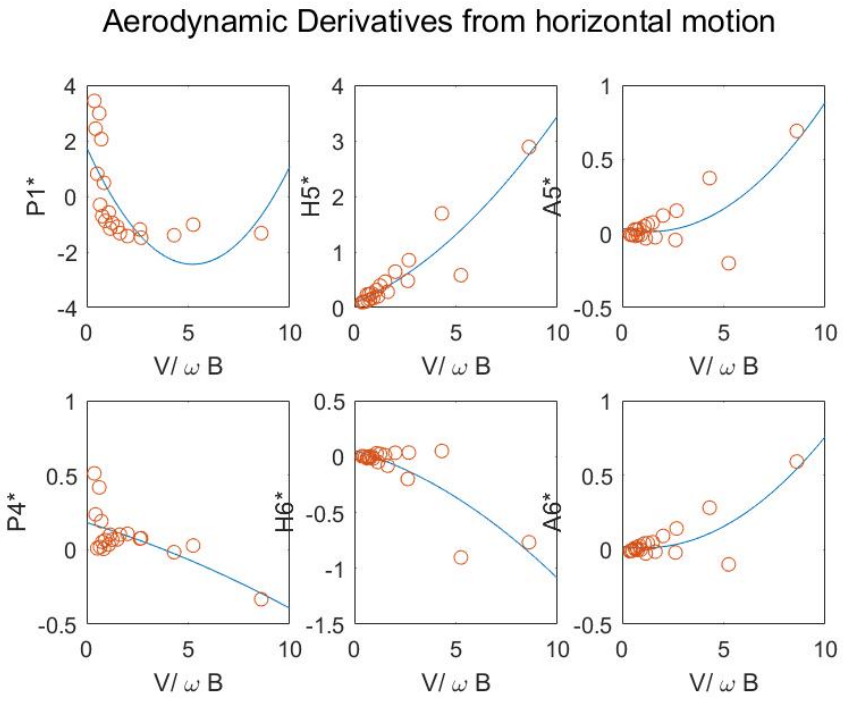

Figure 5.10: Aerodynamic derivatives from horizontal motion.

It can clearly be seen from figure 5.10 to 5.12 that the aerodynamic derivatives change a lot with regards to reduced velocity. Some ADs are nice and linear while others are highly non-linear, for some ADs sampling points seem to diverge strongly as reduced velocity increases. We observe ADs both positive and negative and some are both, depending on reduced velocity.

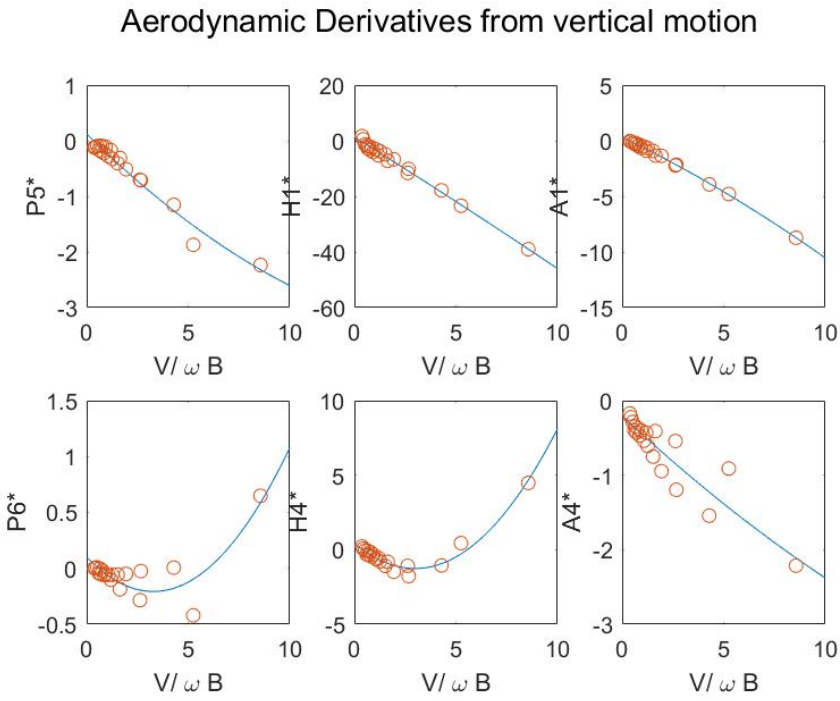

Figure 5.11: Aerodynamic derivatives from vertical motion.

The aerodynamic derivative A_3^* is important for static divergence as there can not be complete instability characterised by the determinant of the impedance matrix going to zero unless this AD is positive. It can be seen from figure 5.12 that A_3^* is clearly positive and the positivity increase with increasing reduced velocity. Having a positive A_3^* is a bad result for the cross section.

The aerodynamic derivative A_2^* is important for instability in torsion as there can not be complete instability characterised by the determinant of the impedance matrix going to zero unless this AD is positive. It can be seen from figure 5.12 that A_2^* is clearly negative and the negativity increase with increasing reduced velocity. Having a negative A_2^* is a good result for the cross section.

The aerodynamic derivative H_1^* is important for vertical instability called galloping as there can not be complete instability characterised by the determinant of the impedance matrix going to zero unless this AD is positive. It can be seen from figure 5.11 that H_1^* is clearly negative and the negativity increase with increasing reduced velocity. Having a negative H_1^* is a good result for the cross section.

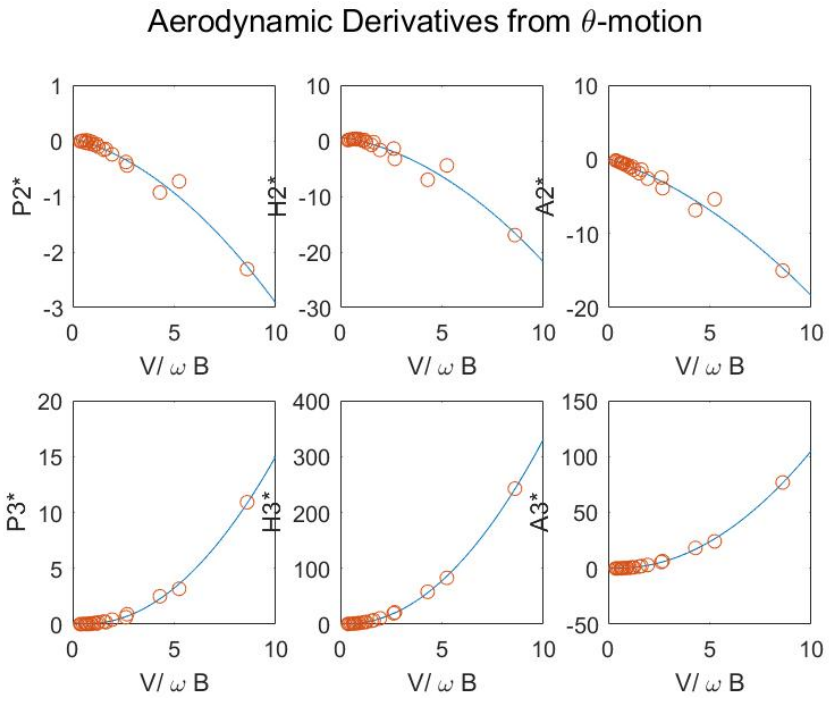

Figure 5.12: Aerodynamic derivatives from angular motion.

Here follows an attempt to shed light on the ADs effect on flutter and whether the gathered results are good or bad. The aerodynamic derivatives H_1^*, A_1^*, H_2^*, A_2^*, H_4^*, A_4^*, H_3^* and A_3^* are important for flutter instability as it is the interaction between these ADs that for bi-modal flutter in the vertical and torsional direction cause the determinant of the impedance matrix to go to zero. When it comes to the damping related ADs H_1^* and A_2^* it is bad if they are positive. From the plots in figure 5.10 to 5.12 we see H_1^* and A_2^* are clearly negative which is good with regards to limiting the consequences of flutter. When it comes to the stiffness related ADs H_4^*, A_4^*, H_3^*, A_3^* and the coupled aerodynamic damping related ADs A_1^* and H_2^* it is harder to say what is good and what is bad because it depends on the eigenfrequencies of the bridge and the coupling of the modes. If we assume the vertical mode has a lower eigenfrequency than the torsional mode it would be good with a positive H_4^* to decrease the total stiffness of the vertical mode bringing the vertical eigenfrequency further away from the torsional eigenfrequency. The same way around it would be good with a negative A_3^* to increase the total stiffness of the torsional mode bringing the torsional eigenfrequency further away from the vertical eigenfrequency. It is even more complicated with the coupled aerodynamic stiffness terms A_4^*, H_3^* and the coupled aerodynamic damping terms A_1^*, H_2^* as both negative and positive values can be bad depending on the coupling of the modes. In the following the setup in figure 2.11 with wind from the left side is taken for granted. Assuming the deck behaves a bit like a typical airfoil and the coupled flutter mode consists of positive rotational displacement while the

vertical velocity is positive and the vertical displacement is positive while the rotational velocity is negative, all with regards to the coordinate system shown in figure 2.11, we may say a bit more about the ADs. For the given case it follows that the phase angle between angular displacement and vertical displacement is ninety degrees. In the case assumed, which is a realistic case, the bad case for the ADs would be stiffness bringing the eigenfrequencies closer and damping aligning damping forces and velocity so energy is added(negative aerodynamic damping) instead of extracted. For the case described table 5.1 sums up the four coupled ADs.

AD	**From matrix**	**Effect in assumed case**	**Should be**	**Really is**	**Larger V_r makes it**
A_4^*	Stiffness	Damping	Positive	Negative	Worse
H_3^*	Stiffness	Damping	Negative	Positive	Worse
A_1^*	Damping	Stiffness	Negative	Negative	Better
H_2^*	Damping	Stiffness	Negative	Negative	Better

Table 5.1: Coupled flutter ADs.

The reason the crossed aerodynamic stiffness terms act as damping and the crossed aerodynamic damping terms act as stiffness for the given case is that the phase angle between the angular displacement and vertical displacement is ninety degrees. The reason stiffness usually have the effect of stiffness and damping usually have the effect of damping is because the effect of stiffness is achieved if forces are aligned with displacement and the effect of damping is achieved if forces are aligned with velocity. For the given case the velocity related forces from one mode align with the displacement of the other mode due to the ninety degree phase angle between modal displacements and the ninety degree phase angle between stiffness forces and damping forces. The same way displacement related forces from one mode align with the velocity of the other mode.

Having cleared that out table 5.1 looks the way it looks because:

- A_4^* should be positive to damp the torsional mode.
- H_3^* should be negative to damp vertical mode.
- A_1^* should be negative to speed up the torsional mode bringing the eigenfrequency further away from the vertical eigenfrequency.
- H_2^* should be negative to slow down the vertical mode bringing the eigenfrequency further away from the torsional eigenfrequency.

The reason a solution has to be found iteratively would be because for example the effect of one AD may change the frequency of a mode, which changes the self excited forces generated from that mode which changes something else again. Simply explained it seems like there are multiple positive and negative feedback loops that may affect each other. Visualising these phenomenons requires a good understanding of Argand diagrams. In this world some models are too good to be true while some are too true to be good, it is suspected that this explanation of flutter belong in the latter category.

As it can be seen from figure 5.10 to figure 5.12 the last sampling point is incredibly important for the curve fitting for some aerodynamic derivatives. Adding the fact that sampling points in some plots seem to be strongly diverging it is believed for example the addition of one more sampling point would drastically change the fitted polynomial. This raises strong doubt with regard to the legitimacy of the ADs as functions of reduced velocity when reduced velocity is relatively large.

5.3.2 Comparison of the Self Excited Forces and Forces from the ADs

To investigate the validity of the assumption that the self excited forces depend linearly on the displacements and the velocities the forces obtained in testing is plotted against the forces obtained when equation 2.31 is used. The ADs are the ones found in section 5.3.1, and they are multiplied by motion components from the motion patterns in figure 4.7. These plots are for the same reduced velocity as in equation 5.1.

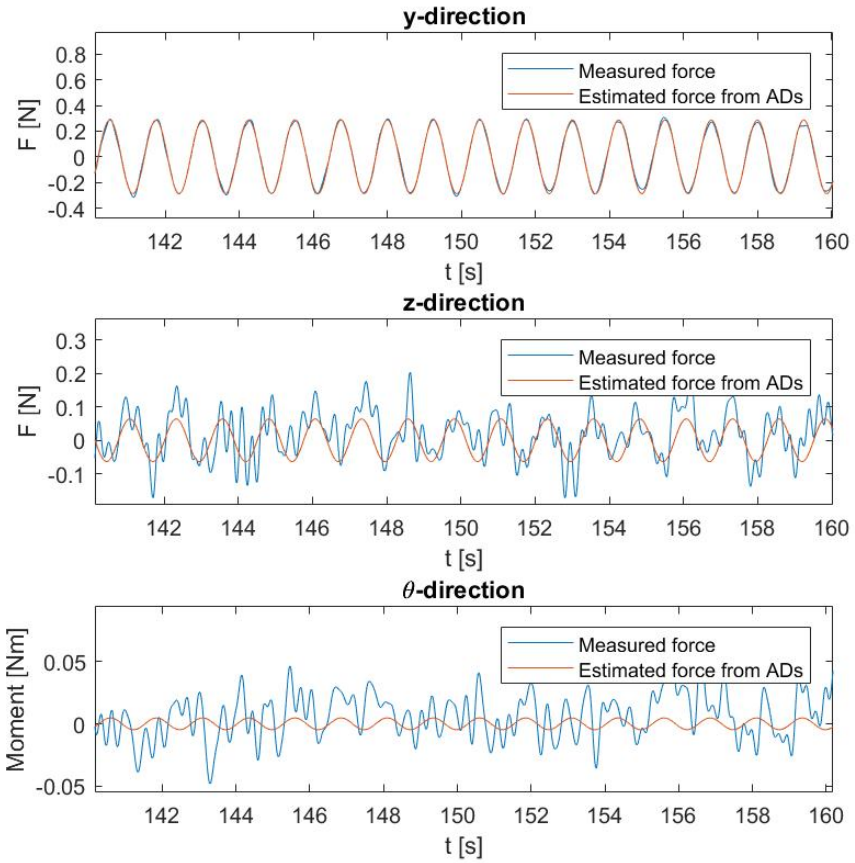

Figure 5.13: Comparison to assess linear dependence of self excited forces from horizontal motion.

From figure 5.13 the self excited forces from the horizontal motion is compared with self excited forces estimated using the ADs. The forces in z-, and θ-direction is very low and doesn't fit very well. The reason could be noise from measurements, because these forces are very low, but it could also be due to non-linearity. Forces in the y-direction fit well which indicate the assumption of self excited forces being linearly dependent on

displacement and velocity being a reasonable assumption for the relevant ADs, but clearly not ADs extracted in the vertical and angular directions.

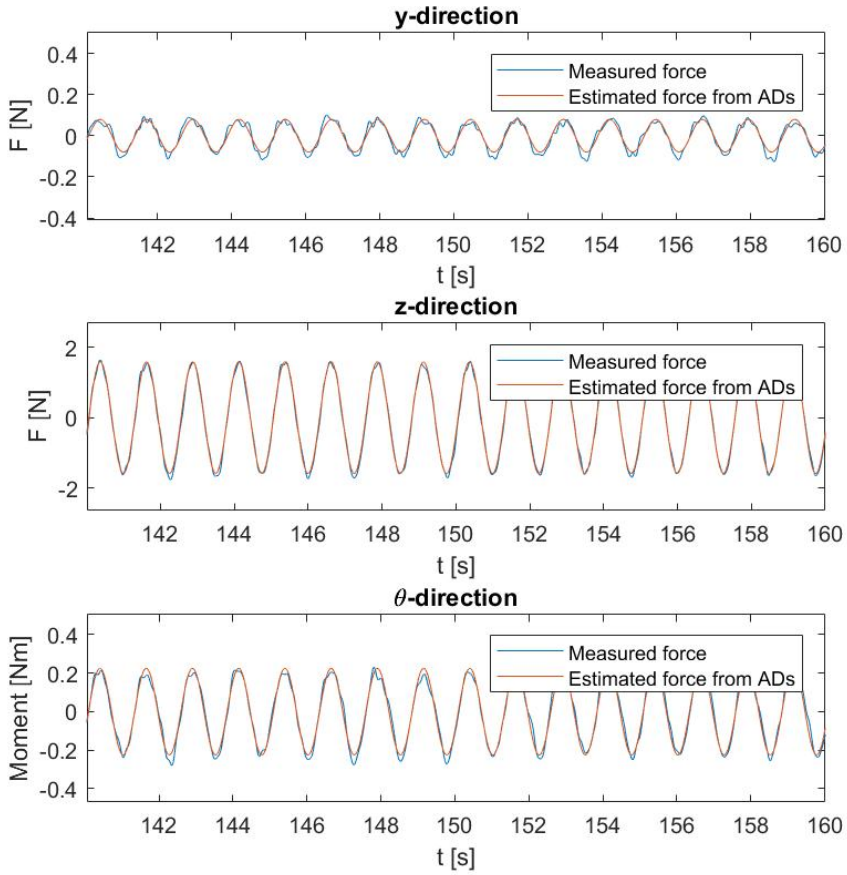

Figure 5.14: Comparison to assess linear dependence of self excited forces from vertical motion.

From figure 5.14 it looks like the forces approximated by the ADs fit the measured forces well, there are some mismatch especially for the peak values in the y- and θ-direction, which indicates some non-linearity.

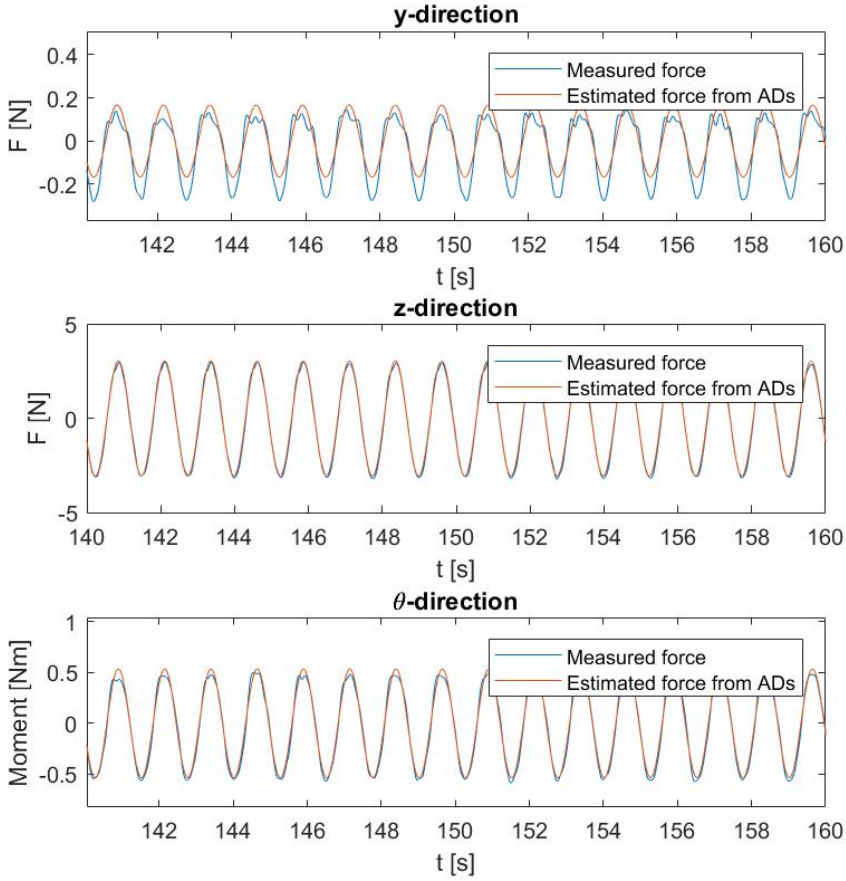

Figure 5.15: Comparison to assess linear dependence of self excited forces from angular motion.

Figure 5.15 shows large self excited forces in z-direction. These forces are obtained from torsional motion, see figure 4.7. The calculated forces from the ADs also fit quite well in the z-direction, there is just a little mismatch. Forces in θ-direction also fit well. It looks like the estimated forces in horizontal direction gets a bit to high values.

5.3.3 Self Excited Forces Estimated from Random Motion

There are some assumptions that need to be considered when estimating self excited forces from random motion. The superposition principle needs to be valid for the aerodynamic forces. But also the linearity of the AD theory as mentioned earlier must hold.

Figure 5.16 to 5.19 shows estimated and measured SE-forces. The motion consist of mul-

tiple frequency components from 0-3.5 Hz. The method used to estimate the forces is a time domain method that uses rational function approximation of the ADs to extract the SE forces. The theory is explained in (Siedziako and Øiseth, 2018b). The square of the correlation coefficient (R^2) is used to show the accuracy of the estimated forces with respect to the measured forces.

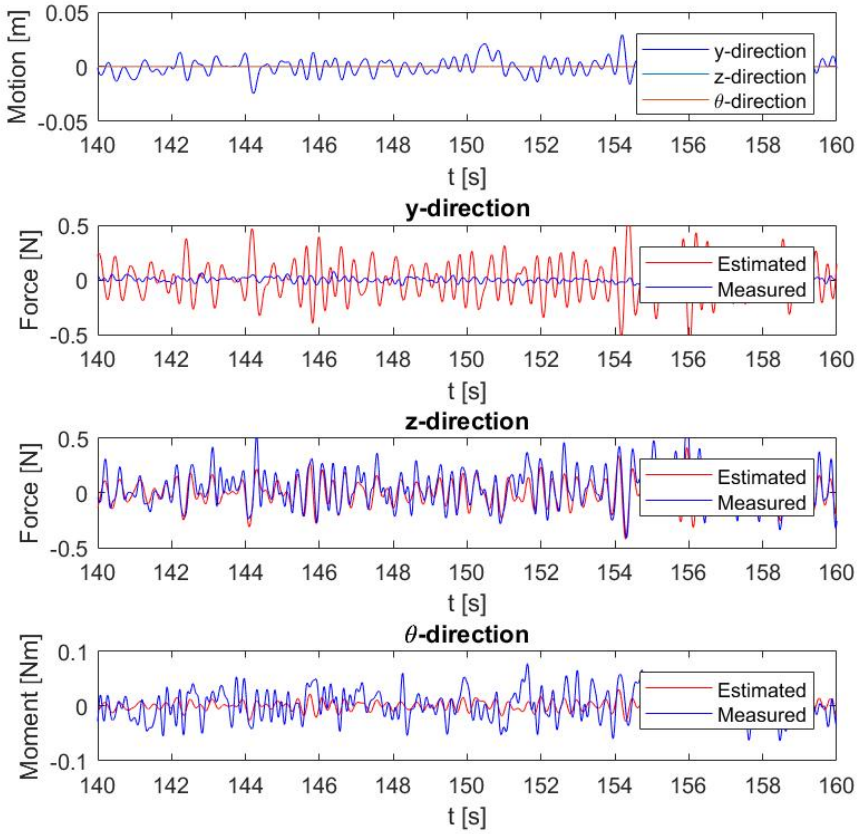

Figure 5.16: Estimated self excited forces compared with measured self excited forces from horizontal random motion and wind speed 10 m/s.

It looks like the SE forces in the horizontal direction are strongly non-linear, as shown by figure 5.16 and table 5.2, where the R^2 values are very low for horizontal motion, this indicates low correlation between the estimated and measured forces. It can be seen from table 5.2 the tendency for non-linearity and invalid superposition is present also in the vertical and angular direction.

When the motion is applied in the vertical and angular direction the results are quite good, with R^2 values of approximately 85-95% except for low correlation for horizontal forces with random motion in all directions. This indicate that the accuracy of the superposition principle approximation is appropriate concerning bridge design in lack of better theory and that the linearity of the SE forces with regard to velocity and displacement can be used.

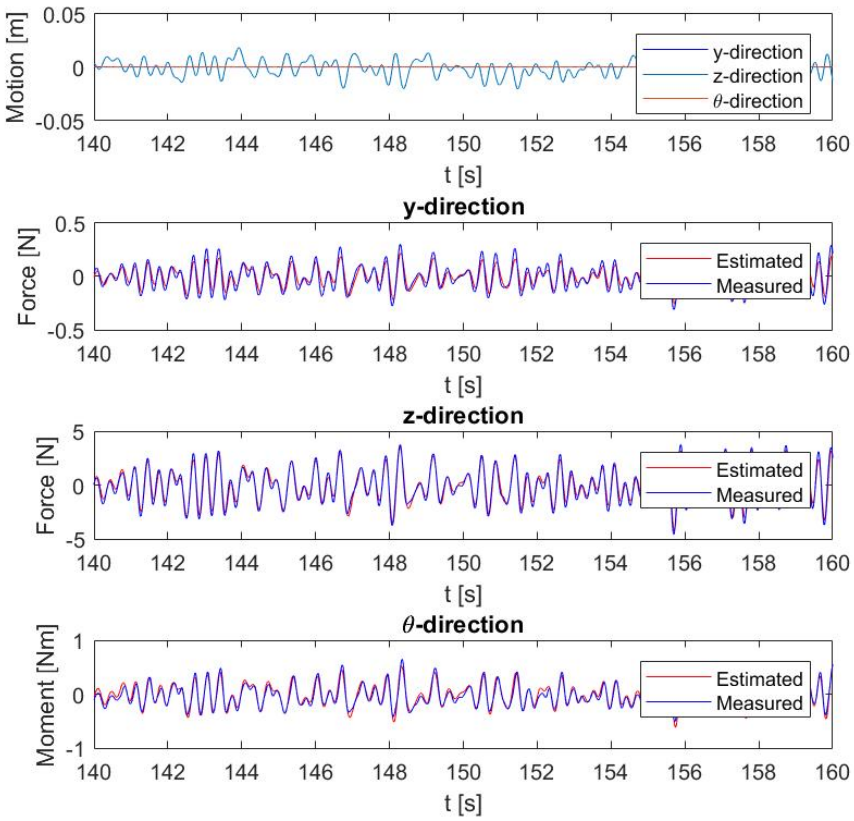

Figure 5.17: Estimated self excited forces compared with measured self excited forces from vertical random motion and wind speed 10 m/s.

The random motion seen in figure 5.16 to 5.19 is made up from lots of different frequencies with different and varying amplitudes which means there are multiple AD values being applied at the same time. If superposition is valid for the forces the presence of multiple frequencies and different AD values being used at once will be handled well under the assumptions in the load model. If the superposition principle is not valid forces will not

be correctly approximated with the prescribed motion.

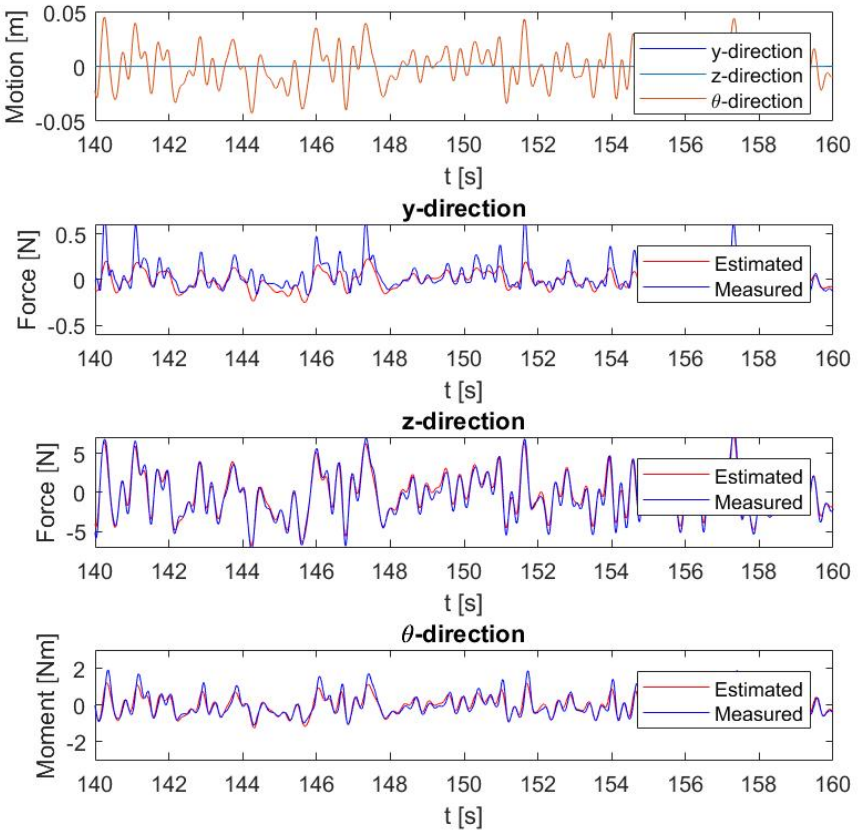

Figure 5.18: Estimated self excited forces compared with measured self excited forces from angular random motion and wind speed 10 m/s.

Looking at figure 5.16 to 5.19 and table 5.2 it can be seen that approximated SE forces are correlating better to the measured forces where measured forces are relatively large. This observation is promising with regards to design because large forces are relevant forces. It is also promising that the estimation in vertical and angular direction fit so well, because these directions is the critical directions in flutter analysis, which means the flutter calculations can be accurate.

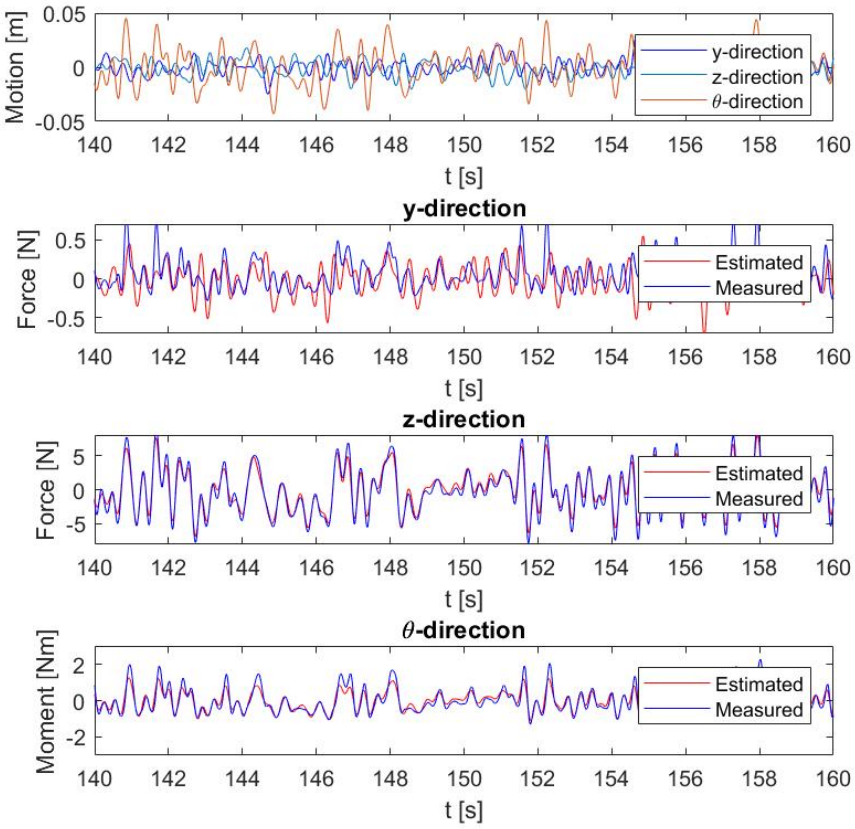

Figure 5.19: Estimated self excited forces compared with measured self excited forces from random motion in all directions and wind speed 10 m/s.

Table 5.2 sums up the most interesting results from figure 5.16 to 5.19.

	y-motion	**z-motion**	**θ-motion**	**All directions**
Forces in y-direction	0.0018	0.8639	0.5369	0.19
Forces in z-direction	0.6042	0.9563	0.9631	0.9553
Forces in θ-direction	0.1413	0.9087	0.8447	0.8605

Table 5.2: R^2-values from figures 5.16 to 5.19.

5.3.4 Critical Flutter Wind Speed

Given the aerodynamic derivatives found in section 5.3.1 the following critical flutter wind speed was found: $V_{cr} = 67,23$ m/s

The critical wind speed was calculated for the Sulafjorden bridge with a 2800 m span, 343,0 m tower height measured from the bridge deck and 37,0 m cable spacing. The reduced velocity used to extract the ADs was V_r = 2,34(Giske and Aasrum, 2018).

5.4 Methods to Reduce Vortex Shedding Vibrations

In the wind tunnel there was tested countermeasures to limit vortex shedding vibrations. In figure 5.20 and figure 5.21 plots are shown of forces with and without countermeasures for vortex shedding vibration.

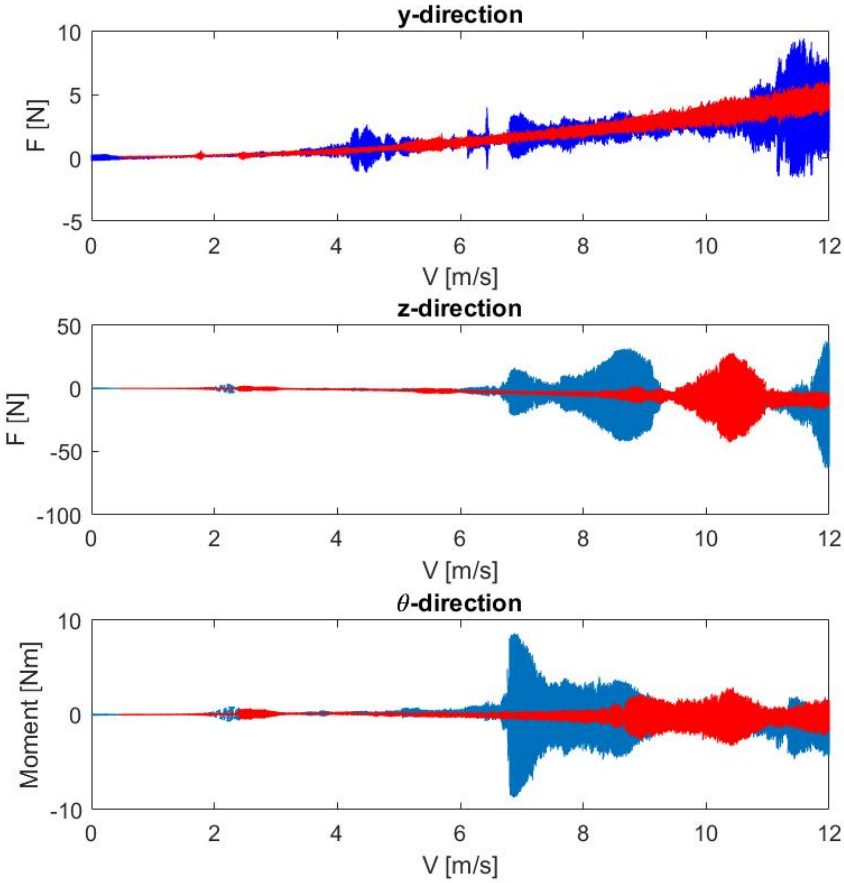

Figure 5.20: Comparison between the default model and the model with a spoiler and TMDs subjected to vortex shedding tests.

As seen from figure 5.20 the countermeasure of one spoiler and a TMD seems to decrease vibrations in the y-direction and the θ-direction while it changes the Strouhal number for the z-direction causing the same resonant frequency to be hit in the same way but for a higher wind speed. The applied TMDs were simply sticks with 20 coins on them, the eigenfrequencies could be adjusted by changing the eccentricity of the coins. The TMDs where adjusted to have the same eigenfrequency as the first eigfrequency of the lanes. There is a possibility the delayed vortex shedding vibrations in z-direction is coming from the second eigenfrequency.

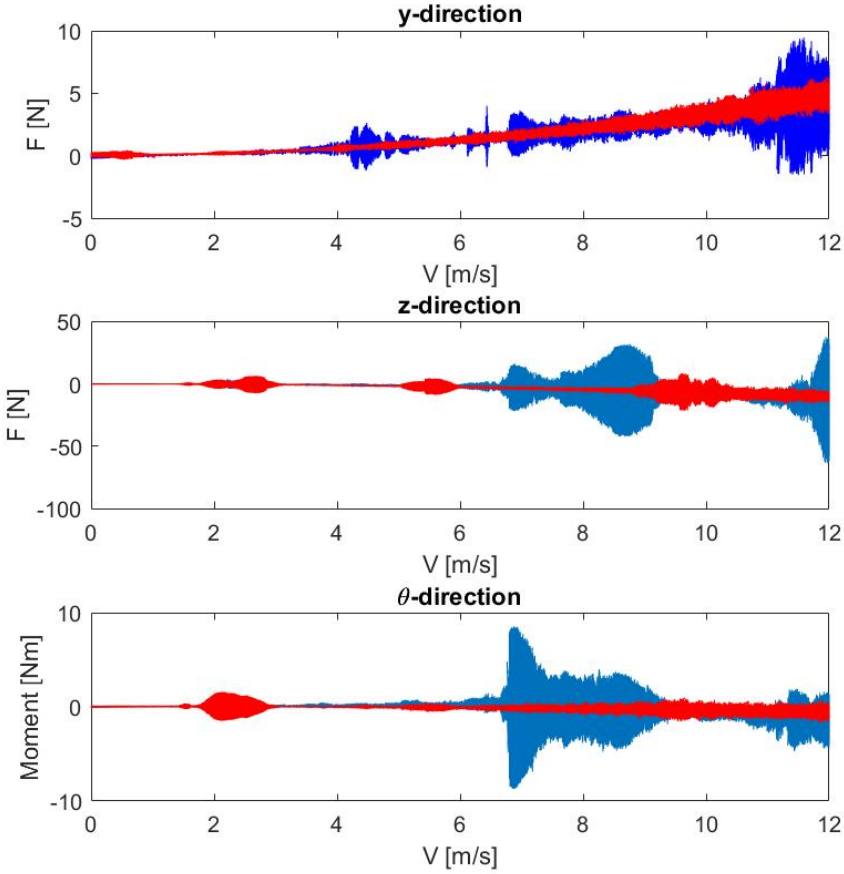

Figure 5.21: Comparison between the default model and the model with two sets of spoilers subjected to vortex shedding tests.

As seen from figure 5.21 the countermeasure of two spoilers seems to decrease vibrations in all directions. In this case using two spoilers seem to be the most effective way of dealing with vortex shedding.

5.5 Investigation of Damping

From figure 5.22 it can be seen the peak of the resonant frequency around eight hertz has been split in two smaller peaks by the TMD which is exactly what is expected. The height of the peaks around eight hertz in the spectral density also show vibrations were radically diminished by the TMD.

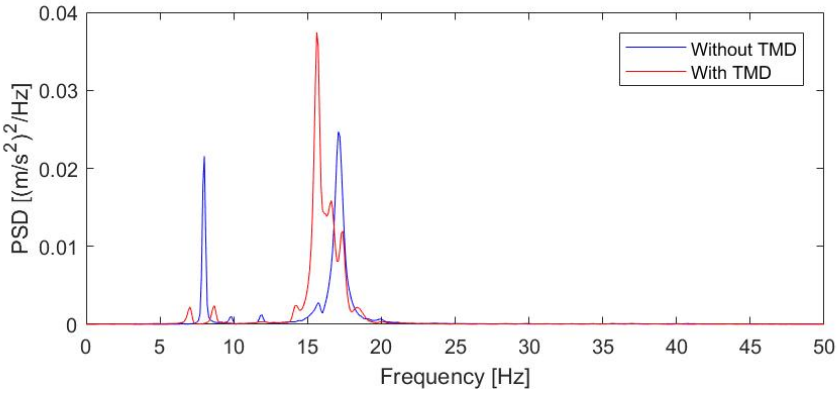

Figure 5.22: Comparison of the PSD between the back lane with and without TMD, carried out with data from the app VibSensor.

Figure 5.23 shows how free vibrations are damped when TMDs are not applied. The forces are obtained by simply hitting the middle of the lane once and measure how the forces decrease. From these tests it is possible to calculate damping ratios by use of theory explained in section 2.16. Knowing the two girders have close eigenfrequencies may explain the varying amplitude of the vibrations as it looks like a phenomenon called beating. Beating happens because two close modes are vibrating with slightly different frequencies so one moment they cancel each other out while a bit later they stack on top of each other.

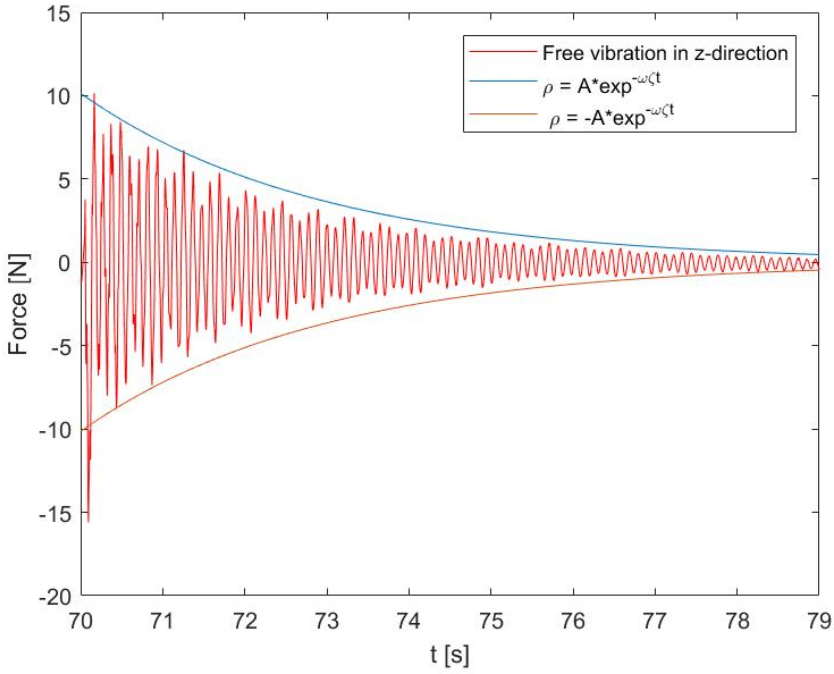

Figure 5.23: Visualisation of free vibration with plot of the damping line.

From calculations of the free vibrations in figure 5.23 following is calculated:
ζ = 0.0044
ω = 9.18 Hz
A = 14.4173 N
These values are extracted from measurements obtained in the wind tunnel, so there could have been interactions between the two lanes affecting the results.

Figure 5.24 shows how free vibrations are damped when TMDs are applied.

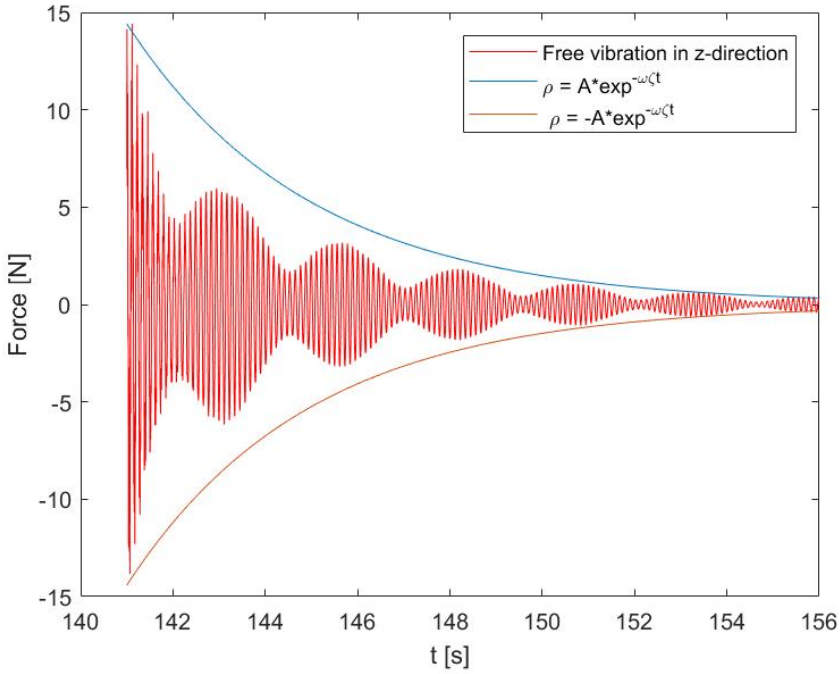

Figure 5.24: Visualisation of free vibration using a TMD with plot of the damping line.

From calculations of the free vibrations in figure 5.24 following is calculated:
ζ = 0.0065
ω = 9.18 Hz
A = 10.1392 N
These values are extracted from measurements obtained in the wind tunnel, so there could have been interactions between the two lanes affecting the results.
The TMDs increase the damping ratio by a factor of almost 1,5.

5.6 Discussion

5.6.1 Reynolds Dependency

When testing the model in the wind tunnel at low wind speeds the Reynolds number is not the same as it will be for the full scale bridge at higher wind speeds. As flow characteristics are in reality dependent on Reynolds number contrary to what we like to assume when experimenting the forces are changed by changing Reynolds number. According to Schewe and Larsen the drag coefficient obtained from low speed wind tunnel testing and used in the bridge design appear conservative(Schewe and Larsen, 1998). It is the authors

somewhat unqualified interpretation that the flow is subcritical during testing and closer to being transcritical for the full scale bridge which results in smaller drag forces for the latter. This is also shown in the results, where the static coefficients decrease with increasing wind speeds. It has also been shown by Matsuda et al. that flutter wind speeds calculated with ADs extracted at high Reynolds numbers are the same or higher than flutter wind speeds calculated using ADs extracted at lower Reynolds numbers(Matsuda et al., 2001) like in a conventional wind tunnel as done in this thesis. Short and concise this means wind tunnel testing at low Reynolds numbers is believed to be conservative.

5.6.2 Vortex Shedding

As shown in section 5.1 the model exhibited a lot of vortex shedding induced vibrations during wind tunnel testing. The slot size could be modified and it has been shown through multiple studies modifying the slot size may change the vortex shedding behaviour drastically and even completely alter it for the wind tunnel wind speeds. Also the appearance of the severity of the vortex shedding is largely depending on coinciding with a resonant frequency which may be avoided by making a stiffer and lighter wind tunnel model. The Scruton number is very low for the wind tunnel model and this is known to emphasise the effects of vortex shedding. For a real bridge the Scruton number is much higher than for the wind tunnel model.

5.6.3 Effect of Asymmetry and Effect of Shear Centre

Asymmetry of the cross section cause mass centre not to be in the middle. For a real bridge uneven distribution of mass over the width may encourage the use of two different cable cross sections for economical purposes as the cables will be loaded differently. For very long span bridges the cables are the main source of torsional stiffness. If cables are not of equal size to compensate for mass centre not being in the middle the cable shear centre will move towards the heaviest cable and change the aerodynamic behaviour of the bridge, maybe cancelling the potentially positive effect of the asymmetry. The position of the shear centre is important for the ae-stiffness as it determines what point the cross section rotates around when subjected to wind, and therefore the eccentricity to the force resultant making the aerodynamic moment. A solution could be to use two equal cables with different pre-tensioning to achieve a levelled cross section and a cable shear centre in the middle of the cable spacing.

5.6.4 Blockage

With a 2 m high and 2,7 m wide wind tunnel(Siedziako and Øiseth, 2018a) the blockage ratio for the model becomes $\frac{S}{C} = 0,0269 = 2,69\%$. For blockage ratios less than 6% the effects of blockage are small. For blockage ratios in the range 6-16% blockage is considered to be significant. However in reality this phenomenon does not follow a dichotomy where there is either no effect or there are pronounced effects. In reality it is strongly

believed the effect of blockage is continuously increasing with blockage ratio so there are small but negligible effects even at the ratio of 2,69%.

5.6.5 Angular Amplitude of Motion for Finding ADs

When testing for aerodynamic derivatives the rotational motion only had an angular amplitude of two degrees. Having tested with a maximum angle of two degrees the results may look deceivingly linear as non-linearities tend to be more present for large angles. It can be seen from the static coefficients pictured in section 5.2 that even the clearly non-linear coefficients are somewhat linear for angles between minus two and two degrees.

5.6.6 Self Excited Forces at High Frequencies

From an intuitive point of view the self excited forces should get higher and higher values as the motion frequency increase because using a fixed amplitude increased frequency means increased velocity. Despite what was expected figure 5.25 shows SE-forces for the vertical motion and it shows that the SE-forces increase up to 2 Hz, but then they drop before they increase again for the highest frequency, 3.5 Hz.

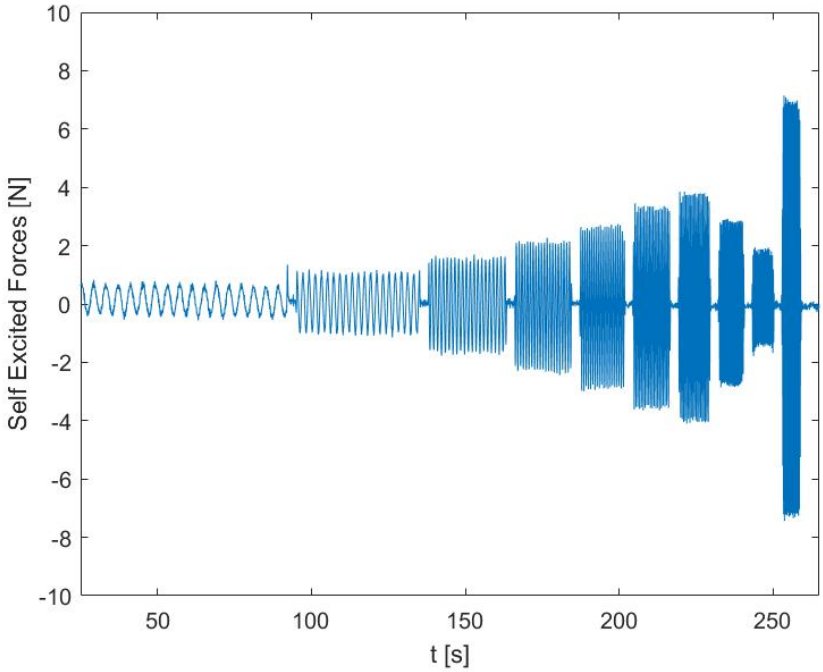

Figure 5.25: Visualisation of the self excited forces from vertical motion.

In figure 5.26 it can be seen that for low frequencies the total forces is mainly made up of SE-forces. But as the frequency increases the inertia forces gets larger and for the highest frequencies they are the main part. SE-forces are just approximately 10% of the total forces when the frequency is 3 Hz and wind velocity 6 m/s. In practice this means that for frequency around 3 Hz the SE-forces are extracted by subtracting something big from something big and the result is something small. This leads to the self excited forces, when making a small proportion of the total forces, is vulnerable to noise and filtering of the total forces. This can be contributing to the drop of SE-forces in figure 5.25.

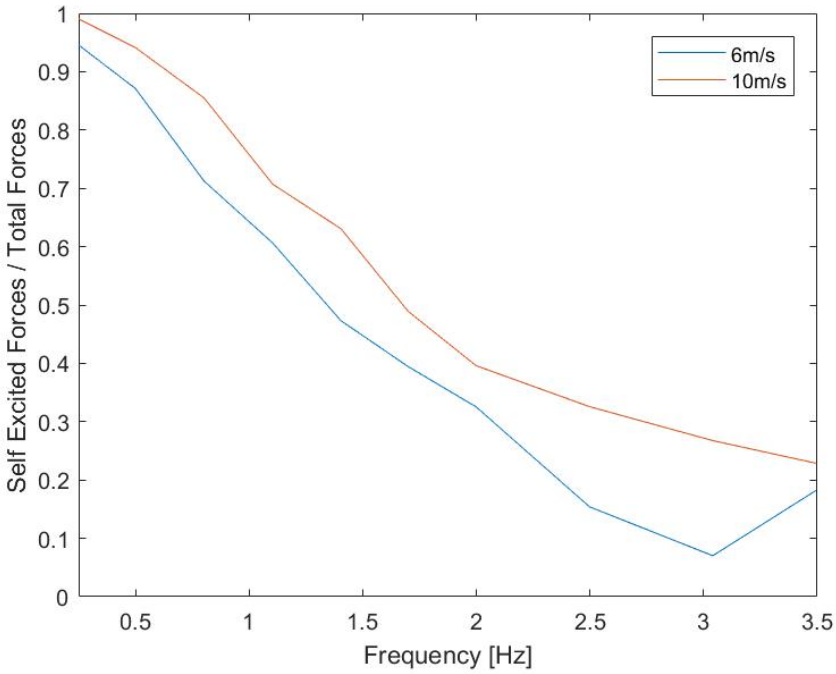

Figure 5.26: Visualisation of the propotion between SE-forces and total forces. Here total forces is the inertia forces and the SE-forces.

It can be seen from figure 5.10 to 5.12 that the ADs can be strongly non-linear with regard to reduced velocity, this could have explained the forces shown in figure 5.25. Because the amplitude is constant for all the frequencies tested the self excited forces due to displacement are not changing with changing frequency, this leaves us with changes caused by velocity. As amplitude is constant and frequency increase velocity also increase, this is changing the self excited forces. As the motion is vertical and the forces are vertical the relevant AD is H_1^* which is very linear, so it can not explain the forces seen in figure 5.25. The strange load pattern then have to be caused by error in the load cells or something else.

5.7 Potential Sources of Error

To assess the quality of the measurements and the aerodynamic derivatives it is important to have an idea of what might have affected the results. Throughout the making of this thesis there have been several potential sources of error. Naturally there may be sources of error not known to the authors but here follows a presentation of known sources.

- Testing at low Reynolds number.
- Vortex shedding disturbing flow patterns and measurements.
- Imperfections in foil application.
- Blockage not being accounted for in calculations.
- Testing for ADs done with small angular amplitudes.
- Assumption of SE forces depending linearly on displacement and velocity.
- Wind tunnel effects like boundary layer and end plates.
- Limited amount of tests and sampling points for making ADs as function of reduced velocity. As seen in section 5.3.1 the sampling point with the highest reduced velocity is extremely important for the curve fitting.
- Temperature changes in the wind tunnel during testing leading to all tests not being done with the same air density.
- The model was not perfectly shaped after carving and assembly.
- The parts of the model close to the end plates were cut and did not have the prescribed cross section.
- Splines used when CADing as the prescribed curvatures could not be made to work with a continuous gradient of the surface.
- There might have been unknown error in lab devices.
- There might have been unknown human error.
- The angle of the model after mounting it in the wind tunnel might not have been completely zero.
- Longitudinal directions of girders might not have been entirely parallel after build of final configuration.
- Minor scratches on model surface after assembly and transport.
- Carving leaves some surplus material and foil builds a bit, leading to a slight deviation from 1:50 scale not accounted for in calculations.

- In the y-direction where self excited forces are often small the measurements may be so sensitive they are vulnerable to external noise from for example construction work on campus, which was going on during testing.
- Uncertainty about the load cells range of validity. The motion frequency of 3,5 Hz is higher than anything ever tested for the setup before, which gives larger inertia forces than what is known to work for the load cells.

Of the mentioned considerations Reynolds number, imperfections in foil application, limited amount of tests and capacity of the load cells is believed to be the most significant potential sources of error.

Chapter 6

Conclusion

Having done model building, testing and discussion it is time to conclude. The conclusion will be split into two parts, one about the section model building and one about the test method and results.

6.1 Section Model Building

The chosen cross section proved to be interesting and possible to build given the available tools. Fusion 360 proved to be an easy to use and powerful program for turning ideas into reality. The milling process took a long time and could have been radically optimised with a more advanced router, but the X-Carve used was sufficient given the time frame. Assembly of the model went well, but it is strongly advised for future model building to carve the entire length at once and not 40 cm sections at a time. This to avoid imperfections in the joints. Foiling proved to be difficult because of the joints from the assembly, but the result was reasonably satisfactory. Eigenfrequencies of the model was measured and approximated analytically and the match between the two was reasonably good. Eigenfrequencies of the model was a bit low, but measurements could still be made under reasonable conditions because certain wind speeds caused little vortex shedding.

6.2 Test Method and Results

The experimental setup proved to be efficient to extract all the desired data and appeared flawless except of some uncertainty about the load cells capacity potentially making trouble for high frequencies giving large inertia forces. The conducted tests gave sufficient data to extract all the information necessary to analyse the cross section with regard to aerodynamic derivatives. The section showed lots of vortex shedding vibrations, but this is largely because of resonance and a low Scruton number, so the section may still be feasible for a real bridge despite the vortex shedding. The countermeasure for vortex shedding of one spoiler and TMD diminished the vortex shedding vibrations to some extent.

The countermeasure for vortex shedding of two spoilers proved very effective at alleviating vortex shedding vibrations. Static coefficients were found and seemed to be slightly Reynolds dependent, coefficients decreasing while wind speed increased. The aerodynamic derivatives were found and they were used to replicate self excited forces with the same motion history as used to extract them, this gave satisfying accuracy, showing the ADs were reasonably precise. There was some trouble dealing with a large proportion of inertia forces when the motion frequencies where high. For high frequencies strange results for the measured self excited forces were seen. It turned out the assumption of the self excited forces being linearly dependent on velocity and displacement could not be used in the horizontal direction, but can be used with good accuracy in the vertical and angular direction. This was verified by estimating the self excited forces with the calculated ADs using random motion which consisted of multiple frequency components from 0-3,5 Hz. The results showed high correlation between measured and estimated forces in the vertical and angular direction and low correlation in the horizontal direction. This implies that the superposition principle is applicable in the vertical and angular directions. It is pointed out self excited forces are often small in the horizontal direction. The superposition principle seemed to be reasonably valid for large forces, which is good for design applications. The cross section was shown to be resistant to galloping and torsional instability while being more vulnerable to static divergence and flutter.

Chapter 7

Future Work

Here comes some ideas for what can be done for future work. Both work making a whole new model and further investigation of the model considered in this thesis.

Suggestions to further work that can be done with regard to model building is:

- Increase the stiffness and reduce the weight of the model to increase the eigenfrequencies. The lighter H45 version of Divinycell could be used.
- Find methods to implement a TMD without affecting the aerodynamic behaviour of the cross section.
- Trying to optimise the production process by using better tools such as a router/CNC machine able to make the whole length in one piece and rotate the tool around more axes.

Suggestions to further work that can be done with regard to model investigation is:

- Find methods to reduce vortex shedding. Test at more realistic Scruton numbers. Further investigation of the effects of spoilers.
- Test section model with details, such as railings.
- Further investigation of the drop in SE-forces at high frequencies. See if load cells have sufficient capacity.
- Use obtained ADs to investigate all instability phenomenons, also for reversed setup.
- Try to find the reasons for the mismatch in analytically estimated eigenfrequencies and measured eigenfrequencies.
- Investigate Reynolds dependency of the model.
- Conduct testing which would give a better distribution of sampling points with regard to reduced velocity.

- Come up with a way of analytically estimate static coefficients and ADs.
- Test results for self excited forces as quadratic functions of displacement and velocity.
- Investigate what cross section characteristics affect which ADs.
- Find ADs with larger angular amplitude of motion to better reveal non-linearities.

Bibliography

Brancaleoni, F., 2016. Concepts and new perspectives for long span bridges. Romanian Journal of Transport Infrastructure 5 (1), 75–97.

Buresti, G., 1998. Vortex shedding from bluff bodies. Wind effects on buildings and structures, 61–95.

Caracoglia, L., Sarkar, P. P., Haan Jr, F. L., Sato, H., Murakoshi, J., 2009. Comparative and sensitivity study of flutter derivatives of selected bridge deck sections, part 2: Implications on the aerodynamic stability of long-span bridges. Engineering Structures 31 (9), 2194–2202.

Chopra, A. K., 2001. Structural dynamics: Theory and applications to earthquake engineering.

Constellationevolution, 2010. Image no. 241908. [Online; accessed 26-February-2018]. URL https://structurae.net/photos/241908-yangluo-bridge

Diab, 2018. Divinycell h. [Online; accessed 21-April-2018]. URL http://www.diabgroup.com/en-GB/Products-and-services/Core-Material/Divinycell-H

Diana, G., Fiammenghi, G., Belloli, M., Rocchi, D., 2013. Wind tunnel tests and numerical approach for long span bridges: the messina bridge. Journal of Wind Engineering and Industrial Aerodynamics 122, 38–49.

Diana, G., Rocchi, D., Belloli, M., 2015. Wind tunnel: a fundamental tool for long-span bridge design. Structure and Infrastructure Engineering 11 (4), 533–555.

Elger, D. F., Roberson, J. A., 2016. Engineering fluid mechanics. Wiley Hoboken (NJ).

Ge, Y.-J., Xiang, H.-F., 2008. Bluff body aerodynamics application in challenging bridge span length. In: BBAA VI International Colloquium on: Bluff Bodies Aerodynamics and Applications, Milano, Italy. Citeseer, pp. 20–24.

Gerb, 2018. Bridge tmd - millennium bridge, london / uk. [Online; accessed 11-May-2018].
URL http://www.gerb.in/index.php?id=589&no_cache=1&tx_photogals_elementid=1601&tx_photogals_image=4&MP=503-614

Giske, F., Aasrum, E. M., 2018. Optimising of super long span suspension bridge. Master's thesis, NTNU.

Horg, S. E., Aas, S. B., 2016. Wind tunnel testing of bridge decks. Master's thesis, NTNU.

Hui, M. C., Wong, C. K., 2009. Stonecutters bridge–durability, maintenance and safety considerations. Structure and Infrastructure Engineering 5 (3), 229–243.

Irwin, P. A., 2008. Bluff body aerodynamics in wind engineering. Journal of Wind Engineering and Industrial Aerodynamics 96 (6-7), 701–712.

Kardon, J. B., 2010. Tacoma narrows bridge collapse.

Kubo, Y., Miyazaki, M., Kato, K., 1989. Effects of end plates and blockage of structural members on drag forces. Journal of Wind Engineering and Industrial Aerodynamics 32 (3), 329–342.

Kwok, K. C., Qin, X. R., Fok, C., Hitchcock, P. A., 2012. Wind-induced pressures around a sectional twin-deck bridge model: Effects of gap-width on the aerodynamic forces and vortex shedding mechanisms. Journal of wind engineering and industrial aerodynamics 110, 50–61.

Larsen, A., Savage, M., Lafrenière, A., Hui, M. C., Larsen, S. V., 2008. Investigation of vortex response of a twin box bridge section at high and low reynolds numbers. Journal of Wind Engineering and Industrial Aerodynamics 96 (6-7), 934–944.

Lin, Y.-Y., Cheng, C.-M., Wu, J.-C., Lan, T.-L., Wu, K.-T., 2005. Effects of deck shape and oncoming turbulence on bridge aerodynamics. Ł 8 (1), 43–56.

Matsuda, K., Cooper, K., Tanaka, H., Tokushige, M., Iwasaki, T., 2001. An investigation of reynolds number effects on the steady and unsteady aerodynamic forces on a 1: 10 scale bridge deck section model. Journal of Wind Engineering and Industrial Aerodynamics 89 (7-8), 619–632.

Matsumoto, M., 1996. Aerodynamic damping of prisms. Journal of Wind Engineering and Industrial Aerodynamics 59 (2-3), 159–175.

Multiconsult, October 2015. Suspension bridge alternative - sulafjorden. Tech. rep.

Newland, D. E., 2012. An introduction to random vibrations, spectral & wavelet analysis. Courier Corporation.

Princeton, 2018. Drag of blunt bodies and streamlined bodies. [Online; accessed 10-April-2018].
URL https://www.princeton.edu/~asmits/Bicycle_web/blunt.html

Puckette, M., 2006. Low-pass and high-pass filters. [Online; accessed 30-December-2006].
URL http://msp.ucsd.edu/techniques/v0.11/book-html/node129.html

Ramsden, J., 2009. A critical analysis of the proposed bridge over the strait of messina. In: Proceedings of Bridge Engineering 2 Conference.

Sarkar, P. P., Caracoglia, L., Haan Jr, F. L., Sato, H., Murakoshi, J., 2009. Comparative and sensitivity study of flutter derivatives of selected bridge deck sections, part 1: Analysis of inter-laboratory experimental data. Engineering Structures 31 (1), 158–169.

Scanlan, R. H., Tomko, J., 1971. Air foil and bridge deck flutter derivatives. Journal of Soil Mechanics & Foundations Div.

Schewe, G., 2001. Reynolds-number effects in flow around more-or-less bluff bodies. Journal of Wind Engineering and Industrial Aerodynamics 89 (14-15), 1267–1289.

Schewe, G., Larsen, A., 1998. Reynolds number effects in the flow around a bluff bridge deck cross section. Journal of Wind Engineering and Industrial Aerodynamics 74, 829–838.

Scott, J., 2005. Drag of cylinders & cones. In: Aerospaceweb. org [online forum], URL: http://www. aerospaceweb. org/question/aerodynamics/q0231. shtml [cited 27 March 2010].

Siedziako, B., 2018. Modelling of the self-excited forces for bridge decks subjected to random motions: an experimental study.

Siedziako, B., Øiseth, O., 2018a. An enhanced identification procedure to determine the rational functions and aerodynamic derivatives of bridge decks. Journal of Wind Engineering and Industrial Aerodynamics 176, 131–142.

Siedziako, B., Øiseth, O., 2018b. Superposition principle in bridge aerodynamics: Modelling of self-excited forces for bridge decks in random vibrations.

Siedziako, B., Øiseth, O., Rønnquist, A., 2017. An enhanced forced vibration rig for wind tunnel testing of bridge deck section models in arbitrary motion. Journal of Wind Engineering and Industrial Aerodynamics 164, 152–163.

Strømmen, E., 2010. Theory of bridge aerodynamics. Springer Science & Business Media.

Takeda, K., Kato, M., 1992. Wind tunnel blockage effects on drag coefficient and wind-induced vibration. Journal of Wind Engineering and Industrial Aerodynamics 42 (1-3), 897–908.

Tamura, Y., Kareem, A., 2013. Advanced structural wind engineering. Springer Science & Business Media.

Virola, J., 2018. World's longest bridge spans. [Online; accessed 05-April-2018].
URL http://bridge.aalto.fi/en/longspan.html

West, G., Apelt, C., 1982. The effects of tunnel blockage and aspect ratio on the mean flow past a circular cylinder with reynolds numbers between 10 4 and 10 5. Journal of Fluid Mechanics 114, 361–377.

Wikipedia, 2018. List of longest suspension bridge spans — Wikipedia, the free encyclopedia. [Online; accessed 05-April-2018].
URL https://en.wikipedia.org/wiki/List_of_longest_suspension_bridge_spans

Yang, Y., Wu, T., Ge, Y., Kareem, A., 2014. Aerodynamic stabilization mechanism of a twin box girder with various slot widths. Journal of Bridge Engineering 20 (3), 04014067.

Zhang, Z., Zhang, X., Yang, Y., Ge, Y., 2017. Nonlinear aerodynamic and energy input properties of a twin-box girder bridge deck section. Journal of Fluids and Structures 74, 413–426.

Appendix A

The Frequency Response Function

$$M\ddot{r}(t) + C\dot{r}(t) + Kr(t) = q(t)$$

$$\ddot{r}(t) + \frac{C}{M}\dot{r}(t) + \frac{K}{M}r(t) = \frac{q(t)}{M}$$

Introducing $\omega_n = \sqrt{\frac{K}{M}}$ and $\zeta = \frac{C}{2M\omega_n}$.

$$\ddot{r}(t) + 2\omega_n\zeta\dot{r}(t) + \omega_n^2 r(t) = \frac{q(t)}{M}$$

Making the qualified assumption $r(t) = e^{i\omega t}$ and taking derivatives.

$$-\omega^2 r(t) + 2i\omega_n\omega\zeta r(t) + \omega_n^2 r(t) = \frac{q(t)}{M}$$

$$r(t)(1 - (\frac{\omega}{\omega_n})^2 + 2i\frac{\omega}{\omega_n}\zeta) = \frac{q(t)}{M\omega_n^2} = \frac{1}{M\frac{K}{M}}q(t) = \frac{1}{K}q(t)$$

$$r(t) = \frac{1}{(1 - (\frac{\omega}{\omega_n})^2 + 2i\frac{\omega}{\omega_n}\zeta)}\frac{1}{K}q(t) = H(\omega)\frac{1}{K}q(t)$$

$$H(\omega) = \frac{1}{(1 - (\frac{\omega}{\omega_n})^2 + 2i\frac{\omega}{\omega_n}\zeta)}$$

Introducing $\beta = \frac{\omega}{\omega_n}$ to obtain the typical expression for the FRF or dynamic amplification factor as it is also called.

$$H(\omega) = \frac{1}{(1 - \beta^2 + 2i\beta\zeta)}$$

Appendix B

Static Coefficients for Reversed Model

Static coefficients when the model is reversed so the wind blow from the other side.

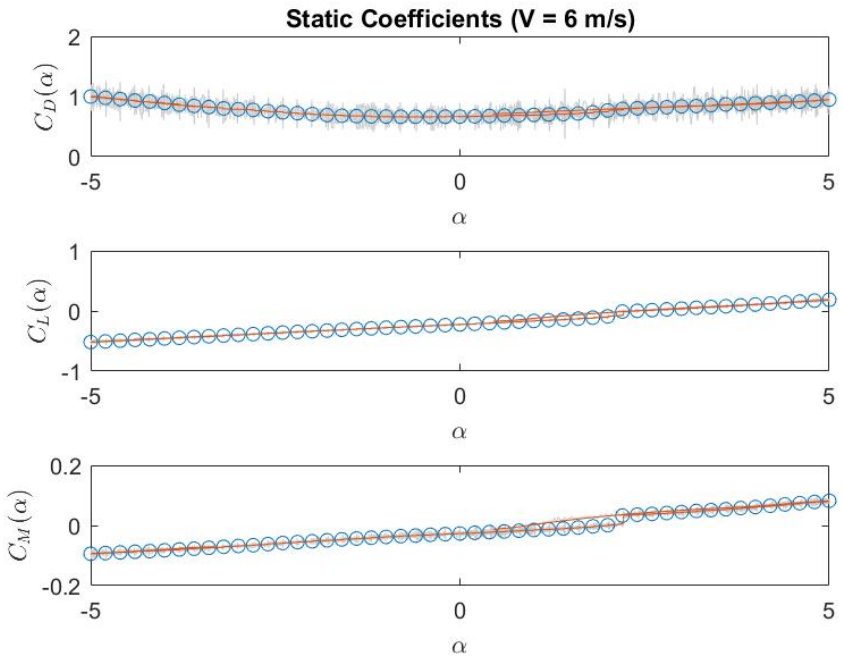

Figure B.1: Static coefficients measured with wind velocity 6 m/s.

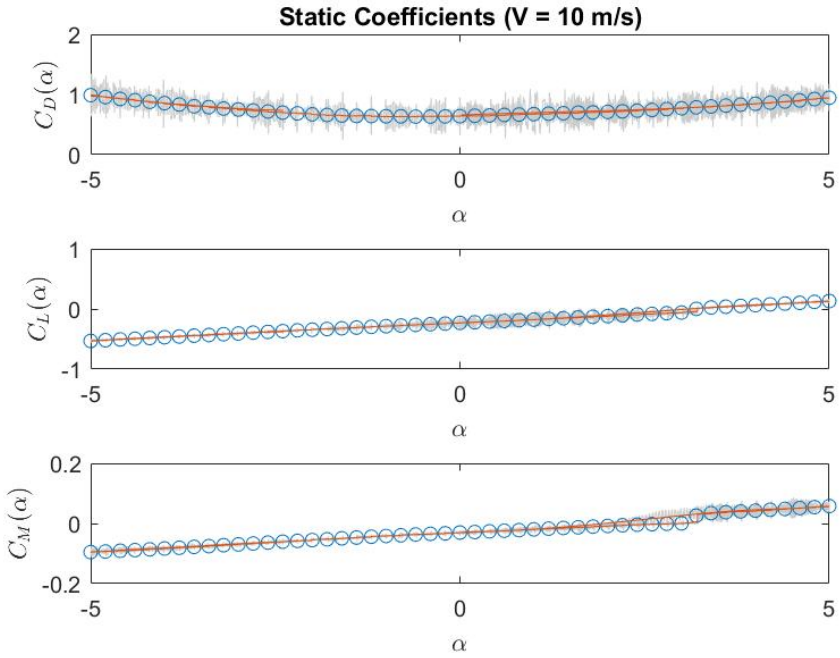

Figure B.2: Static coefficients measured with wind velocity 10 m/s.

Appendix C

Aerodynamic Derivatives for Reversed Model

Aerodynamic derivatives when the model is reversed so the wind blow from the other side.

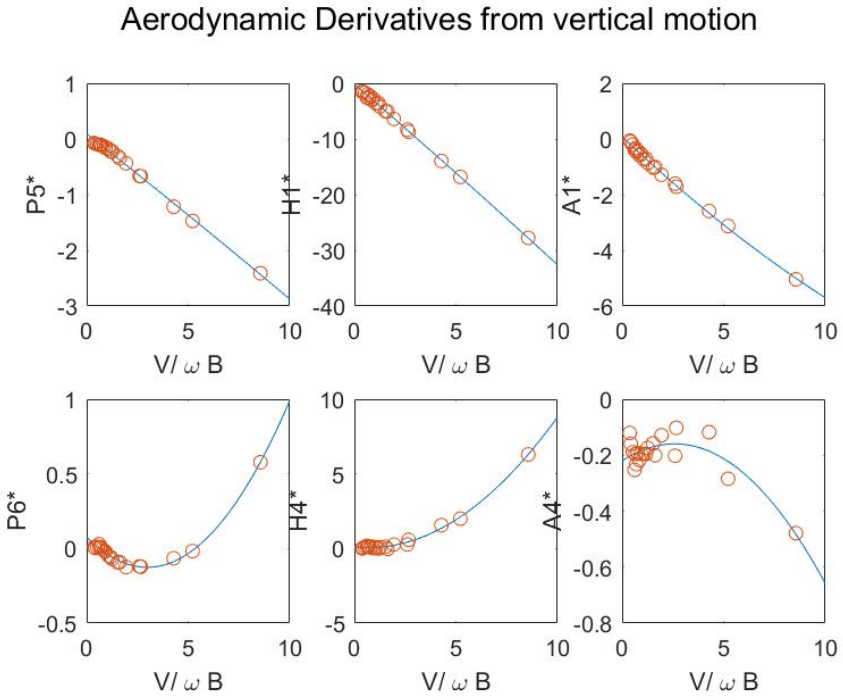

Figure C.1: Aerodynamic derivatives from vertical motion.

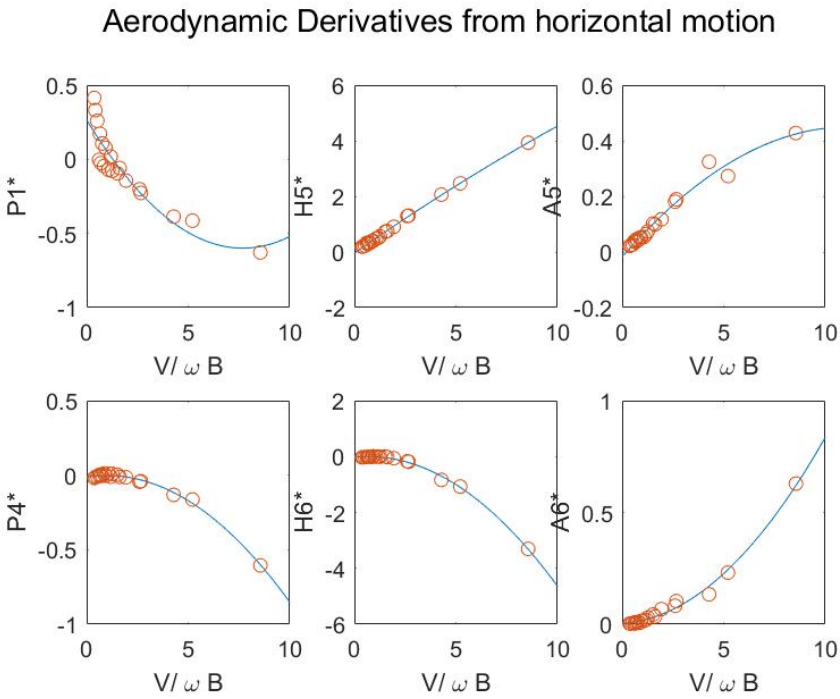

Figure C.2: Aerodynamic derivatives from horizontal motion.

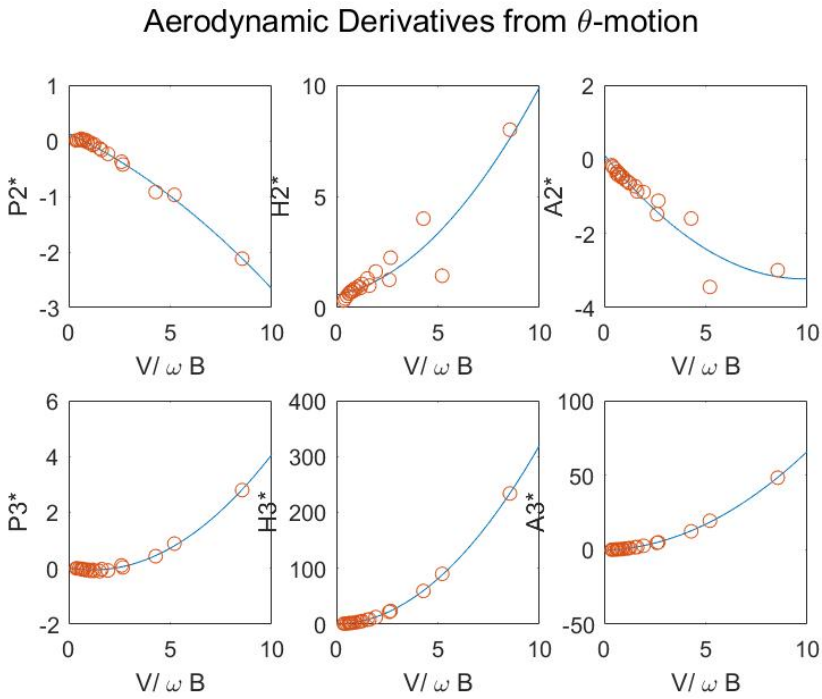

Figure C.3: Aerodynamic derivatives from angular motion.